



City Research Online

City, University of London Institutional Repository

Citation: Abdi, M. (2015). Multi-electrode stimulation and measurement patterns versus prior information of fast 3D EIT. (Unpublished Masters thesis, City, University of London)

This is the accepted version of the paper.

This version of the publication may differ from the final published version.

Permanent repository link: <https://openaccess.city.ac.uk/id/eprint/16089/>

Link to published version:

Copyright: City Research Online aims to make research outputs of City, University of London available to a wider audience. Copyright and Moral Rights remain with the author(s) and/or copyright holders. URLs from City Research Online may be freely distributed and linked to.

Reuse: Copies of full items can be used for personal research or study, educational, or not-for-profit purposes without prior permission or charge. Provided that the authors, title and full bibliographic details are credited, a hyperlink and/or URL is given for the original metadata page and the content is not changed in any way.



CITY UNIVERSITY
LONDON

Multi–Electrode stimulation and measurement patterns versus prior information for fast 3D EIT

A Thesis Presented to

The School of Engineering and Mathematical Sciences

City University London

In fulfilment

of the requirements for the Degree

Masters of Philosophy

by

Montaserbellah H. M. Abdi

December 2015

Declaration

No portion of the work referred to in this thesis has been submitted in support of an application for another degree or qualification of this or any other university or other institute of learning.

Abstract

Electrical Impedance Tomography or as referred to as EIT, is a typical inverse problem of estimating the unknown interior material impedance properties inside a conductive medium through measurements performed at the periphery of the containing medium. Due to its inverse nature, EIT's poor spatial resolution is still one of its biggest downfalls since meaningful images are hard to obtain without incorporating some sort of prior information about the material distribution characteristics.

Given the ill-posedness of the EIT problem coupled with the limited number of collectable boundary voltage measurements, the resulted discrete system is heavily underdetermined and ill-conditioned. Therefore, a sensible step to overcome this problem is to collect as many measurements as the number of the finite elements composing the medium. From one hand, this is not practically possible, on the other, an increased number of measurements will contribute towards unrealistically high computational overheads both for the assembly and the inversion of the resulted dense system matrix.

For any given EIT configuration, the discrete Picard's stability criterion can be deployed as a practical measure of the system performance against noise contaminated measurements. Herein, this study includes extensive use of this measure to quantify the performance of impedance imaging systems for various injection patterns. In effect, it is numerically demonstrated that by varying electrode distributions and numbers, little improvement, if any, in the performance of the impedance imaging system is recorded. In contrast, by using groups of electrodes in the 3D current injection process, a step increase in performance is obtained. Numerical results reveal that the performance measure of the imaging system is 29% for a conventional combination of stimulation and prior information, 97% for groups of electrodes and the same prior and 98% for groups of electrodes and a more accurate prior. Finally, since a smaller number of electrodes are involved in the measurement process, a smaller number of measurements are acquired. However, no compromise in the quality of the reconstructed images is observed.

List of Publications

- Abdi, M. and P. Liatsis. *EIT in Breast Cancer Imaging: Application to Patient-Specific Forward Model*. in *Developments in E-systems Engineering (DeSE)*. 2011.
- Kantartzis, P., M. Abdi, and P. Liatsis, *Stimulation and measurement patterns versus prior information for fast 3D EIT: A breast screening case study*. *Signal Processing*, 2012. **1**(1).

Acknowledgements

I take this opportunity to show gratitude to the almighty God for making the completion of this thesis possible despite the hurdles that I came across throughout my studies. At the same time, this research would not have been possible without the support of many people. I wish to express my gratitude to my dear supervisor, Professor Panos Liatsis who was abundantly helpful and offered invaluable assistance, tolerance, support and guidance. Deepest gratitude is also offered to Dr. Panagiotis Kantartzis without whose knowledge and assistance this study would not have been successful. I would also like to thank my beloved parents, for their unconditional love, support and patience throughout my life. Last but not least, I would like to thank the school of Engineering and Mathematical Sciences at City University London for their financial support throughout the tenure of my degree.

Contents

Abstract	iii
List of Symbols	xi
List of abbreviations	xiii
Chapter 1: Introduction	1
1.1 Electrical Impedance Tomography (EIT)	1
1.2 Inverse problems	3
1.3 The toilsome EIT	5
1.4 EIT hardware.....	6
1.5 EIT as an imaging modality	7
1.6 Thesis aim and objectives	7
1.7 Thesis contribution	9
1.8 Thesis organisation.....	9
Chapter 2: The EIT forward problem	11
2.1 Overview of the forward problem	11
2.2 EIT problem formulation	13
2.3 Electrode models	15
2.3.1 Continuum Electrode Model	16
2.3.2 Gap Electrode Model.....	17
2.3.3 Shunt Electrode Model	17
2.3.4 Complete electrode model	18
2.4 Finite Element Methods in the solution of solving the EIT forward problem	19
2.4.1 Continuous domain setting.....	20
2.4.2 Discrete domain setting	23
2.5 Current injection and data collection strategies in EIT	25
2.5.1 Adjacent method.....	27
2.5.2 Opposite method.....	28
2.5.3 Adaptive method	28
2.6 Solving the linear system of the forward problem	30
2.6.1 Direct methods	31
2.6.2 Iterative methods	32
2.7 The EIT inverse problem	33
2.7.1 Calculating the Jacobian matrix	36
2.8 Summary	37
Chapter 3: The EIT image reconstruction problem	38
3.1 Introduction.....	39
3.2 The linearised inverse problem	41

3.3 Singular Value Decomposition	42
3.4 Regularisation	44
3.4.1 Standard Regularisation.....	46
3.4.2 Truncated Singular Value Decompositions (TSVD).....	46
3.4.3 Direct algorithms: Standard Tikhonov Regularisation	47
3.4.4 Iterative regularisation techniques.....	50
3.5 The discrete Picard criterion	53
3.6 Summary	54
Chapter 4: Multi stimulation and measurement patterns for fast EIT	55
4.1 Introduction.....	55
4.2 Numerical stability of simulation studies	57
4.2.1 Conservation of Energy	58
4.2.2 Boundary conformity.....	59
4.3 Overview of simulations studies	59
4.4 Computational efficiency.....	60
4.5 A comparison between the conventional opposite 2–electrode pair stimulation and multi– injection protocols based on Picard’s stability and GSVD techniques.....	63
4.5.1 Conventional opposite 2–electrode pair stimulation protocol – 2D and 3D scenarios	64
4.5.2 Proposed Multi–injection stimulation protocol – 2D and 3D scenarios	65
4.6 Multi–injection versus prior information.....	74
4.7 Image reconstruction	77
4.8 Summary.....	83
Chapter 5: Conclusions and future work	84
5.1 The problem and the solution.....	84
5.2 Thesis deliverables	86
5.3 Further Work.....	86
References	89
Appendix A.....	97
Appendix B.....	107
Appendix C.....	110

List of Figures

Figure 1.1 A simple 16–electrodes 2D configuration containing a perturbation. The left–hand side picture shows the single adjacent current injection protocol while on the right–hand side shows opposite multi–injection one. The data collection strategy as shown in the figure is of adjacent nature. That is due to measurements collected from adjacent electrode pairs.....	2
Figure 1.2 ITS, P2000 Electrical Resistance Tomography System at City University London.	3
Figure 2.1 2D domain, marking clearly the domain Ω , boundary $\partial\Omega$, electrodes Γ_i , and inter–electrodes gaps Υ_j	13
Figure 2.2 Adjacent method of data collection for a 16–electrode configuration system. For each stimulation pattern, 13 voltage measurements are collected from non–injecting electrodes (a) First set of injected current $I^{(1)}$. (b) Second set of injected current $I^{(2)}$	27
Figure 2.3 Opposite method of data collection for a 16–electrode configuration system. For each stimulation pattern, 12 voltage measurements are collected from non–injecting electrodes. (a): First stimulation pattern $I^{(1)}$, (b): Second stimulation pattern $I^{(2)}$	28
Figure 2.4 Adaptive method of data collection for a 16–electrode configuration system. For each stimulation pattern, 15 voltage measurements are collected from non–injecting electrodes. (a): First stimulation pattern $I^{(1)}$, (b): Second stimulation pattern $I^{(2)}$	29
Figure 3.1 Groups of Reconstruction algorithms [47].....	39
Figure 3.2 The L–curve of a specific problem, the L–curve is a log–log plot of the solution norm $\ \mathbf{R}\mathbf{x}\ _2^2$ versus the residual norm $\ \mathbf{A}\mathbf{x} - \mathbf{b}\ _2^2$	49
Figure 4.1 Principle of energy conservation. The two top images show the conventional opposite 2–electrode pair injection mechanism, whilst two bottom images show the multi–injection protocol with 4–electrodes per group.....	58
Figure 4.2 The potential distribution and calculated boundary voltages. (a) The field from the first current pattern for the conventional opposite 2–electrode pair stimulation protocol, (b) the field from the first current patter for the multi–injection protocol with 4 electrodes/group, (c) the measured boundary voltages for the conventional opposite 2–electrode pair stimulation protocol, and (d) the measured boundary voltages for the multi–injection protocol.	62
Figure 4.3 The current streamlines for (a) the conventional opposite 2–electrode pair and (b) multi–injection stimulation protocols.	63
Figure 4.4 Conventional opposite 2–electrode pair stimulation protocol gains for a 2D circular medium with a single inhomogeneity located at $(x - 0.45)^2 + (y - 0.4)^2 - 0.2^2 < 0$ and $\delta\sigma = +20\%$ of the background value.	67
Figure 4.5 Proposed multi–injection stimulation protocol gains, for a 2D circular test phantom where a single inhomogeneity is located at $(x - 0.45)^2 + (y - 0.4)^2 - 0.2^2 < 0$ of $\delta\sigma = +20\%$ of the background value.	68
Figure 4.6 Conventional opposite 2–electrode pair stimulation protocol gains for a 3D cylindrical medium, where a single inhomogeneity is located at $(x + 0.5)^2 + (y - 0.3)^2 + (z - 0.4)^2 - 0.1^2 < 0$ of $\delta\sigma = +20\%$ of the background value. A maximum of 3 rings of electrodes are allowed.	69
Figure 4.7 Multi–Injection stimulation protocol gains for a 3D cylindrical medium, where a single inhomogeneity is located at $(x + 0.5)^2 + (y - 0.3)^2 + (z - 0.4)^2 - 0.1^2 < 0$ of $\delta\sigma = +20\%$ of the background value. A maximum of 3 rings of electrodes are allowed.	70
Figure 4.8 Conventional opposite 2–electrode pair stimulation protocol gains for a 3D cylindrical medium, where a single inhomogeneity is located at	

$(x+0.5)^2+(y-0.3)^2+(z-0.4)^2-0.1^2 < 0$ of $\delta\sigma = +20\%$ of the background value. A maximum of 4 rings of electrodes are allowed.	71
Figure 4.9 Proposed multi-injection stimulation protocol gains, for a 3D cylindrical medium, where a single inhomogeneity is located at $(x+0.5)^2+(y-0.3)^2+(z-0.4)^2-0.1^2 < 0$ of $\delta\sigma = +20\%$ of the background value. A maximum of 4 rings of electrodes are allowed.	72
Figure 4.10 Conventional versus proposed opposite protocol for various numbers n_elec of electrodes per group per stimulation group. (a) $n_elec = 1$ (Conventional), (b) $n_elec = 2$, (c) $n_elec = 6$, (d) $n_elec = 8$ electrodes per group. The results shown in the left column assume a simple identity prior whilst in the right column, the NOSER prior is used.	76
Figure 4.11 Conventional opposite protocol. The first column is the original 3D perturbation presented as 2D coronal slices of the cylindrical phantom at levels h . The columns (2–10) are the reconstructions for various values of the regularisation parameter $\lambda = \{1.00000e-001, 1.33352e-002, 1.77828e-003, 2.37137e-004, 3.16228e-005, 4.21697e-006, 4.62341e-007, 7.49894e-008, 1.00000e-008\}$, and the last column represents the reconstructed image resulted from the regularisation parameter produced though the L-curve criterion.	79
Figure 4.12 Proposed opposite protocol (2-electrodes per group). The first column is the original 3D perturbation presented as 2D coronal slices of the cylindrical phantom at levels h . The columns (2–10) are the reconstructions for various values of the regularisation parameter $\lambda = \{1.00000e-001, 1.33352e-002, 1.77828e-003, 2.37137e-004, 3.16228e-005, 4.21697e-006, 4.62341e-007, 7.49894e-008, 1.00000e-008\}$, and the last column represents the reconstructed image resulted from the regularisation parameter produced though the L-curve criterion.	80
Figure 4.13 Proposed opposite protocol (6 electrodes per group). The first column is the original 3D perturbation presented as 2D coronal slices of the cylindrical phantom at levels h . The columns (2–10) are the reconstructions for various values of the regularisation parameter $\lambda = \{1.00000e-001, 1.33352e-002, 1.77828e-003, 2.37137e-004, 3.16228e-005, 4.21697e-006, 4.62341e-007, 7.49894e-008, 1.00000e-008\}$, and the last column represents the reconstructed image resulted from the regularisation parameter produced though the L-curve criterion.	81
Figure 4.14 Proposed opposite protocol (8 electrodes per group). The first column is the original 3D perturbation presented as 2D coronal slices of the cylindrical phantom at levels h . The columns (2–10) are the reconstructions for various values of the regularisation parameter $\lambda = \{1.00000e-001, 1.33352e-002, 1.77828e-003, 2.37137e-004, 3.16228e-005, 4.21697e-006, 4.62341e-007, 7.49894e-008, 1.00000e-008\}$, and the last column represents the reconstructed image resulted from the regularisation parameter produced though the L-curve criterion.	82
Figure A-1 A rough illustration of a 2D with L electrodes attached at its boundary. Right: Continuous domain, and left is the discretised one.	97
Figure A-2 (a) Linear triangular element in the xy-plane. (b) Linear triangular element in the $\xi\eta$ -plane.	98
Figure C-1 2D reconstructions when using conventional opposite 2-electrode pair protocol	111
Figure C-2 2D reconstructions when deploying the proposed multi-injection protocol	112
Figure C-3 3D reconstructions at different heights when using the conventional 2-electrode pair protocol, a maximum of 3 electrode rings is allowed.....	113
Figure C-4 3D reconstruction at different heights when deploying the proposed multi-injection protocol, a maximum of 3 electrode rings is allowed.	114
Figure C-5 3D construction at different heights when using conventional 2-electrode pair protocol, a maximum of 4 electrode rings is allowed.	115
Figure C-6 3D reconstructions at different heights when deploying multi-injection protocol, a maximum of 4 electrode rings is allowed.	116

List of Tables

Table 4.1 Percentage reduction time when using the multi-injection protocol	62
Table 4.2 Conventional opposite 2-electrode pair stimulation protocol gains for a 2D circular test phantom.	73
Table 4.3 Conventional opposite 2-electrode pair stimulation protocol gains, when a maximum of 3-rings of electrodes is allowed.	73
Table 4.4 Conventional opposite 2-electrode pair stimulation protocol gains, when a maximum of 4 rings of electrodes is allowed.	73
Table 4.5 Multi-injection stimulation protocol gains for a 2D circular test phantom.	73
Table 4.6 Multi-injection stimulation protocol gains, when a maximum of 3 rings of electrodes is allowed.	73
Table 4.7 Multi-injection stimulation protocol gains, when a maximum of 4 rings of electrodes is allowed.	73
Table 4.8 Comparison between conventional and proposed (2, 6, and 8 electrodes per group) opposite protocol gains for the 3D phantom with 3 rings of 12 electrodes. Priors considered herein are the Identity (Gain 7) and the NOSER (Gain 8) one.	77

List of Symbols

Throughout the thesis, column vectors and matrices are identified in bold upper-case letter, whereas continuous functions are identified in italic letters. The $(i, j)^{th}$ entry of matrix \mathbf{A} is \mathbf{A}_{ij} , similarly the i th entry of a vector \mathbf{x} is \mathbf{x}_i .

Ω	modelled body
$\partial\Omega$	medium boundary
∇	del operator
\mathbf{B}	magnetic flux density
\mathbf{H}	magnetic field intensity
ρ	charge density
μ	magnetic permeability
\mathbf{D}	electric flux density
\mathbf{E}	electrical field intensity
j	current density inside a medium (continuous function)
\mathbf{j}	total current density inside the medium, it is the summation of the conduction and source current densities i.e., $\mathbf{j} = \mathbf{j}_c + \mathbf{j}_s$
\mathbf{J}	the Jacobian or sensitivity matrix
Λ	nonlinear forward operator that maps the change in the interior conductivities onto the change in the collected boundary voltage measurements
σ	conductivity distribution (continuous function)
$\boldsymbol{\sigma}$	vector containing discrete conductivity values (the entries $\sigma_k _{k=1,\dots,K}$ represents conductivity values at the faces of simplices composing the discretised medium)
$\delta\boldsymbol{\sigma}$	vector containing the change in conductivity values with respect to a reference conductivity $\boldsymbol{\sigma}_0$
$\hat{\mathbf{n}}$	outward unit normal
$N_i(\mathbf{x})$	linear interpolation (basis) functions

$\varphi(\mathbf{x})$	electrical potential function on the interior of the medium (continuous function)
ϕ	discrete values of electrical potential at the nodes of the simplices
ε	electrical permittivity or at some locations is additive noise
ω	relaxation parameter in Landweber iteration
Γ	union of electrodes Γ_l
$ \Gamma_l $	area (in 3D) or length (in 2D) of the l th electrode
z_l	contact impedance of the l th electrode
V_l	electric potential at the l th electrode
y	boundary measured voltages as a function of conductivity change
\mathbf{y}	vector containing the finite boundary measured voltages
\mathbf{y}_{fwd}	vector containing the finite boundary voltages calculated via FEM
$\delta\mathbf{y}$	vector containing the change between the measured and calculated boundary voltages
n	number of nodes in the mesh
\mathbf{I}	current pattern
K	number of elements in the mesh
α	regularisation parameter
δ	change in a given quantity
Δ	an update in a given quantity mainly used in iterative formulae
$\frac{\partial^{(n)}}{\partial t^{(n)}}$	n th partial derivative with respect to time
L	total number of electrodes
m	number of voltage measurements collected at the medium's boundary
γ	generalised singular values
\mathbf{h}	levels at which the 3D model is sliced (for visualisation purposes)
$\mathbf{D}[\cdot]$	a given operator applied to a function
$R(\mathbf{x})$	residual function
κ	condition number of a matrix

List of abbreviations

Abbreviation	Meaning
CEM	Complete Electrode Method
CG	Conjugate Gradients
CG	Conjugate Gradient
CT	Computer Tomography
EIT	Electrical Impedance Tomography
FEM	Finite Element Method
GSVD	Generalised Single Value Decomposition
MRI	Magnetic Resonance Imaging
PCG	Preconditioned Conjugate Gradient
PDE	Partial Differential Equation
PET	Positron Emission Tomography
SPECT	Single Photon Emission Computerised Tomography
STR	Standard Tikhonov Regularisation
SVD	Singular Value Decomposition
TGSVD	Truncated Generalised Singular Value Decomposition
TSVD	Truncated Singular Value Decomposition

Chapter 1

Introduction

Research is to see what everybody else has seen, and to think what nobody else has thought

Albert Szent–Gyorgyi

1.1 Electrical Impedance Tomography (EIT)

Electrical Impedance Tomography (EIT) has been a topic of increasing interest to the Medical Imaging community in the last few decades. Since 1970s, EIT has been actively researched where the number of published papers and journals has been notably growing. As the name suggests, EIT is the process of producing 2D and 3D images of the inside of a medium. This process takes place through injecting a given medium with a sequence of electrical currents via an array of electrodes attached to its periphery, and measuring the resulted voltages. These measurements are then used to reconstruct visual images of the inside of that medium.

The non–invasive nature of the EIT technology, its practicality and portability in producing images have shown promising results which may lead to adopting this technology in medical or industrial applications.

One advantage that distinguishes EIT from other imaging modalities is the use of *low*–amplitude AC currents in the injection process. Although for some, this is considered a disadvantage during to the scattering effect [1], but for others, it is an advantage due to low power (heat) injected into the medium especially when used for medical purposes and the medium is the human body.

The set of electrodes, either current–injecting or voltage–measuring, can be arranged in different ways to achieve the best rate of object detection or distinguishability. Figure 1.1 shows a simple 2D 16–electrode EIT configuration illustrating how

CHAPTER 1. INTRODUCTION

electrical currents are fired into the medium and voltages are measured across various electrodes at the boundary. Figure 1.2 shows the ERT (Electrical Resistance Tomography) system used in the Information Engineering and Medical Imaging Centre at City University London.

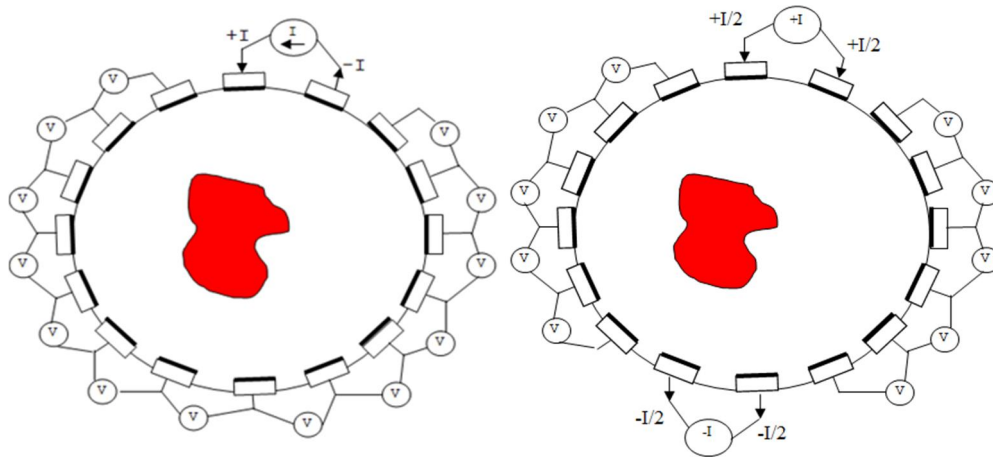


Figure 1.1 A simple 16-electrodes 2D configuration containing a perturbation. The left-hand side picture shows the single adjacent current injection protocol while on the right-hand side shows opposite multi-injection one. The data collection strategy as shown in the figure is of adjacent nature. That is due to measurements collected from adjacent electrode pairs.

Historically, the 2D EIT has suffered from producing limited spatial resolution due to its ability to only produce a cross sectional image of a 3D medium let alone the limitation in the electrodes configuration. Both make the 2D EIT modality less resembling to real life problems. However, the application of 3D EIT through employing two or more equally spaced electrodes sequence around a body in specific planes has introduced enhancements in the reconstructed images as reported in [2] and [3]. The use of EIT imaging modality in many applications such as biomedical, industrial, geophysical, etc., is almost the same; that is due to the image reconstruction process, which differs only in the use of the prior information and the configuration of the electrodes.

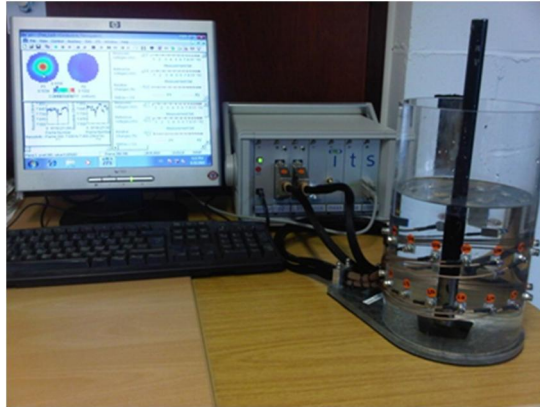


Figure 1.2 ITS, P2000 Electrical Resistance Tomography System at City University London.

It is important to note at this stage that images produced from deploying the EIT modality are of a differential nature i.e., imaging the impedance difference between two states; the reference state which depicts our prior knowledge of the medium, and object/phantom which lies/occurs within that medium. This narrows down the EIT applications to moving objects or 2–state phantoms only, e.g., moving objects in a medium or the inhale and exhale process of the lungs. Other EIT modalities have been developed such as the Multi–frequency EIT which entails injecting the medium with electrical currents of various frequencies, this is outside the scope of this thesis.

To achieve this, the medium is first injected with reference electrical currents and voltage measurements are then taken from the boundary. Another set of measurements are collected at a different state of medium (when the resistive change takes place). Using the difference in voltages and currents, an image is then reconstructed to represent the change in medium’s resistivity. Therefore, EIT can be widely used in many medical applications based on difference imaging such as, the gastric imaging, detection of intrathoracic fluid volumes, detection of haemorrhage, and monitoring of hyperthermia.

1.2 Inverse problems

CHAPTER 1. INTRODUCTION

The EIT modality along with many imaging applications are a part of class of problems referred to as inverse problems. These problems generally arise when one wishes to compute information about internal or otherwise hidden data from the external (or otherwise accessible) measurements. Inverse problems, in turn, belong to the class of ill-posed problems. The term was coined in the early 20th century by Hadamard who worked on problems in mathematical physics, and believed that ill-posed problems did not model the real world, however, he proved to be wrong. Hadamard defined a linear problem to be well-posed if it satisfied the following three requirements [5]:

- Existence: the problem must have a solution
- Uniqueness: there must be only one solution to the problem
- Stability: the solution must depend continuously on the data

If a problem violates one or more of these requirements, it is said to be ill-posed. The EIT problem involves estimating the unknown material conductivity distribution σ from the collected boundary measurements y . Clearly, this problem is nonlinear; therefore, one can introduce a forward operator Λ as

$$\Lambda(\sigma) = y \quad \text{Eq.(1.1)}$$

where σ is the medium's conductivity distribution and y is the observable boundary measurements vector. However, in order to solve this system, one opts to discretise Eq.(1.1), using Taylor's expansion for example, and yields the following discrete linearised system

$$\mathbf{J}\partial\sigma = \partial y \quad \text{Eq.(1.2)}$$

where \mathbf{J} is the discrete form of the operator Λ (Jacobian or sensitivity matrix), $\partial\sigma$ is the finite number of conductivities across the faces of the simplices comprising the model, and ∂y is the finite number of collected boundary voltage measurements. (A thorough discussion of the linearised EIT inverse problem is discussed in the following chapters).

Generally speaking, the relatively poor spatial resolution of the reconstructed images in EIT is often quoted as its major disadvantage, compared with already existing

imaging techniques with good resolution. In this respect, it must be clarified that the motivation of EIT is somewhat different from that of conventional imaging techniques. Despite its limited resolution, the main ask is to provide a reliable, real-time, portable and cost efficient imaging tool. However, the process of conductivity estimation in EIT is a highly nonlinear, ill-conditioned¹ and ill-posed problem. The sensitivity matrix \mathbf{J} , which relates interior conductivity difference to perturbations in the boundary voltage data is heavily ill-conditioned with respect to inversion. So, it requires special treatment in the form of regularisation or a truncation of a singular value expansion [5]. When approaching an ill-posed problem, instead of attempting to solve the original problem one often opts to solve a similar one which is less computational exhaustive. Therefore, effective EIT image reconstruction algorithms are required.

1.3 The toilsome EIT

As mentioned earlier, the problem of recovering an unknown conductivity (reciprocal of resistivity) from boundary data is severely ill-posed, and it is Hadamard's third criterion which is violated. In practice, for any given measurement precision, there are randomly large changes in the conductivity distribution which are untraceable by boundary voltage measurements at that precision. This is a direct indication that low frequency electrical imaging does not provide an accurate conductivity change and boundary voltage correlation. However, the 'partial' solution of this problem is to incorporate additional information about the conductivity distribution. When sufficient prior information is known, it limits the solution so that the huge variations causing the instability are eliminated.

Further, the first two Hadamard's requirements can be overcome more easily than the third; as the existence of a solution is not an arguable issue. That is due to the fact that the body naturally does have conductivity on the inside. The catch here is that, the data should be sufficiently accurate to be consistent with the conductivity

¹ The condition number \mathcal{K} is defined as the ratio between the highest and lowest singular values, and it gives an indication of how numerically stable the system matrix \mathbf{A} is, in the linearised system $\mathbf{Ax}=\mathbf{b}$.

CHAPTER 1. INTRODUCTION

distribution. Minute errors in measurement can violate consistency conditions, such as reciprocity. One of the ways to overcome this problem is to project this unviable data onto the closest viable set. Finally, the problem of solution uniqueness is often referred to by mathematicians as sufficiency of data [5].

Generally speaking, the conductivity inverse boundary value problem (or *Calderón* problem) is to establish a complete knowledge of the relationship between voltage and current at the boundary and to determine the conductivity in a unique manner. This has been demonstrated under a variety of assumptions about the smoothness of the conductivity [6]. However, since only a finite number of measurements from the electrodes can be collected, and since the electrodes cover only a portion of the surface of the body, and not all of them are involved in the measurement process, the number of independent measurements made and the accuracy of the measurements limit the number of degrees of freedom of a parameterised conductivity that one can recover.

1.4 EIT hardware

Most of the factors limiting measurement accuracy in EIT systems lie with the data acquisition system. In most practical systems, the measuring device applies a known, current pattern on two or more electrodes, and measures the developed voltages across the others. As reported in [7], a practical EIT system will normally have the following components: waveform synthesiser, current source, differential amplifier, and a demodulator or some combination of their components. A comprehensive discussion on EIT hardware components can be found in [7] and [8]. Rigaud and Morucci [8], [9] published a review on the hardware solutions developed for EIT and outlined the progress which has taken place in recent years, in terms of measurement strategy and development to overcome hardware error sources that have undesired effects on image recovery [8]. In effect, it appears that there are significant instrumentation problems, due to the interaction of finite current drive output impedance, recording amplifier common mode rejection, and unequal skin–electrode impedances. A number of different EIT systems were successfully constructed or are presently under development to address these limitations ([10]–[12]). These systems

employ varying strategies, such as additional electrodes, multiple electrode current injection, or recording at multiple frequencies, to improve image accuracy with great success.

1.5 EIT as an imaging modality

There are currently three ways to image the distribution of impedance within the body [7], according to the nature of the application: static, multi-frequency or dynamic corresponding to single frequency, multi-frequency and “real-time” imaging types. The first two ways are normally concerned with producing images that show how the different types of tissue are distributed in the body, known as tissue characterisation or anatomical imaging. In such applications, EIT is used as an alternative to X-rays, CT and MRI, with certain practical advantages. The third technique produces images of physiological function, such as imaging short (e.g., millisecond) changes in the physiological state of the body.

In electrical impedance tomography, images are reconstructed from sets of electrical measurements made on the surface of the body. To obtain high-quality images, independent measurements with good accuracy, precision and repeatability are needed from the data acquisition system. Noise, optimal current patterns, and electrode-electrolyte impedance are among other factors that impose stringent requirements on the accuracy of an EIT data acquisition system. Despite these hurdles, useful images at relatively low resolution have been obtained. In [3], a spatial resolution of about 10% of image background for a centrally located object in the cross-sectional plane, using a 64-electrode data acquisition system is reported. Using a 32-electrode system, Casas *et al* [12] obtained a spatial resolution of 14% for a similar scenario. Although, the spatial resolution of EIT is limited, its temporal resolution and sensitivity in dynamic imaging is rather good [13]. It appears that better spatial resolution ought to be achievable by improving either the data acquisition system and/or the performance of the reconstruction algorithm [14].

1.6 Thesis aim and objectives

CHAPTER 1. INTRODUCTION

One of the downfalls of EIT is its limited spatial resolution of the conductivity distribution on the inside of a conductive continuum. However, the addition of a third dimension, has added the flexibility needed to add more electrodes, and therefore, more measurements to be incorporated in the reconstruction process. Indeed, that helped to capture the conductivity distribution from different axes and angles, but added an exhaustive process in acquiring the measurements resulted from increasing the number of injecting electrodes.

Therefore, the aim of this thesis is to develop enhancements in EIT current injection protocols, reducing the acquisition time, whilst maintaining the quality of the produced EIT images. The aim of this thesis will be addressed in terms of the following objectives:

1. Utilising the concept of multi-injection protocol over 2D shapes, and comparing it against the existing opposite 2-electrode pair stimulation protocol in terms of quality and acquisition time.
2. Extending the concept to cover 3D shapes, with different levels of electrode-rings, and comparing the quality based on the *gain* of the selected stimulation pattern quantifier, that is, the ratio of the generalised singular values that meet Picard's criterion [15] over the total number of available generalised singular values.
3. Assessing the effect of deploying the multi-injection protocol on the quality of the resulting reconstructed images.

In the EIT forward model simulations, high-resolution fine meshes generated by the Netgen mesh generator [16] are developed. The numerical costs associated with this can be dealt with quite easily due to the use of Finite Element Analysis (FEA) to solve the forward problem. On the other side, for the inverse problem, coarser meshes are generated using the same platform, and that is for two reasons, the first is to avoid the so-called inverse crime resulting from employing the same model to generate, as well as invert, the given data [17], while the other reason is to ease off the inverse calculations due to calculating the inverse of the Jacobian matrix whose number of columns is proportional to the number of finite elements constituting the

model. Finally, throughout the simulations carried out in this thesis, it is assumed that the voltages are not measured on the current carrying electrodes, e.g., [18]–[19].

1.7 Thesis contribution

This work done has contributed to the Electrical Impedance Tomography imaging technology by adding an adjustment to the current injection and voltage measurement processes. The thesis scope is a follow up to the guidelines of the work done in [20], in which the authors have made use of deploying multi-current injection patterns over 2D mediums. This has produced a lesser number of collected measurements and therefore reduced computational overheads when solving the forward problem.

In addition, the thesis extends the scope to include 3D models, where a greater number of electrodes and patterns is often available. The work develops the 3D multi-current injection stimulation pattern; that is, injecting alternating electrical currents through selected opposite groups of electrodes instead of injecting through only a pair.

On the other hand, the contribution of this work differs from the one in [20]; in this work, the groups of variable electrode numbers to apply the desired stimulation protocol are accounted for. This implies a variable reduction in the number of collected measurements (and thus data acquisition times) without compromising the quality of the reconstructed images.

1.8 Thesis organisation

CHAPTER 1. INTRODUCTION

A detailed overview of the EIT forward model including the various interpretations of electrode–boundary interactions, the solution of the governing Laplacian equation, and the formulation of the EIT forward and inverse problems and the derivation of the Jacobian matrix are encapsulated in Chapter 2.

Afterwards, Chapter 3 proceeds with illustrating the inverse nature of the EIT problem, and the various techniques and methods used to solve the linearised EIT inverse problem. It also discusses the concept of regularisation, and different methods, direct or iterative, to perform the regularisation process over the EIT problem. A quantifier referred to as the Discrete Picard condition, to assess the performance and robustness of an EIT system under the existence of noise is discussed.

Chapter 4 sets out the simulation framework as it starts off with a demonstration of the multi–injection protocol in 2D models, which is expanded to cover 3D ones. Picard graphs and image reconstructions quantifying the performance of each stimulation protocol including the gain calculations are also presented within. The thesis finally concludes with Chapter 5 which contains the conclusions and any potential future work.

Chapter 2

The EIT forward problem

Research is what I'm doing when I don't know what I'm doing.

Wernher Von Braun

In this chapter, the formulation of the EIT forward problem is derived from the basic principles of Maxwell's equations. This is followed by a discussion of various electrode configurations and current injection/voltage acquisition protocols used throughout the history of EIT. Afterwards, the study expands to cover the use of some of the common analytical and numerical methods to solve such equations. The emphasis will be applied on the use of the Finite Element Method (FEM) which benefits and downfalls will be highlighted. Finally the chapter concludes with the derivation of the EIT inverse problem and the associated system which, along with other factors, accounts for the image reconstruction problem discussed in the following chapter.

2.1 Overview of the forward problem

In order to produce meaningful images of the interior of a given conductive medium with an object/phantom lying/occurring within, two interconnected and subsequent processes are considered; The forward problem; where one opts to estimate the boundary voltages excited across the boundary electrodes as a result of injecting the medium with a specific electrical current pattern. The second process, which is referred to as the Inverse problem, is the process in which the mathematically calculated voltages along with the experimentally are used to find an estimation of the difference of the medium's inner conductivity in a form of an image.

Mathematically speaking, assuming a uniform medium with homogenous conductivity distribution, continuous boundary and a known current pattern driven at its boundary. The forward problem is to compute the real boundary voltages

$\mathbf{y}_{\text{fwd}} \in \mathbb{R}^m$, where m is the number of voltage measurements across boundary electrode.

This includes solving the governing Laplacian equation,

$$\nabla \cdot (\sigma(\mathbf{x}) \nabla \phi(\mathbf{x})) = 0 \quad \text{Eq.(2.1)}$$

where $\phi(\mathbf{x}) \in H^1(\Omega)$ ² [1] is a scalar function representing the electric potential inside the continuum, $\sigma(\mathbf{x}) \in L^2(\Omega)$ ³ is the material conductivity (real material conductivity is assumed throughout). Both the electric potential and conductivity are functions of the spatial distribution $\mathbf{x} \in \Omega$ and the body $\Omega \subset \mathbb{R}^n$ which is a closed and bounded subset of a 2D (i.e., $n = 2$) or 3D (i.e., $n = 3$) space with a smooth (or sufficiently smooth) boundary $\partial\Omega$. Figure 2.1 illustrates a simple 2D medium configuration.

For Eq.(2.1) to be solved uniquely, one ought to couple it with a set of boundary conditions that represents restrictions imposed on the problem at hand, such as smoothness of the boundary or confinement of energy. This can be achieved by either deploying analytical [21], i.e., calculating the potentials at any points inside a given medium, or numerical solutions [22], i.e., which find estimates of the potentials at the nodes of the finite elements composing the model. Through the course of EIT history, numerical techniques have proved to be superior over the analytical ones, due to their adaptability to complex geometries, which the analytical techniques have shown to be very computationally exhaustive in dealing with.

However, another important factor in solving Eq.(2.1) is the accurate modelling of the phantom under study. This includes the geometry and boundary of the model.

² Having the electrical potential $\phi(\mathbf{x})$ to be in the Sobolev space i.e., $\phi(\mathbf{x}) \in H^k(\Omega)$ for an integer k indicates that the square of the k th derivative has a finite integral over the domain Ω . For non-integer and negative powers, Sobolev spaces are defined by taking the Fourier transform, multiplying by a power of frequency and demanding the result is square integrable i.e., $\int_{\Omega} |\phi^{(k)}(\mathbf{x})|^2 d\Omega < \infty$.

³ Having the conductivity $\sigma(\mathbf{x})$ to be in the $L^2(\Omega)$ indicates that the square of the function has a finite integral over the domain Ω i.e., $\int_{\Omega} |\sigma(\mathbf{x})|^2 d\Omega < \infty$

The locations of the electrodes on the surface are also of prime importance; their characteristics might affect their reliability and applicability in real life applications. In the next section, Maxwell's equations are used as mathematical links which tie the conditions imposed over the medium's boundary with the electrical fields inside the medium.

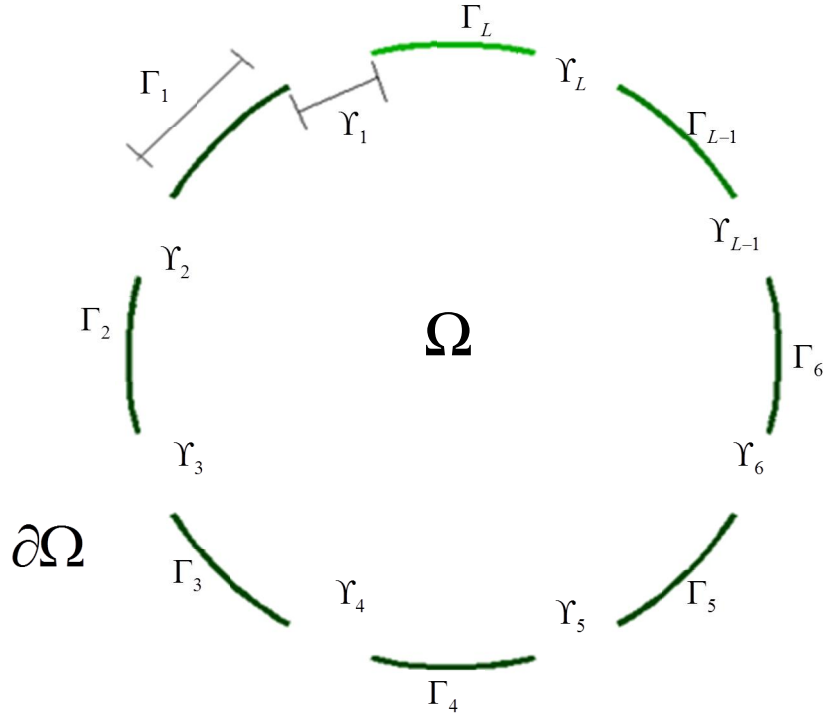


Figure 2.1 2D domain, marking clearly the domain Ω , boundary $\partial\Omega$, electrodes Γ_i , and inter-electrodes gaps Υ_j

2.2 EIT problem formulation

In this section, Maxwell's equations for electro-magnetics [23] are used to derive the generic EIT governing Equation Eq.(2.1). Without loss of generality, the medium is assumed to be uniform, conductive, isotropic, non-dispersive, and linear. The current injection is confined within the electrodes' areas and is normal to the boundary $\partial\Omega$. The electrodes are assumed as disjoint uniform boundary segments (as shown in Figure 2.1). There is no current traffic on the inter-electrode areas (labelled as Υ_j in Figure 2.1). Finally, the eddy (leakage) currents will be assumed zero, i.e., the amount of currents injected into the medium is exactly equal to the amount exiting.

CHAPTER 2. THE EIT FORWARDPROBLEM

Further, Maxwell's equations state that the curl of the electrical field intensity \mathbf{E} is equal to the negative time-derivative of the magnetic flux density \mathbf{B} ,

$$\nabla \times \mathbf{E} = -\frac{\partial \mathbf{B}}{\partial t} \quad \text{Eq.(2.2)}$$

and that the curl of magnetic field intensity \mathbf{H} is essentially the current density flowing inside the medium plus the rate of change of the electric flux density \mathbf{D} , as

$$\nabla \times \mathbf{H} = \frac{\partial \mathbf{D}}{\partial t} + \mathbf{j} \quad \text{Eq.(2.3)}$$

where \mathbf{E} , \mathbf{B} , \mathbf{H} , \mathbf{D} , and \mathbf{j} refer to the electric field intensity, magnetic flux density, magnetic field intensity, electric flux density, and current density, respectively.

From Gauss's law for magnetism, the divergence of \mathbf{B} through a closed surface is equal to zero i.e.,

$$\nabla \cdot \mathbf{B} = 0 \quad \text{Eq.(2.4)}$$

and according to Gauss law, the charge density ρ can be given as the divergence of \mathbf{D} as,

$$\nabla \cdot \mathbf{D} = \rho \quad \text{Eq.(2.5)}$$

The conduction current density can be represented as

$$\mathbf{j}_c = \sigma \mathbf{E} \quad \text{Eq.(2.6)}$$

However, the total current is then $\mathbf{j} = \mathbf{j}_c + \mathbf{j}_s$, the sum of the conduction and source currents. EIT assumes that the source current \mathbf{j}_s is typically zero at frequency ω .

EIT assumes that the injected electrical currents are of a low frequency nature, in which a change in conductivity would have some effect on any measurement of surface voltage [24]. This assumption makes it possible to neglect the magnetic field effects or simply assuming a direct current case.

Hence, taking the divergence of Eq.(2.3) as,

$$\nabla \cdot (\nabla \times \mathbf{H}) = \nabla \cdot \left(\frac{\partial \mathbf{D}}{\partial t} + \mathbf{j} \right) \quad \text{Eq.(2.7)}$$

or simply,

$$\nabla \cdot (\nabla \times \mathbf{H}) = \frac{\partial}{\partial t} \nabla \cdot \mathbf{D} + \nabla \cdot \mathbf{j} = 0 \quad \text{Eq.(2.8)}$$

Substituting Eq.(2.5) into Eq.(2.8) results in,

$$\frac{\partial \rho}{\partial t} + \nabla \cdot \mathbf{j} = 0 \quad \text{Eq.(2.9)}$$

Since the system is assumed to be running under the quasi-static assumption, the term $\frac{\partial \rho}{\partial t}$ therefore plunges to zero, resulting in,

$$\nabla \cdot \mathbf{j} = 0 \quad \text{Eq.(2.10)}$$

Eq.(2.10) is another way of looking at Kirchhoff's current law; the amount of the current going into the medium is the same as the amount of currents going out (conservation of energy). Using relation $\mathbf{j}_c = \sigma \mathbf{E}$, Eq.(2.10) can be rewritten as

$$\nabla \cdot (\sigma \mathbf{E}) = 0 \Rightarrow \nabla \cdot (\sigma (-\nabla \phi)) = 0 \Rightarrow \nabla \cdot (\sigma \nabla \phi) = 0 \quad \text{Eq.(2.11)}$$

2.3 Electrode models

As previously mentioned, in order to solve Eq.(2.1) efficiently, a set of boundary conditions ought to be incorporated. Through the history of EIT, several electrode configurations demonstrating these conditions have been developed in order to interpret the electrode interactions with the medium to which they are attached. A detailed description can be found in [25].

Throughout the thesis, unless otherwise stated, the electrodes are considered as a set of disjoint boundary segments Γ_l where

$$\Gamma = \bigcup_{l=1}^L \Gamma_l ; L \text{ is the total number of electrodes} \quad \text{Eq.(2.12)}$$

represents the total boundary segment occupied by the electrodes with each having a length (2D shapes) or an area (3D shapes) of $|\Gamma_l|$ units. On the other hand, the boundary segments denoted by Υ_l where

$$\Upsilon = \bigcup_{l=1}^L \Upsilon_l = \partial\Omega \setminus \Gamma \quad \text{Eq.(2.13)}$$

characterises the total inter–electrode boundary gaps.

2.3.1 Continuum Electrode Model

The continuum electrode model [26] is the simplest of the models used in electrical impedance tomography. This model does not account for the attached electrodes, and assumes that the injected current is a continuous function, that is,

$$I(t) = \nu \cos(\omega t) \quad \text{Eq.(2.14)}$$

where ν and ω are the constants corresponding to current amplitude and frequency, respectively.

Hence, according to the continuum model, the injected current density can be randomly set on the entire boundary of the medium

$$\mathbf{j}_{int} \cdot \hat{\mathbf{n}} = -\mathbf{j}_{inj} \cdot \hat{\mathbf{n}} \text{ on } \partial\Omega \quad \text{Eq.(2.15)}$$

where $\hat{\mathbf{n}}$ is the outward normal vector to $\partial\Omega$, and \mathbf{j}_{inj} is the injected current density.

This configuration only considers the normal components of the injected current, as electrodes (supposed to be perfect conductors) would shunt the tangential components of the electric field. Using Ohm's law and recalling that \mathbf{E} is conservative, Eq. (2.15) can be expressed as a Neumann boundary condition

$$\sigma \frac{\partial \phi}{\partial \hat{\mathbf{n}}} = -\mathbf{j}_{inj} \cdot \hat{\mathbf{n}} \text{ on } \partial\Omega \quad \text{Eq.(2.16)}$$

Additionally, the conservation of charge must be preserved

$$\int_{\partial\Omega} \mathbf{j}_{inj} \cdot \hat{\mathbf{n}} \cdot d(\partial\Omega) = 0 \quad \text{Eq.(2.17)}$$

and the condition

$$\int_{\partial\Omega} \phi \cdot d(\partial\Omega) = 0 \quad \text{Eq.(2.18)}$$

to make the model complete by assigning a reference voltage. The continuum model is a very rough approximation of the electrode/medium interface and hence, the difference between the voltages resulting from the forward calculations and the actual measurements can be quite high [24].

2.3.2 Gap Electrode Model

The Gap Electrode Model [24] is an enhancement of the previously described continuum model. It is the first model to consider the electrodes as a set of discrete subdomains (as shown in Figure 2.1), and it approximates the current density at each electrode by a constant value

$$j_l = \sigma \frac{\partial \phi}{\partial \hat{\mathbf{n}}} = \begin{cases} \frac{I_l}{|\Gamma_l|} & \text{on } \Gamma_l \text{ for } l=1, \dots, L \\ 0 & \text{on } \Upsilon_l \text{ for } l=1, \dots, L \end{cases} \quad \text{Eq.(2.19)}$$

where I_l is the injected current at l electrode

The conservation of charge is imposed as

$$\sum_l I_l = 0 \quad \text{Eq.(2.20)}$$

Unfortunately, the assumption that the current density is constant on the interface of each electrode is an oversimplification for many practical EIT applications. Moreover, both the continuum and gap models ignore both the shunting effect of the electrodes and their contact impedances.

2.3.3 Shunt Electrode Model

The Shunt Electrode Model [24] modifies the Gap Electrode Model by considering that the current density characteristics underneath the electrodes are assumed to be unknown. The model simply assumes that the total current density injection through the electrodes should be equal to the injected current. This means replacing the condition in Eq.(2.19) by

$$j = \sigma \frac{\partial \phi}{\partial \hat{\mathbf{n}}} \text{ on } \Gamma \quad \text{Eq.(2.21)}$$

The main difference from the gap model is that the shunt model accounts for the shunting effect i.e., considering the potential at each electrode to be constant as

$$\phi(\Gamma_l) = V_l \quad \text{Eq.(2.22)}$$

As mentioned earlier, V_l represents the electric potential value at the l th electrode.

Finally, the unique solution can be obtain by selecting a ground point as,

$$\sum_l V_l = 0 \quad \text{Eq.(2.23)}$$

However, this model underestimates the resistivities, since it ignores the contact impedance of the electrodes.

2.3.4 Complete electrode model

The complete electrode model (CEM) [27], [28] is the most refined description of the interface between the electrodes and the boundary of the medium. The model is an update of the Shunt Electrode Model as it includes the effect of the contact impedance with the boundary.

The alternating currents are fired from a set of electrodes fixed at the periphery in a direction normal to the boundary surface. This gives rise to a current density j of

$$j = \sigma \frac{\partial \phi}{\partial \hat{\mathbf{n}}} \quad \text{on } \Gamma \quad \text{Eq.(2.24)}$$

and since the injection is limited to the electrodes, the inter-electrode gaps exhibit no flow of current through them. Also, the eddy currents escaping these areas are assumed to be negligible,

$$\sigma \frac{\partial \phi}{\partial \hat{\mathbf{n}}} = 0 \quad \text{on } \Upsilon \quad \text{Eq.(2.25)}$$

Finally, what differentiates the complete electrode model from its predecessors is its consideration of the voltage drop across the thin layer (resistance) connecting the electrode to the medium. Mathematically speaking,

$$\phi + z_l \sigma \frac{\partial \phi}{\partial \hat{\mathbf{n}}} = V_l \quad \text{on } \Gamma_l \quad \text{Eq.(2.26)}$$

where $z_l \neq 0$ is the electrode contact impedance which could vary over Γ_l but assumed constant i.e., $z_l \in \mathbb{R}$. Another way of writing the expression in Eq.(2.26) is

$$\phi + z_l \sigma \nabla \phi \cdot \hat{\mathbf{n}} = V_l \quad \text{on } \Gamma_l$$

It has been proven in [27] that this model produces a unique solution when the conservation theorem holds, i.e.,

$$\int_{\partial \Omega} \mathbf{j} = 0 \Leftrightarrow \sum_{l=1}^L I_l = 0 \quad \text{Eq.(2.27)}$$

and a selection for ground is considered,

$$\int_{\partial\Omega} \phi = 0 \Leftrightarrow \sum_{l=1}^L V_l = 0 \quad \text{Eq.(2.28)}$$

The Complete Electrode Mode is a well-posed problem and has a unique solution. It is also the most refined electrode model in EIT so far.

2.4 Finite Element Methods in the solution of solving the EIT forward problem

In order to solve for the electrical potentials and boundary voltages, the governing equation in Eq.(2.1), along with a boundary condition selection (as described in Section 2.3.4) are coupled together to construct an integrated system which, with the aid of discretisation, turns into a linear system of equations that can be solved either via direct or iterative methods.

The basic idea of Finite Element Methods (FEM) [29] is to approximate the domain of interest Ω as a union of a finite number of elements Ω_k , which for simplicity can be assumed to be simplices. In a two dimensional scenario, a simplex is a triangle, and in a three dimensional one, it is a tetrahedron. A collection of such simplices is called a finite element mesh.

Assuming a domain Ω having K simplices with n vertices. The continuous electric potential $\phi(\mathbf{x})$ inside the mesh i.e., $\mathbf{x} \in \Omega$ can be approximated using this mesh by functions, which are linear on each simplex, and continuous across the faces. These functions, also referred to as interpolation or basis functions, have the appealing feature that they are completely determined by their values at the mesh vertices. A natural basis is the set of functions $N_i(\mathbf{x})$ that are one on vertex i and zero at the other vertices, i.e.,

$$N_i(\mathbf{x}) = \begin{cases} 1 & \text{on vertex } i, \\ 0 & \text{otherwise.} \end{cases}$$

Hence, the electrical potential can be approximated as,

$$\begin{aligned}\phi(\mathbf{x}) &\cong \tilde{\phi} = \sum_{i=1}^n \varphi_i N_i(\mathbf{x}) \\ &\cong \varphi_1 N_1(\mathbf{x}) + \varphi_2 N_2(\mathbf{x}) + \cdots + \varphi_n N_n(\mathbf{x})\end{aligned}\tag{Eq.(2.29)}$$

and the vector $[\varphi_1, \dots, \varphi_n]^T \in \mathbb{R}^n$ represents the discrete approximations of the electric potential.

However, it is not difficult to note that these basis functions have to be either quadratic or at least twice differentiable in order to satisfy equation Eq.(2.1) [1] due to the second order derivative nature of the Laplacian operator. However, the resulting complexity resulting from using such basis functions can be avoided by utilising a method referred to as The *Method of Weighted Residuals* (MWR) [30], the latter will be elaborated in more details in the following sections.

2.4.1 Continuous domain setting

The forward problem under consideration, in this context, is the one described by Eq.(2.1), and the set of boundary conditions Eq.(2.24) – Eq.(2.28). As mentioned before, in order to apply the finite element concept and discretise the system, the weak formulation of the problem should be derived first.

2.4.1.1 Weak formulation of the EIT Partial Differential Equation (PDE)

Many authors refer to the PDE described by Eq.(2.1) as the *strong formulation*. This is due to the fact that in order to solve this equation, one must be able to compute the highest order derivative term in the PDE. In other words, the electric potential function $\phi(\mathbf{x})$ must be at least twice differentiable and should not disappear when its second derivatives are taken. Hence, one way to weaken this requirement, integration by parts can be applied to the strong formulation to derive the weak formulation of the problem. The weak formulation, therefore, allows the use of the first-order linear basis functions to solve the problem as they only have to be once differentiable.

CHAPTER 2. THE EIT FORWARD PROBLEM

The Method of Weighted Residuals or MWR [30] is a family of methods mainly used to obtain approximate solutions to differential equations. Mathematically speaking, if one assumes a linear operator D acting on a potential function $\phi(\mathbf{x})$ to produce a function $p(\mathbf{x})$,

$$D[\phi(\mathbf{x})] = p(\mathbf{x})$$

and the function $\phi(\mathbf{x})$ is to be approximated as in Eq.(2.29). Then, by substituting the discretised value of $\phi(\mathbf{x})$, i.e., $\tilde{\phi}$ into the differential operator, D , does not, in general, result in $p(\mathbf{x})$. Hence, an error or residual exists,

$$R(\mathbf{x}) = D[\tilde{\phi}] - p(\mathbf{x}) \neq 0$$

The idea behind the method of weighted residuals is to essentially force the residual function to zero in some average sense over the domain Ω , i.e.,

$$\int_{\Omega} w(\mathbf{x}) R(\mathbf{x}) d\Omega = 0, \quad i = 1, 2, \dots, n \quad \text{Eq.(2.30)}$$

where $w(\mathbf{x})$ is the weight function.

In this context, for the EIT forward problem governing equation, the function $p(\mathbf{x})$ is zero, and denoting the Laplacian in Eq.(2.1) by $D[\tilde{\phi}]$ and residual function $R(\mathbf{x})$ in Eq.(2.30) is essentially

$$\begin{aligned} R(\mathbf{x}) &= D[\tilde{\phi}] - p(\mathbf{x}) \\ &= \nabla \cdot (\sigma \nabla \phi) - 0 \\ &= \nabla \cdot (\sigma \nabla \phi) \end{aligned} \quad \text{Eq.(2.31)}$$

Therefore, inserting this result into Eq. (2.30), results in

$$\int_{\Omega} w(\nabla \cdot (\sigma \nabla \phi)) = 0 \quad \text{on } \Omega \quad \text{Eq.(2.32)}$$

Using Green's second identity and the vector identity

$$\nabla \cdot (w \sigma \nabla \phi) = \sigma \nabla \phi \cdot \nabla w + w \nabla \cdot (\sigma \nabla \phi) \quad \text{Eq.(2.33)}$$

Eq.(2.32) changes to

$$\int_{\Omega} \nabla \cdot (w \sigma \nabla \phi) d\Omega = \int_{\Omega} \sigma \nabla \phi \cdot \nabla w d\Omega + \underbrace{\int_{\Omega} w \nabla \cdot (\sigma \nabla \phi) d\Omega}_{=0 \text{ from equation (2.32)}} \quad \text{Eq.(2.34)}$$

Invoking the divergence theorem

$$\int_{\Omega} \nabla \cdot (w \sigma \nabla \phi) d\Omega = \int_{\partial\Omega} (w \sigma \nabla \phi) \cdot \hat{\mathbf{n}} dS \quad \text{Eq.(2.35)}$$

CHAPTER 2. THE EIT FORWARDPROBLEM

and given that the current density is zero outside the electrodes, as in Eq.(2.25), yields,

$$\begin{aligned} \int_{\Omega} \nabla \cdot (w\sigma\nabla\phi) d\Omega &= \int_{\partial\Omega} w\sigma\nabla\phi \cdot \hat{\mathbf{n}} dS \\ &= \int_{\Gamma} w\sigma\nabla\phi \cdot \hat{\mathbf{n}} dS_{\Gamma} \end{aligned} \quad \text{Eq.(2.36)}$$

Eq.(2.32) can be rewritten using the observation of Eq.(2.36) as,

$$\int_{\Omega} \sigma\nabla\phi \cdot \nabla w d\Omega = \int_{\Gamma} w\sigma\nabla\phi \cdot \hat{\mathbf{n}} dS_{\Gamma} \quad \text{Eq.(2.37)}$$

Rearranging the boundary condition in Eq.(2.26) gives,

$$\sigma\nabla\phi \cdot \hat{\mathbf{n}} = \frac{1}{z_l}(V_l - \phi) \quad \text{on } \Gamma \quad \text{Eq.(2.38)}$$

where $z_l \neq 0$ is the contact impedance between the electrode and medium boundary.

Therefore, incorporating Eq.(2.38) into Eq.(2.37) gives,

$$\int_{\Omega} \sigma\nabla\phi \cdot \nabla w d\Omega = \sum_{l=1}^L \int_{\Gamma_l} \frac{1}{z_l}(V_l - \phi) w dS_{\Gamma_l} \quad \text{Eq.(2.39)}$$

or more conveniently,

$$\int_{\Omega} \sigma\nabla\phi \cdot \nabla w d\Omega - \sum_{l=1}^L \frac{1}{z_l} \int_{\Gamma_l} w V_l dS_{\Gamma_l} + \sum_{l=1}^L \frac{1}{z_l} \int_{\Gamma_l} w \phi dS_{\Gamma_l} = 0 \quad \text{Eq.(2.40)}$$

Finally, the injection current into the medium has the constraint

$$I_l = \int_{\Gamma_l} \sigma \frac{\partial\phi}{\partial\hat{\mathbf{n}}} dS_{\Gamma_l} \quad \text{Eq.(2.41)}$$

which indicates that the amount of current injected into the medium can be kept at certain values through controlling the voltages at the boundaries. This is beneficial when using EIT in medical applications and excessive current values might lead to tissues damage.

Eq.(2.40) is the weak formulation of the governing boundary value problem of Eq.(2.1) with current density applied through the electrodes.

In addition, if the weight functions $w(\mathbf{x})$ are chosen from the same set of functions as the basis functions $N_i(\mathbf{x})$, i.e.,

$$w(\mathbf{x}) = N_i(\mathbf{x}) \quad \text{for } i = 1, 2, \dots, n \quad \text{Eq.(2.42)}$$

the featured weighted residual method is referred to as the *Galerkin method* [30]. The Galerkin method is discussed in the context of this thesis rather than the variational approach due to its simplicity and its intuitive interpretation. The use of variational methods in the solution of boundary value problems is discussed in [31]–[33] and the references therein.

2.4.2 Discrete domain setting

Next, we discuss the process of discretising the weak formulation of Eq.(2.40). That is, computing the solution over a given medium with smooth predefined boundaries. This is done by discretising the domain into a collection of subdomains and calculating the electrical potentials across the nodes (connectors) of these subdomains.

In order to do so, we follow the Galerkin approach by choosing the weight and basis functions to be from the same family. Hence, the weak formulation of Eq.(2.40) turns into,

$$\sum_{i=1}^n \left\{ \int_{\Omega} \sigma \nabla N_i \nabla N_j d\Omega \right\} \varphi_i + \sum_{l=1}^L \left\{ \int_{\Gamma_l} \frac{1}{z_l} N_i N_j dS_{\Gamma_l} \right\} \varphi_i - \sum_{l=1}^L \left\{ \int_{\Gamma_l} \frac{1}{z_l} N_i dS_{\Gamma_l} \right\} V_l = 0 \text{ Eq.(2.43)}$$

and from Eq.(2.41), the current injected from each exciting electrode can be represented as,

$$\begin{aligned} I_l &= \int_{\Gamma_l} \frac{1}{z_l} (V_l - \phi) dS \\ &= \int_{\Gamma_l} \frac{1}{z_l} V_l dS_{\Gamma_l} - \sum_{i=1}^n \left\{ \int_{\Gamma_l} \frac{1}{z_l} N_i dS_{\Gamma_l} \right\} \varphi_i \\ &= \frac{1}{z_l} |\Gamma_l| V_l - \frac{1}{z_l} \sum_{i=1}^n \left\{ \int_{\Gamma_l} N_i dS_{\Gamma_l} \right\} \varphi_i \end{aligned} \quad \text{Eq.(2.44)}$$

where $|\Gamma_l|$ is the area (or in two dimensions, length) of the l^{th} electrode.

If $\mathbf{I} \in \mathbb{R}^L$ is the vector containing a current pattern, then another vector $\mathbf{b} \in \mathbb{R}^{n+L}$ can be set such as $\mathbf{b} = [\mathbf{0}, \mathbf{I}]^T$, where $\mathbf{0} \in \mathbb{R}^n$ is a zero vector. If \mathbf{A} is the global

CHAPTER 2. THE EIT FORWARDPROBLEM

conductance or stiffness matrix with entries indicated below, then using Eq.(2.43) and Eq.(2.44) the EIT forward problem can take the form of a linear set of equations as [1]

$$\mathbf{Ax} = \mathbf{b} \quad \text{Eq.(2.45)}$$

where $\mathbf{A} = \begin{bmatrix} \mathbf{A}_M + \mathbf{A}_Z & \mathbf{A}_W \\ \mathbf{A}_W^T & \mathbf{A}_D \end{bmatrix} \in \mathbb{R}^{n+L \times n+L}$ having the entries:

\mathbf{A}_M is an $n \times n$ symmetric matrix, and has entries $A_{Mi,j}$,

$$\mathbf{A}_{Mi,j} = \int_{\Omega} \sigma \nabla N_i \cdot \nabla N_j d\Omega \quad \text{for } i, j = 1, \dots, n \quad \text{Eq.(2.46)}$$

which represents the solution of Eq.(2.1) discarding all boundary conditions.

However, the conductivity distribution σ is to be approximated over the mesh. An intuitive method is to choose σ to be constant on each simplex (e.g., piecewise constant (PWC) [1]).

Assuming χ_j to be the characteristic function which has the value of one on the j th simplex and zero elsewhere, we have an approximation to σ

$$\sigma \approx \sum_{j=1}^K \sigma_j \chi_j \quad \text{Eq.(2.47)}$$

where K is the total number of subdomains consisting the medium.

The constant σ_j can be taken outside the integral for each simplex. Therefore, Eq.(2.46) can be rewritten as,

$$\mathbf{A}_{Mi,j} = \sum_{k=1}^K \sigma_k \int_{\Omega_k} \nabla N_i \cdot \nabla N_j d\Omega_k \quad \text{Eq.(2.48)}$$

The matrix \mathbf{A}_Z is an $n \times n$ matrix that has entries $\mathbf{A}_{Zi,j}$

$$\mathbf{A}_{Zi,j} = \sum_{l=1}^L \left\{ \int_{\Gamma_l} \frac{1}{z_l} N_i N_j dS_{\Gamma_l} \right\} \quad \text{for } i, j = 1, \dots, n \quad \text{and } l = 1, \dots, L \quad \text{Eq.(2.49)}$$

Furthermore, the matrix \mathbf{A}_W is an $n \times L$ matrix having entries $\mathbf{A}_{Wi,j}$,

$$\mathbf{A}_{Wi} = - \int_{\Gamma_l} \frac{1}{z_l} N_i dS_{\Gamma_l} \quad \text{for } i = 1, \dots, n \quad \text{and } l = 1, \dots, L \quad \text{Eq.(2.50)}$$

and matrix \mathbf{A}_D is an $L \times L$ diagonal matrix, having entries

$$\mathbf{A}_{D_{i,j}} = \begin{cases} \left(\frac{1}{z_l} \right)_j |\Gamma_l|, & \text{for } i = j \\ 0, & \text{otherwise} \end{cases} \quad i, j = 1, \dots, L \quad \text{Eq.(2.51)}$$

Hence, Eq.(2.45) can be rewritten including the previous components as,

$$\begin{bmatrix} \mathbf{A}_M + \mathbf{A}_Z & \mathbf{A}_W \\ \mathbf{A}_W^T & \mathbf{A}_D \end{bmatrix} \begin{bmatrix} \Phi \\ \mathbf{V} \end{bmatrix} = \begin{bmatrix} \mathbf{0} \\ \mathbf{I} \end{bmatrix} \quad \text{Eq.(2.52)}$$

and solved for the approximated potential distribution $\Phi = [\varphi_1, \dots, \varphi_n]^T$. The vector $\mathbf{x} \in \mathbb{R}^{n+L \times 1}$ has the form $\mathbf{x} = [\Phi \ \mathbf{V}]^T$ where $\Phi \in \mathbb{R}^n$ is the nodal potential distribution in the interior of the medium and $\mathbf{V} = [V_1, \dots, V_L]^T \in \mathbb{R}^L$ are the potentials on the boundary electrodes. The derivations of the matrix \mathbf{A} and composing sub-matrices for a simple 2D domain are shown in Appendix A.

The previous configuration is often referred to as the *Neumann-to-Dirichlet* mapping [1]. That is, the injected current, governed by the Neumann boundary condition, is the fixed known quantity, whilst the electric potentials at the surface, governed by Dirichlet condition, are the primary unknown quantity. The *Dirichlet-to-Neumann* mapping can also be considered for the solution of the forward problem, however, it is intuitive that controlling the current injected into the body, while fixing the voltages at the boundary is purely dictated by Ohm's law, therefore, increasing the risk of injecting excessive amounts of electrical current into the body and threatening the validity of EIT in the medical/clinical context.

2.5 Current injection and data collection strategies in EIT

Once the forward problem, demonstrated in Eq.(2.45), has been constructed, and prior to solving the system, the conditions expressed by Eq.(2.27) and Eq.(2.28) should be imposed in order to preserve the existence and the uniqueness of the forward problem solution [27]. If \mathbf{I}_l is the current injected by the l th electrode, then for a set of d driving current patterns

$$\mathbf{I}^{[d]} := (\mathbf{I}^{(1)}, \mathbf{I}^{(2)}, \dots, \mathbf{I}^{(d)}) \quad \text{Eq.(2.53)}$$

where $\mathbf{I}^{[d]} \in \mathbb{R}^{L \times d}$, the law of charge conservation theorem is imposed as,

$$\int_{\partial\Omega} j = \sum_{i=1}^d \mathbf{I}^{(i)} = 0 \quad \text{Eq.(2.54)}$$

In other words, each of these currents should sum up to zero, which means that the total amount of current entering the medium is equal to that exiting it.

Intuitively, varying the number of stimulation patterns directly affects the number of required solutions for Eq.(2.52). Given that EIT is typically concerned with large scale Finite Element systems, ‘short patterns’ (i.e., for small d) are favoured as they would offer significant computational savings. Hence, it is not hard to infer that the role of the stimulation pattern $I^{[d]}$ is of great computational significance.

The different current stimulation strategies in EIT are mainly divided into two categories: the pair drive or multi–electrode drive schemes. In the pair drive schemes [34], electrical current is mainly injected into the medium through a pair of adjacent or opposite electrodes. From one hand, it has been proven that their effectiveness differs depending on the application. On the other, the multi–electrode injection protocols [20] adopt the same strategy of injecting but on multi–electrode groups, either opposite or adjacent. Multi–injection protocols have the advantage of collecting a reduced number of measurements. In the fourth chapter injection protocols are analysed and their performance studied.

The hardware of current EIT systems is mainly manufactured to serve pair–drive schemes. However, although this study proves that the multi–electrode drive protocol shows superiority in performance in terms of voltage measurements inquisition time and number, the use of an EIT system that employs multi–electrode driving patterns is still not available.

Further, whether a pair– or multi–electrode drive scheme is to be used, available data acquisition strategies are essentially the same; as there are mainly two collection methods referred to as, the two–electrode and the 4–electrode collection strategies. In

the first approach voltages are measured through the same electrode from which the current is fired, and in the second, according to a specific configuration, the current is injected through some electrodes, and the voltage is measured across other electrodes. The second method has the advantage of minimising the error in the voltage measurements. For simplicity, the pair–electrode drive is used throughout.

2.5.1 Adjacent method

The adjacent data collection strategy [34] is the most commonly used 4–electrode method. According to this injection criterion, the current is injected through an adjacent pair of the electrodes, and the voltages are then measured across the rest of the electrode pairs. Figure 2.2 shows the concept of the adjacent collection method in a 2D medium [35].

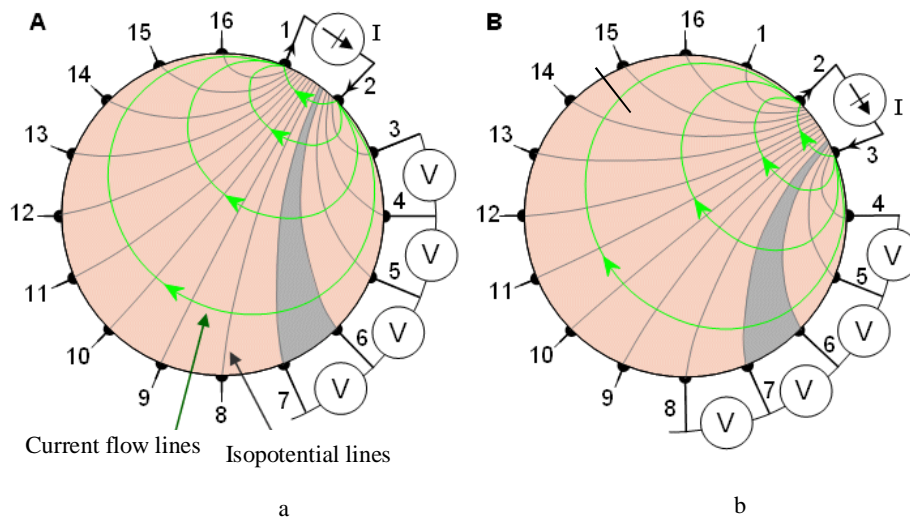


Figure 2.2 Adjacent method of data collection for a 16-electrode configuration system. For each stimulation pattern, 13 voltage measurements are collected from non-injecting electrodes (a) First set of injected current $\mathbf{I}^{(1)}$. (b) Second set of injected current $\mathbf{I}^{(2)}$.

The next stimulation pattern is then achieved when the injecting pair moves clock– or counter clock– wise by one electrode, and the second set of data can be therefore collected across the rest of the electrodes and so on.

It can also be seen from Figure 2.2, assuming L electrodes are available, that for each stimulation pattern $(L-3)$ voltage measurements can be collected, i.e., a total of $L(L-3)$ measurements will be available, half of which are linearly independent.

2.5.2 Opposite method

In the opposite method [36], the current is fired through opposite pairs of electrodes, as shown in Figure 2.3 [35], and voltages are measured across the rest of the electrodes. This configuration results in $(L-4)$ measurements for each stimulation pattern, totalling $L(L-4)$ measurements. Again, half of these measurements are linearly independent.

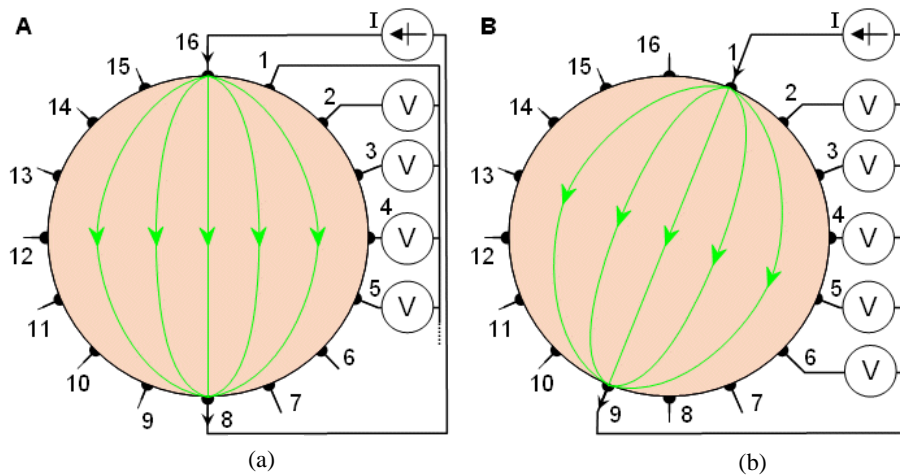


Figure 2.3 Opposite method of data collection for a 16-electrode configuration system. For each stimulation pattern, 12 voltage measurements are collected from non-injecting electrodes. (a): First stimulation pattern $I^{(1)}$, (b): Second stimulation pattern $I^{(2)}$.

In contrast to the adjacent method, whose sensitivity (higher current density) is only at its maximum near the area of the electrodes, the opposite method has a more uniform current density throughout the medium and therefore, good sensitivity in the central areas.

2.5.3 Adaptive method

In the adaptive method [37], currents are fired at once from all electrodes. Then, the voltages are measured with respect to a single electrode. This configuration requires a handful of current sources in order to inject this amount of current. An electrical current between -5 to $+5$ mA is traditionally injected, allowing for different current patterns. For a 16-electrode model, as shown in Figure 2.4, a total of 15-voltage measurements are collected for each stimulation pattern. The current pattern rotates

around one electrode by $22.5^\circ (360^\circ / 16)$. Therefore, 8–distinct current patterns are resulted, totalling $8 \times 15 = 120$ independent voltage measurements.

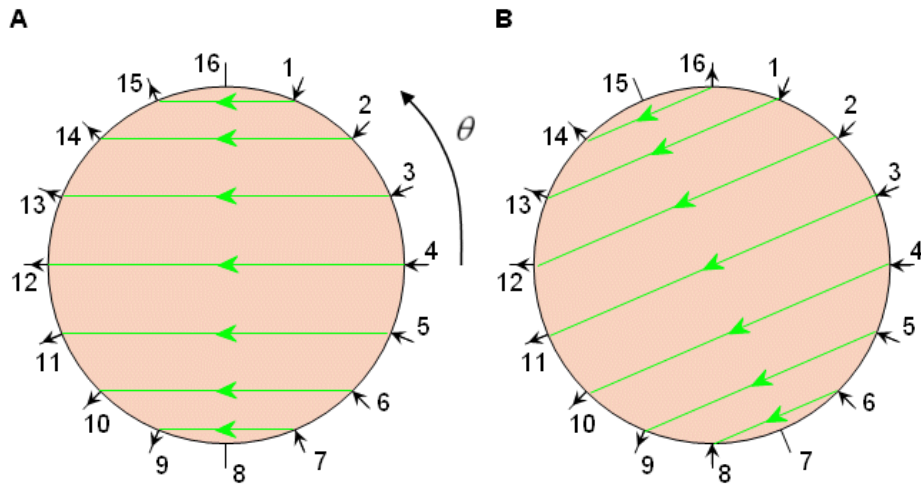


Figure 2.4 Adaptive method of data collection for a 16-electrode configuration system. For each stimulation pattern, 15 voltage measurements are collected from non-injecting electrodes. (a): First stimulation pattern $\mathbf{I}^{(1)}$, (b): Second stimulation pattern $\mathbf{I}^{(2)}$.

The problem of using a large number of current sources to operate this type of stimulation strategy can be avoided by utilising a single current source that can be switched, using a multiplexer, between the electrodes. The resulting measurements can be collected by using a single voltage measurement circuit multiplexed over the electrodes [38].

The choice of selecting an ‘optimum’ driving current pattern, which may contribute in enhancing the spatial resolution of the reconstructed images, has captured the interest of many researchers. However, it has been advocated in [37] that the pair–drive protocols lose their ability to distinguish between different conductivities as the size of the boundary reduces. In the same spirit, Gisser *et al* [37] proposed a trigonometric current pattern to enhance the ‘distinguishability’ of several admittivities within the volume of interest. Although the proposed protocol requires complex hardware for implementation, a superiority in performance has been advocated in [18], [39], and [40]. Similarly, another approach was suggested in [39], which exploits the role of adaptive current pattern generator in increasing the density of the current in areas where an inhomogeneity is expected to exist.

However, the appropriate choice for the injection protocol is directly related to the surrounding conditions, and the imposed restrictions. From a biomedical application point of view, if the electrical currents are to be injected into a living being, the excitation conditions have to comply with the IEEE safety regulations [41], [42]. These are mainly related to the ‘maximum current value’ injected into the body; this specially provides a formula for the maximum allowable current amplitude as a function of the frequency of the current signal.

2.6 Solving the linear system of the forward problem

In order to solve the system in Eq.(2.52) i.e., obtain a unique solution, some modifications can be introduced into the systems due to its rank deficient nature that is, the governing system matrix \mathbf{A} is not full-rank and in turn, has a family of solutions that satisfy the system and therefore prior information is needed to achieve this uniqueness.

One way to achieve this uniqueness in Eq.(2.52) is for the voltages to sum up to zero, or as proposed in [40], a set of measurements that satisfy condition Eq.(2.28) can be obtained by modifying the \mathbf{A}_w and \mathbf{A}_w^T blocks in Eq.(2.52) in such a way that when they are multiplied by the current patterns the potentials on the electrodes sum up to zero.

There are variety of methods to solve systems such as Eq.(2.52). However, there is no single method that is best for systems. These methods are normally determined according to speed and accuracy. In this case, speed is an important factor in solve the resulted forward problem system due to its large scale nature and this includes the amount of computations involved in solving such a system which is normally huge. Another issue is the accuracy for the solution rounding off error involved in these computations. These methods are normally divided into

- Direct Methods
- Iterative methods

CHAPTER 2. THE EIT FORWARDPROBLEM

Direct methods [43] are not appropriate for solving large number of equations in a system, particularly when the system matrix is sparse, i.e. when the majority of the elements in a matrix are zeroes. However, Iterative methods are best suited for solving systems with large number of equations. Iterative methods are very effective concerning computer storage and time requirements.

One of the main advantages of using iterative methods is that they require lesser multiplications for large systems. Another advantage is that they can be implemented in smaller programmes than direct methods with fewer round-off errors.

In contrast, direct methods normally aim to calculate an exact solution in a finite number of operations whereas iterative methods begin with an initial approximation and reproduce usually improved approximations in an infinite sequence which limit is the exact solution.

Direct methods work best for systems in which most of the entries are non-zero whereas iterative methods are appropriate for large sparse systems which mostly contain zeroes. Even when direct methods exist we should give priority to iterative methods because they are fast and efficient.

2.6.1 Direct methods

The linear system demonstrated in Eq.(2.55), can be solved using direct methods such as LU-factorisation [44]. However, the Cholesky method is considered better suited than the LU-factorisation technique; due to its exploitation of the sparsity and symmetry properties of the coefficient matrix \mathbf{A} . In Cholesky factorisation, \mathbf{A} can be factored into \mathbf{LL}^T , where \mathbf{L} is a lower triangular matrix, thus equation Eq.(2.55) becomes

$$\mathbf{LL}^T \mathbf{x} = \mathbf{b} \quad \text{Eq.(2.56)}$$

Then by assuming that $\mathbf{\vartheta} = \mathbf{L}^T \mathbf{x}$, one opts to solve the following linear system using the forward and backward substitution

$$\mathbf{L}\mathbf{\vartheta} = \mathbf{b} \quad \text{Eq.(2.57)}$$

$$\mathfrak{g} = \mathbf{L}^T \mathbf{x} \quad \text{Eq.(2.58)}$$

The numerical cost associated with this factorisation is of $O(n^3)$, while for the backward and forward substitution have a cost of $O(n^2 f)$ for f right hand sides.

2.6.2 Iterative methods

As mentioned previously, iterative methods are memory efficient and run quickly on sparse matrices rather than dense ones. When the system matrix \mathbf{A} is dense, then, the best course of action is to factor \mathbf{A} and solve Eq.(2.55) by back substitution as the time spent in factorising \mathbf{A} is roughly the same as when solving it iteratively.

The concept of iterative methods discussed in this context is based on the fact that if \mathbf{A} is symmetric and positive-definite, which is a true assumption for the resulting system matrix of the EIT forward problem, then the solution of Eq.(2.55) is the minimum of the quadratic equation

$$f'(\mathbf{x}) = \frac{d}{d\mathbf{x}} \left\{ \frac{1}{2} \mathbf{x}^T \mathbf{A} \mathbf{x} - \mathbf{b}^T \mathbf{x} + c \right\} \quad \text{Eq.(2.59)}$$

where c is a constant.

or,

$$f'(\mathbf{x}) = \frac{1}{2} \mathbf{A}^T \mathbf{x} + \frac{1}{2} \mathbf{A} \mathbf{x} - \mathbf{b} \quad \text{Eq.(2.60)}$$

and given the fact that \mathbf{A} is symmetric, Eq.(2.60) becomes

$$f'(\mathbf{x}) = \mathbf{A} \mathbf{x} - \mathbf{b} \quad \text{Eq.(2.61)}$$

Hence, by setting the gradient to zero, the linear equation in Eq.(2.55) is obtained. If one desires to find a solution for the system in Eq.(2.55), when matrix \mathbf{A} is nonsymmetric, iterative methods may be used to determine the solution of the system

$$\frac{1}{2} (\mathbf{A}^T + \mathbf{A}) \mathbf{x} = \mathbf{b} \text{ which is symmetric.}$$

2.7 The EIT inverse problem

Using conventional EIT modelling methods, the measured data y is essentially the result of the application of a measurement operator Π to the corresponding electrode potentials V as

$$\Pi(V) = y \quad \text{Eq.(2.69)}$$

As previously discussed, the forward problem is the process of mapping the change in the material conductivity inside a medium to the boundary voltage measurements, resulting from exciting a current pattern at its boundary. Mathematically speaking, this process is summarised by the nonlinear operator $\Lambda: L_2(\Omega) \rightarrow H^{1/2}(\partial\Omega)$,

$$\Lambda(\sigma) = y \quad \text{Eq.(2.70)}$$

which links the interior material conductivity $\sigma := \sigma(\mathbf{x}) \in L_2(\Omega)$, $\mathbf{x} \in \Omega$ with the observed data $y \in H^{1/2}(\partial\Omega)$.

On the other hand, the inverse problem in EIT is formed as the problem of estimating the unobserved material conductivity $\sigma(\mathbf{x})$ from an observable y . From an optimisation point of view, as the main aim is to find the model through which the measured voltages y , the simplest way is to minimise the quadratic minimisation functional, which is the minimum of the sum of squared errors,

$$\arg \min_{\sigma} \frac{1}{2} \|\Lambda(\sigma) - y\|_2^2 \quad \text{Eq.(2.71)}$$

Therefore, a natural step will be the linearisation of operator Λ . This can be done through linearising the forward problem around a reference conductivity distribution σ_0 . Further, using Taylor expansion as

$$\begin{aligned} \Lambda(\sigma) &= \Lambda(\sigma_0) + \left. \frac{\partial \Lambda}{\partial \sigma} \right|_{\sigma=\sigma_0} (\sigma - \sigma_0) + \left. \frac{\partial^2 \Lambda}{\partial \sigma^2} \right|_{\sigma=\sigma_0} (\sigma - \sigma_0)^2 + \text{HOT} \\ &\approx \Lambda(\sigma_0) + \nabla \Lambda(\sigma_0)(\sigma - \sigma_0) + O(\sigma^2) \end{aligned} \quad \text{Eq.(2.72)}$$

and ignoring the higher-order terms (HOT), Eq.(2.72) can be rewritten as

$$\Lambda(\sigma) - \Lambda(\sigma_0) = \nabla \Lambda(\sigma_0)(\sigma - \sigma_0) + \underbrace{O(\sigma^2)}_{\approx 0 \text{ for simplicity}} \quad \text{Eq.(2.73)}$$

denoting $\nabla\Lambda(\sigma_0)$ by $\Lambda^{(1)}(\sigma_0)$ results in

$$\underbrace{\Lambda(\sigma) - \Lambda(\sigma_0)}_{\delta y} = \underbrace{\Lambda^{(1)}(\sigma_0)}_J \underbrace{(\sigma - \sigma_0)}_{\delta\sigma} \quad \text{Eq.(2.74)}$$

or simply,

$$\delta y = J \delta\sigma \quad \text{Eq.(2.75)}$$

where δy represents the difference in measured voltages at the boundary for difference conductivity distribution σ and the known σ_0 or at $\delta\sigma$ and $J = \Lambda^{(1)}(\sigma_0)$ is essentially the first-order Fréchet differentiation of the nonlinear operator Λ at σ_0 :

$$\Lambda^{(1)}(\sigma_0) = \left. \frac{\partial\Lambda_j}{\partial\sigma_i} \right|_{\sigma=\sigma_0} \quad \text{Eq.(2.76)}$$

Clearly, the dimensionality of the J is determined by the dimensionality of the unobservable distribution σ and the measured data y .

Eq.(2.75) represents the EIT *linearised inverse problem* for the perturbation of σ about $\sigma = \sigma_0$.

For the inverse problem to be solved, and for simplicity reasons, one can eliminate the second-order derivative terms from the Taylor expansion of the forward problem demonstrated in Eq.(2.75). This would construct a generalised inverse of the Jacobian, and subsequently it would be possible to invert the well-posed problem using the Newton-Raphson method. This approach is often referred to as the Gauss-Newton method [45], which is the approach followed in the simulation studies in this thesis.

The Gauss-Newton method is one of a class of iterative methods used to calculate the potential distribution for a given conductivity distribution and an injected current pattern. It also iteratively calculates the conductivity until a predefined error between the measured and computed potentials on the electrodes is obtained. Hence, we define

$$\mathbf{y}(\mathbf{I}^{[d]}) = \left[\mathbf{y}(\mathbf{I}^{(1)}) \quad \mathbf{y}(\mathbf{I}^{(2)}) \quad \dots \quad \mathbf{y}(\mathbf{I}^{(d)}) \right] \in \mathbb{R}^{m \times d} \quad \text{Eq.(2.77)}$$

CHAPTER 2. THE EIT FORWARDPROBLEM

as the vector containing m measured voltages for d current patterns, and the vector $\mathbf{y}_{fwd}^{(\boldsymbol{\sigma})}$ which contains the electrode voltages for the same stimulation patterns, computed using FEM at conductivity $\boldsymbol{\sigma}$ ($\boldsymbol{\sigma}$ is a vector of length K , the number of finite elements in the mesh). Moreover, an objective function Θ [45] is defined, projecting the error between the measured and calculated voltages as,

$$\Theta = \frac{1}{2} \left(\mathbf{y}_{fwd}^{(\boldsymbol{\sigma})} - \mathbf{y} \right)^T \left(\mathbf{y}_{fwd}^{(\boldsymbol{\sigma})} - \mathbf{y} \right) \quad \text{Eq.(2.78)}$$

which when minimised with respect to the conductivity gives

$$\frac{\partial \Theta}{\partial \boldsymbol{\sigma}} = \frac{1}{2} \left(\mathbf{y}'_{fwd}(\boldsymbol{\sigma}) \right)^T \left(\mathbf{y}_{fwd}^{(\boldsymbol{\sigma})} - \mathbf{y} \right) = 0 \quad \text{Eq.(2.79)}$$

where $\mathbf{y}'_{fwd}(\boldsymbol{\sigma})$ is the matrix containing the derivatives of the boundary voltages with respect to the conductivity $\boldsymbol{\sigma}$ as,

$$\mathbf{J}_{(d;m,K)} = \left[\mathbf{y}'_{fwd}(\boldsymbol{\sigma}) \right] = \frac{\partial \mathbf{y}^{(d,m)}}{\partial \boldsymbol{\sigma}} \quad \text{Eq.(2.80)}$$

and termed, the *Jacobian matrix* \mathbf{J} , which is an $md \times K$ rectangular matrix.

The elements of this matrix, $\mathbf{J}_{(d;m,k)} = \frac{\partial V_{dm}}{\partial \sigma_k}$ are the partial derivatives of the electrode voltage V_{dm} with respect to the conductivity σ_k of element Ω_k at the d th current pattern.

By calculating the Taylor expansion of Eq.(2.79) and ignoring the higher order terms, the correction to the conductivity at the c th iteration can be calculated using the following iterative formula

$$\Delta \boldsymbol{\sigma}_c = - \left[\mathbf{J}_c^T \mathbf{J}_c \right]^{-1} \left[\mathbf{J}_c^T \left(\mathbf{y}_{fwd}^{(\boldsymbol{\sigma})} - \mathbf{y} \right) \right] \quad \text{Eq.(2.81)}$$

Further, the conductivity update, $\Delta \boldsymbol{\sigma}_c$, at each iteration c of the nonlinear algorithm is calculated by solving the following linear system of equations

$$\left(\mathbf{J}_c^T \mathbf{J}_c \right) \Delta \boldsymbol{\sigma}_c = - \mathbf{J}_c^T \left(\mathbf{y}_{fwd}^{(\boldsymbol{\sigma})} - \mathbf{y} \right) \quad \text{Eq.(2.82)}$$

The updated conductivity distribution at iteration d is obtained by

$$\boldsymbol{\sigma}_{c+1} = \boldsymbol{\sigma}_c + \Delta \boldsymbol{\sigma}_c \quad \text{Eq.(2.83)}$$

Finally, when the change in conductivity values falls below a predetermined tolerance, the solution is considered to have converged and the algorithm can be stopped.

2.7.1 Calculating the Jacobian matrix

As has been shown before, the Jacobian matrix of Eq.(2.80) is essentially the first order Fréchet differentiation of the nonlinear operator Λ at σ_0 . The Jacobian can be obtained in many ways. The author in [40] was the first to complete the derivation of the Jacobian matrix, this method is referred to as the *standard model*. It is mainly based on the solution obtained from the forward model. Considering the system of linear equations in Eq.(2.55)

$$\mathbf{Ax} = \mathbf{b} \quad \text{Eq.(2.84)}$$

Then, the k th column of the Jacobian can be obtained by differentiating the solution \mathbf{x} of the system Eq.(2.84) with respect to the conductivity σ_k

$$\frac{\partial \mathbf{x}}{\partial \sigma_k} = \frac{\partial (\mathbf{A}^{-1} \mathbf{b})}{\partial \sigma_k} \quad \text{Eq.(2.85)}$$

Using the differentiation product rule, the right hand side of Eq.(2.85) can be expressed as

$$\frac{\partial (\mathbf{A}^{-1} \mathbf{b})}{\partial \sigma_k} = -\mathbf{A}^{-1} \frac{\partial \mathbf{A}}{\partial \sigma_k} \mathbf{A}^{-1} \mathbf{b} = -\mathbf{A}^{-1} \frac{\partial \mathbf{A}}{\partial \sigma_k} \mathbf{x} \quad \text{Eq.(2.86)}$$

where the derivative $\frac{\partial \mathbf{A}}{\partial \sigma_k}$ has the elements, by using Eq.(2.46)

$$\frac{\partial \mathbf{A}_{K,i}}{\partial \sigma_k} = \int_{\Omega_k} \nabla N_K \nabla N_i d\Omega_k \quad \text{Eq.(2.87)}$$

Given the fact that the matrix $\frac{\partial \mathbf{A}}{\partial \sigma_k}$ is sparse, as it only contains the contributions

from the k th element, without being multiplied by σ_k . This matrix is then multiplied by the solution \mathbf{x} which holds the values of potential distributions at the nodes, which in turn produces a column vector that has non-zero elements only in those rows corresponding the node numbers of the k th element. The matrix \mathbf{A}^{-1} which has been

factored in the forward solution can be used again to solve a new system, whose solution contains the derivatives of all potentials with respect to the conductivity of the k th element. Since Eq.(2.85) produces the derivatives of all potentials, the part which includes the electrodes' potentials has to be excluded. The Jacobian matrix has a size of $md \times K$ block matrix (m is the number of measurements collected for each stimulation pattern, d is the number of stimulation patterns, and K is the number of finite elements constituting the mesh).

2.8 Summary

In this chapter, the concept of the EIT forward problem has been discussed, along with the EIT's main electrode configurations highlighting on their pros and cons with regards to the real life resemblance. The Finite Element Methods has been used to solve the EIT forward problem utilising the boundary conditions and current stimulation patterns. The resulting weak formulation was produced and discretised using the standard Galerkin method to produce a linear set of equations $\mathbf{Ax}=\mathbf{b}$, and touching on how to solve such matrices either analytically or iteratively.

The chapter has also discussed techniques of current injection and data collection strategies in EIT such as the adjacent, opposite and adaptive method. An introduction to the multi-electrode injection pattern was briefly mentioned as compared against the single-electrode method.

The EIT linearised inverse problem and Jacobian matrix have been formulated as a result of a conductivity perturbation inside the medium. This paves the way for a discussion of the reconstruction problem in Chapter three.

Chapter 3

The EIT image reconstruction problem

As far as the propositions of mathematics refer to reality they are not certain, and so far as they are certain, they do not refer to reality.

Albert Einstein

In this chapter, the linearised EIT inverse model, Jacobian Matrix and other assumptions will be further discussed and incorporated to establish the setting of the EIT Inverse Problem. In which process, a differential conductivity image of a given medium containing an object/phenomena is produced by solving the system containing the Jacobian, current stimulation pattern and voltage difference at the boundary of the medium.

However, this is not a straightforward problem due to the system being underdetermined; which means fewer measurements than unknowns since there is only a finite set of measurements that can be collected at the medium's periphery. The resulting Jacobian matrix is also ill-conditioned with a high condition number; this means a simple inverse of the Jacobian matrix would not simply do the trick.

Afterwards, a process referred to as *Regularisation* is deployed in order for the linearised problem to produce meaningful and stable solutions. This chapter proceeds to discuss various regularisation techniques, conditions and assumptions which help in enhancing the image reconstruction process.

3.1 Introduction

In terms of functional analysis [46], inverse problems are typically continuous, and numerical instability may arise when solved with finite precision, or when errors exist in the data.

However, in order for inverse problems to produce stable solutions, they must be converted into well-posed ones. In order to do so, the problems need to be reformulated for numerical treatment. Typically, this involves including additional prior assumptions on the behaviour of the solution.

Various algorithms have been suggested to deal with the inverse problem that arises in EIT and fall into the broad categories of single-step or direct and iterative algorithms.

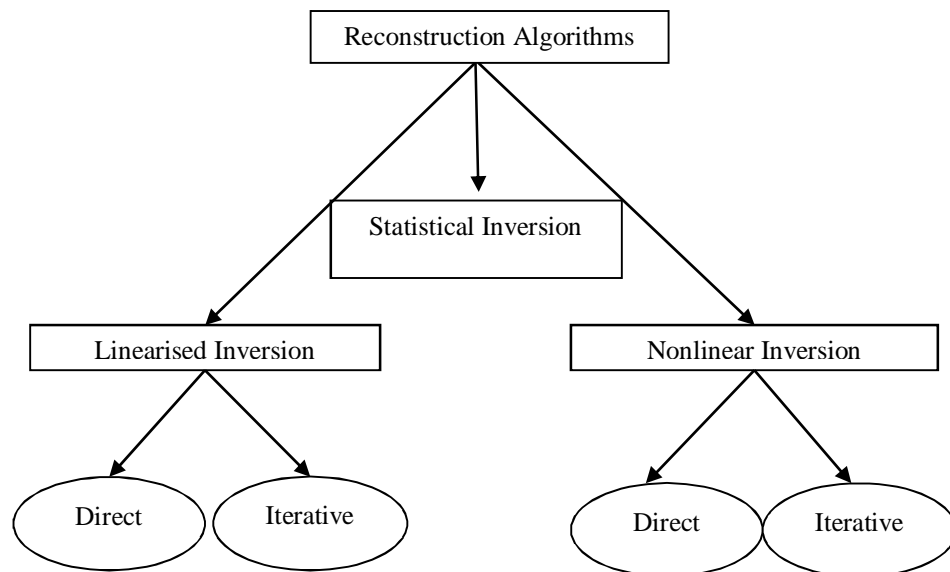


Figure 3.1 Groups of Reconstruction algorithms [47]

Figure 3.1 gives a categorisation of the types of already available reconstruction algorithms for the EIT problem. These are generally divided in probabilistic-statistical methods [40] and [48]–[50], deterministic methods based on linearisation [40] and [51]–[59], and the deterministic nonlinear inversion methods [60]–[68].

CHAPTER 3. THE EIT IMAGE RECONSTRUCTION PROBLEM

The algorithms suitable for solving the linearised inverse problem are subdivided into the direct methods that use a single regularisation step, such as the Tikhonov regularisation [46], and iterative methods which regularise iteratively such as the Conjugate Gradients algorithm (CG) [69]. Nonlinear algorithms, on the other hand, are capable of reconstructing high-contrast inhomogeneities, and are mostly iterative, typically Newton-type approaches with a linear regularisation step.

Numerical algorithms suitable for the inverse conductivity problem are those explicitly designed to treat the ill-conditioning and rank-deficiency of the Jacobian matrix.

An indication of the degree of ill-conditioning of the Jacobian matrix can be obtained by evaluating its condition number. The condition number is essentially a measure of well-posedness of the discrete system and is defined as the ratio of its largest singular value to its smallest one, giving a measurable figure of the span of its singular values [69]. Matrices with a relatively small condition number are said to be well-conditioned with respect to inversion, and maintain their singular values clustered together. In EIT, the Jacobian matrix tends to be heavily ill-conditioned. In effect [5],

- the Jacobian matrix does not have a well-defined inverse
- the solution resulting from applying the least-squares approach to the inverse problem, is a highly unstable function of the measurements, violating Hadamard's third criterion [5]
- the reconstruction problem is generally underdetermined, due to the clustering of the Jacobian matrix extremely small singular values
- a meaningful and stable inverse solution can be computed with the help of regularisation

3.2 The linearised inverse problem

As discussed in Chapter 2, the EIT inverse problem is formed as the problem of estimating the unobserved distribution σ from the observable measurements y as,

$$\Lambda(\sigma) = y \quad \text{Eq.(3.1)}$$

where $\Lambda: L_2(\Omega) \rightarrow H^{1/2}(\partial\Omega)$ is the nonlinear operator mapping the real conductivity of the medium onto the boundary voltage measurements, σ is the conductivity distribution inside the medium, and y is the observed boundary data.

It was also shown that, by taking the Taylor expansion of the quadratic minimisation functional $\min_{\sigma} \frac{1}{2} \|\Lambda(\sigma) - y\|_2^2$, where $\|\cdot\|$ is the ℓ_2 norm, the following linear system results

$$J\delta\sigma = \delta y \quad \text{Eq.(3.2)}$$

where J is essentially the first-order Fréchet differentiation of the nonlinear operator Λ at a conductivity distribution σ_0 . Clearly, the dimensionality of J is determined by the dimensionality of the unobservable distribution σ and the measured data y . Therefore, Eq.(3.2) represents the EIT linearised inverse problem.

In the typical EIT fashion, the measured data vector is contaminated with some noise originating from various physiological, modelling and discretisation errors. Without loss of generality, the noise ε is assumed to be additive,

$$J\delta\sigma = \delta y + \varepsilon \quad \text{Eq.(3.3)}$$

In the discrete setting, where only a finite set of measurements \mathbf{y}_{fwd} can be collected, the number of the corresponding discretised equations from of Eq.(3.3) is finite as

$$\mathbf{J}\delta\sigma = \delta\mathbf{y}_{fwd} + \varepsilon \quad \text{Eq.(3.4)}$$

where $\mathbf{J} \in \mathbb{R}^{m \times K}$ is the discrete equivalent of J , $\delta\mathbf{y}_{fwd} \in \mathbb{R}^m$ is a vector containing the finite collected measurements, and $\delta\sigma \in \mathbb{R}^K$ is the discretised conductivity distribution across the medium, as it is assigned values over the faces of the K finite elements.

On the other hand, since the number of discretisation variables for σ typically outnumbers the dimensionality of the measurements, one encounters a heavily underdetermined problem. From the least squares point of view, the solution of Eq.(3.4), in its discrete form, comes as the following minimisation problem holds,

$$\arg \min_{\sigma} \left\| \mathbf{J} \delta \sigma - (\delta \mathbf{y}_{fwd} + \varepsilon) \right\|_2^2 \quad \text{Eq.(3.5)}$$

Unfortunately, the above solution is of little practical/numerical use as matrix \mathbf{J} is a dense, rectangular and ill-conditioned matrix, hence prone to numerical and measurement errors. Thus, matrix $(\mathbf{J}^T \mathbf{J})$ is severely ill-conditioned. However, one way of avoiding this problem is by applying a selection rule or additional constraints.

For instance, among all vectors minimising the norm of $\left\| \mathbf{J} \delta \sigma - (\delta \mathbf{y}_{fwd} + \varepsilon) \right\|_2^2$, one may seek the vector having minimum norm or the vector having maximum entropy. This amounts to solving the following optimisation problem

$$\arg \min_{\sigma} \left\{ \xi(\sigma) \mid \mathbf{J}^T \mathbf{J} \delta \sigma = \mathbf{J}^T \delta \mathbf{y}_{fwd} \right\} \quad \text{Eq.(3.6)}$$

Here, $\xi(\sigma)$ is the norm of σ or the negative of the entropy of σ or any other criteria leading to a unique solution.

3.3 Singular Value Decomposition

Singular Value Decomposition (SVD) [69] is the generalisation of orthogonal diagonalisation of the Hermitian matrices. Its importance to the EIT applications stems from its fast and guaranteed convergence.

Let us consider the linearised discrete system of Eq.(3.4), and drop the use of the δ – term in $\delta \sigma$ and $\zeta \mathbf{y}_{fwd}$ for notational convenience, hence Eq.(3.4) becomes,

$$\mathbf{J} \sigma = \mathbf{y}_{fwd} + \varepsilon \quad \text{Eq.(3.7)}$$

which is an underdetermined system as $\mathbf{J} \in \mathbb{R}^{m \times K}$, $m \leq K$ where m is the number of collected measurements and K is the number of finite elements comprising the discretised medium. The SVD of matrix \mathbf{J} is,

$$\mathbf{J} = \mathbf{P}\mathbf{\Xi}\mathbf{Q}^T = \sum_{i=1}^m \mathbf{p}_i \zeta_i \mathbf{q}_i^T \quad \text{Eq.(3.8)}$$

where $\mathbf{P} = (\mathbf{p}_1, \mathbf{p}_2, \dots, \mathbf{p}_m)$ and $\mathbf{Q} = (\mathbf{q}_1, \mathbf{q}_2, \dots, \mathbf{q}_K)$ are matrices with orthonormal columns, i.e., $\mathbf{P}^T \mathbf{P} = \mathbf{Q}^T \mathbf{Q} = \mathbf{I}$, called the left and right singular vectors, respectively. The non-negative entries of the diagonal matrix $\mathbf{\Xi}$ or ζ_i are typically sorted in a non-increasing order as $\zeta_1 \geq \zeta_2 \geq \dots \geq \zeta_m \geq 0$ and are identified as the singular values.

Using SVD, one may determine a generalised inverse \mathbf{J}^\dagger for \mathbf{J} , corresponding to the different properties which can be imposed on \mathbf{J} . In effect, one may obtain \mathbf{J}^\dagger as

$$\mathbf{J}^\dagger = \mathbf{Q}\mathbf{\Xi}^{-1}\mathbf{P}^T = \sum_{i=1}^{n_\dagger} \mathbf{q}_i \zeta_i^{-1} \mathbf{p}_i^T \quad \text{Eq.(3.9)}$$

where

$$n_\dagger := \begin{cases} m, & \text{if } \mathbf{J} \text{ is invertible,} \\ n_r = \text{rank}(\mathbf{J}), & \text{if } \mathbf{J} \text{ is } n_r \text{-rank-deficient.} \end{cases} \quad \text{Eq.(3.10)}$$

The first case assumes that \mathbf{J} is of full rank and effectively corresponds to the so called generalised Moore–Penrose pseudo inverse [15]. In the second case, which reflects the EIT problem, \mathbf{J} is assumed to be n_r -rank deficient, which implies that some of the smallest singular values are practically zero, i.e. $\zeta_1 \geq \dots \geq \zeta_{n_r} \geq \zeta_{n_r+1} \approx \dots \approx \zeta_m \approx 0$. Based on SVD, the generalised or Moore–Penrose solution can be written in the following form [15]

$$\boldsymbol{\sigma}_\dagger = \mathbf{J}^\dagger \mathbf{y}_{fwd} = \sum_{i=1}^{n_\dagger} \frac{\mathbf{p}_i^T \mathbf{y}_{fwd}}{\zeta_i} \mathbf{q}_i \quad \text{Eq.(3.11)}$$

From Eq.(3.11), one may study the contribution of the singular values ζ_i and the solution $\boldsymbol{\sigma}_\dagger$ and in fact, understand how SVD provides an insight into the ill-posedness problem. Generally speaking, should one attempt to invert small singular values $\zeta_i \approx 0$, the solution $\boldsymbol{\sigma}_\dagger$ would attract considerable high values, effectively obscuring the desired solution. In this respect, even a small perturbation in \mathbf{y}_{fwd} can cause a dramatically high perturbation in $\boldsymbol{\sigma}_\dagger$ as the tiny values of ζ_i would eventually prevail, rendering the obtained solution meaningless.

3.4 Regularisation

The previously mentioned attempts, as described in Eq.(3.5) and Eq.(3.6), to reconstruct meaningful images, normally produce solutions that are unstable. In other words, a small perturbation in the data leads to an arbitrary perturbation in the solution. This is a direct violation of Hadamard's third condition [1]. Therefore, one must resort to the regularisation theory in order to determine a unique and stable solution. Formally, a slight modification of Eq.(3.5) is ought to take place in order to provide simultaneous adherence to uniqueness and stability. This can be achieved, as one seeks the solution to the following optimisation problem,

$$\arg \min_{\sigma} \left\| \mathbf{J} \delta \sigma - (\delta \mathbf{y}_{fwd} + \varepsilon) \right\|_2^2 + R(\sigma) \quad \text{Eq.(3.14)}$$

where $R(\sigma)$ is the artificially imposed prior information matrix.

From one hand, if $R(\sigma)$ is carefully selected, the corresponding solution will meet the desired physical and mathematical requirements. On the other, it is not feasible sometimes to find suitable prior information about the problem at hand, or restrict the solution to behave in such way that does not serve the purpose of the problem.

Regularisation can be employed in a variety of ways. Its main objective is to impose prior assumptions on the solution, and filter out the high frequency components of the solution, i.e., those corresponding to the smallest singular values of the Jacobian matrix. Having said this, one can reasonably question why, in a problem with an intrinsic lack of information, the sensitivity matrix is further truncated. Among the singular values of the Jacobian, the smallest ones are the most susceptible to noise. These are often very small and when perturbed by the noise signals and when inverted to produce the regularised solution they grow into very large noise signals, causing instability in the solution. To avoid this, their riddance is essential, a process which reduces the degree of ill-conditioning of the matrix. Removing singular values from the Jacobian causes the sensitivity to drop. However, this reduction becomes apparent in the spatial resolution of the images, only when some of the larger singular values are removed.

CHAPTER 3. THE EIT IMAGE RECONSTRUCTION PROBLEM

The existing deterministic algorithms in image reconstruction are mainly divided into two key categories; those suitable for the linearised problems and those solving the nonlinearised ones which to some extent encompass the first. The former category can be subdivided even further into the so-called direct methods, which calculate an ‘exact’ regularised solution in a single step such as Standard Tikhonov (ST) and Truncated Singular Value Decomposition (TSVD). While in the iterative methods, an approximation to the regularised inverse and solution is estimated in every iteration. Generally, nonlinear inverse solvers are iterative, although the purpose for iterating in the nonlinear schemes is defensible, their value in the linearised solvers is less evident.

However, the accuracy level must be accounted for prior to conducting any computations, either for the forward or the inverse problems. This is due to it being prone to the level of noise in the data, or to the errors introduced from the data acquisition system. Further, scientific complexity languages such as MATLAB have a set tolerance value for the calculations that is higher than the noise level present in real-life experimental conditions. This causes redundant refinements and pointless delays with no impact on the solution. Direct methods require the calculation of a regularised inverse, which is subsequently projected onto the measurements vector to provide the reconstructed image. Most of the computational power and time is consumed for the calculation of the regularised inverse to a high precision. This can be avoided by calculating the regularised inverse, and indeed the solution, iteratively, a process which can be monitored and terminated as soon as the measurement precision is reached.

The main iterative schemes used to solve ill-posed linearised problems include the Landweber iteration [70] and its regularised hybrids as well as the Conjugate Gradients iteration, which possesses intrinsic regularisation properties. Iterative solvers traditionally used for well-posed problems [69] may still be applied (although not preferred) but it is essential that these are terminated before they finally converge to the unstable LS solution. Iterations, linear and nonlinear, are often controlled by Morozov’s stopping criterion or discrepancy principle as it is otherwise known [71], according to which iterations should progress until,

$$\|\Lambda(\sigma) - y\| \leq \varepsilon$$

where ε is the estimated measurement error. In this way, regularisation is applied by essentially avoiding the calculation of the high-frequency components of the solution i.e., preventing the fitting of data which is likely to be contaminated by noise.

3.4.1 Standard Regularisation

The role of regularisation is to penalise solutions that according to some prior knowledge are unlikely. The general formulation of the regularised problem is given below [40]:

$$\arg \min_{\sigma} \left\{ \left\| \mathbf{L}_1 (\mathbf{J} \delta \sigma - \delta \mathbf{y}_{fwd}) \right\|_2^2 + \alpha \left\| \mathbf{L}_2 \delta \sigma \right\|_2^2 \right\} \quad \text{Eq.(3.15)}$$

where \mathbf{L}_1 is the square root of the weighting matrix $\mathbf{W}_1 = \mathbf{L}_1^T \mathbf{L}_1$, \mathbf{L}_2 a regularisation matrix, and $\alpha > 0$ is the regularisation parameter.

Various kinds of regularisation schemes include different selection of regularisation and weight matrices.

3.4.2 Truncated Singular Value Decompositions (TSVD)

As mentioned before, the basic idea of standard regularisation is to impose additional requirements on the characteristics of the solution. This effectively dampens the contributions from the errors introduced from the collected voltage measurements. The TSVD method achieves this by neglecting the components of the solution corresponding to the smallest singular values, as these contributions are mostly contaminated with error components and render the solution unusably large.

The least square solution of the linearised EIT inverse problem given in Eq.(3.4) [47],

$$\sigma_{LS} = \sigma_0 + \mathbf{Q} \mathbf{\Xi}^{-1} \mathbf{P}^T \mathbf{y}_{fwd} = \sigma_0 + \sum_{i=1}^{n_t} \frac{\mathbf{p}_i^T \mathbf{y}_{fwd}}{\zeta_i} \mathbf{q}_i \quad \text{Eq.(3.16)}$$

which is a reformulation of Eq. (3.11) by replacing $\boldsymbol{\sigma}^\dagger = \boldsymbol{\sigma}_{LS} - \boldsymbol{\sigma}_0$ where $\boldsymbol{\sigma}_0$ is the reference conductivity distribution and $\boldsymbol{\sigma}_{LS}$ is the medium's second state conductivity.

It is worth to note that the column $\mathbf{Q}(:,i)$ is the singular vector to the i th singular value s_i and

$$\Xi^{-1} = \text{diag}(\zeta_i^{-1}) = \begin{cases} 1/\zeta_i & \text{if } \zeta_i \neq 0 \\ 0 & \text{otherwise} \end{cases}$$

However, since \mathbf{J} is an ill-conditioned matrix, it is characterised by the presence of extremely small singular values, and from Eq.(3.16) it is clear that any error in the measurements \mathbf{y} will appear in the image components $\mathbf{p}_i^T \mathbf{y}_{fwd}$ drastically magnified. To avoid this situation, a regularised solution is calculated in truncated singular value decomposition (TSVD) [40] and [98], by setting the small singular values to zero after some threshold ι in order to obtain a unique and stable solution such as

$$\boldsymbol{\sigma}_{\text{TSVD}} = \boldsymbol{\sigma}_0 + \sum_{i=1}^{n_t} \tau_i \frac{\mathbf{p}_i^T \mathbf{y}_{fwd}}{\zeta_i} \mathbf{q}_i \quad \text{Eq.(3.17)}$$

with τ_i being a filter factor of the form

$$\tau_i = \begin{cases} 1, & i \leq \iota \\ 0, & i > \iota \end{cases} \quad \text{Eq.(3.18)}$$

The TSVD method is widely used in the EIT imaging applications where the high frequency components of the image i.e. image sharpness can be compromised, such Lung Imaging and Gastric Emptying.

3.4.3 Direct algorithms: Standard Tikhonov Regularisation

The Standard Tikhonov (ST) method is one of the common direct regularisation methods. They are naturally derived either from the probability theory or the trade-off analysis. Just like TSVD, ST incorporate some filters to remove the impact of the smallest singular values of the Jacobian and subsequently impose prior assumptions on the solution. The Tikhonov regularisation parameter α is analogous to the 'level of truncation' parameter used in the truncated decomposition in section 3.4.2. The

regularised solution $\boldsymbol{\sigma}_{ST}$ can be derived either from a probabilistic framework or from the TSVD. The regularisation matrix $R(\boldsymbol{\sigma})$ in Eq.(3.14), in the Tikhonov regime, is a constraint for a bounded solution $R(\boldsymbol{\sigma}) := \frac{1}{2}\alpha \|\boldsymbol{\sigma}\|_2^2$ or, more precisely, for a bespoke penalisation of non-smooth solutions as $R(\boldsymbol{\sigma}) := \frac{1}{2}\alpha \|\mathbf{D}\boldsymbol{\sigma}\|_2^2$, where \mathbf{D} is the differential operator. The selection of the optimal regularisation parameter and matrix is beyond the scope of this thesis but can be found in [98] and the references therein.

Due to its relevance to this work, the determination of the regularisation parameter α using the L-curve method is discussed in the next section.

Mathematically, the filter factor τ_i in Eq.(3.17) for the Tikhonov case becomes [98]

$$\tau_i = \frac{\zeta_i^2}{\zeta_i^2 + \alpha}, \text{ for } i = 1, \dots, m \quad \text{Eq.(3.22)}$$

Therefore, the standard Tikhonov solution is represented as

$$\boldsymbol{\sigma}_{ST} = \boldsymbol{\sigma}_0 + \sum_{i=1}^m \left(\frac{\zeta_i^2}{\zeta_i^2 + \alpha} \right) \frac{\mathbf{p}_i^T \mathbf{y}_{fwd}}{s_i} \mathbf{q}_i \quad \text{Eq.(3.23)}$$

3.4.3.1 The Regularisation parameter α

The choice of regularisation parameter is not a straightforward procedure and is usually associated with the *a priori* assumptions about the solution. As it is not reasonable to try to obtain a norm smaller than the error norm, the regularisation parameter is chosen such that the norm equals the norm of noise ε (discrepancy principle) [98]

$$\|\mathbf{J}\delta\boldsymbol{\sigma} - (\delta\mathbf{y}_{fwd} + \varepsilon)\|_2^2 = \|\varepsilon\|_2^2 \quad \text{Eq.(3.25)}$$

If the variance of noise is not known, more sophisticated methods are employed for the optimal selection of α such as the Quasi optimality criterion [72].

3.4.3.2 L-curve criterion

The L-Curve criterion [74] and [98] is a log-log plot of the norm of the regularised solution versus the resulting residual norm for each set of regularisation parameter values. Figure 3.2 shows a typical L-curve for a given problem. This plot often is in the shape of the letter L, from which it claims its name. The log-log scale emphasises the appearance of the L shape.

Clearly, the optimal regularisation parameter is located at the corner of the L curve, since for values higher than this, the residual increases rapidly and the norm of the solution decreases only slowly, while for values smaller than this, the norm of the solution increases rapidly without significant decrease in the residual. Hence, the solution is expected to be near the corner of the L shape to balance the regularisation and perturbation errors.

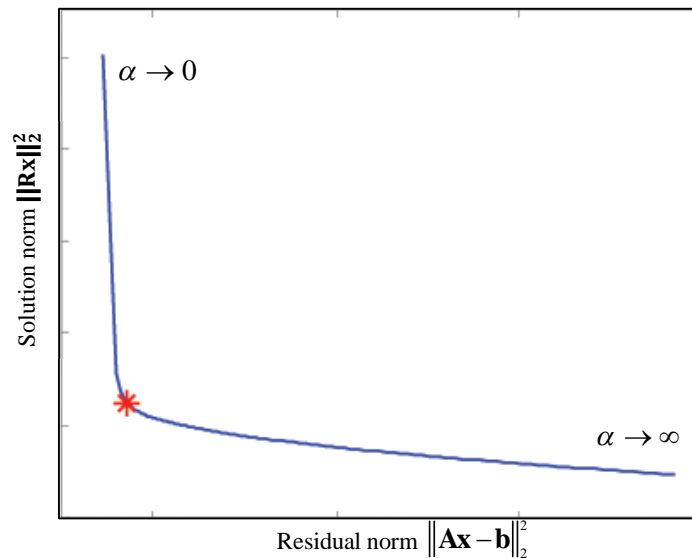


Figure 3.2 The L-curve of a specific problem, the L-curve is a log-log plot of the solution norm $\|\mathbf{R}\mathbf{x}\|_2^2$ versus the residual norm $\|\mathbf{A}\mathbf{x} - \mathbf{b}\|_2^2$

In practice, only a few points on the L-curve need to be computed, and the corner is located by estimating the point of maximum curvature [73].

Choosing an appropriate regularisation parameter is very difficult. Every parameter choice method has severe flaws; either they require more information than is usually available, or they fail to converge to the true solution as the error norm goes to zero.

For further discussion regarding parameter choice methods see [75], [76], [98] and the references therein.

3.4.4 Iterative regularisation techniques

As an alternative to the direct regularisation methods, one can advocate the possibility of applying regularisation iteratively. Indeed, many iterative algorithms have been published in the open literature. Amongst the iterative techniques are variants of the Newton–Raphson method [13], [7] and variants of the error function minimisation algorithm [56]. Error function minimisation algorithms minimise an error function based on the differences of potential distribution solutions compared to an initially assumed conductivity distribution. The conductivity distribution is updated by minimising the error function with a least squares technique. Such algorithms include the Wexler EIT algorithm and its variants [56], Fry and Neuman’s double constraint algorithm [70],[78], a variant [77] and the popular Conjugate Gradients (CG) method [79],[[80]-[81]. There seem to be two particular limitations, though highly disputable, to the iterative approach:

- the iterative process is thought of as being sensitive to noise and measurement errors
- convergence to a solution is observed to be quite slow and thus the image reconstruction process is computationally intensive

Iterative techniques are used to solve the 'static' reconstruction problem, i.e., finding the actual resistivity in the body rather than a change in resistivity. Various iterative schemes are already in use for solving the linearised inverse problem. Among them the Landweber and Kaczmarz algorithms are considered to be the more classical options, which are particularly useful for problems with large data sets.

3.4.4.1 The Landweber iteration

A good example of iterative regularisation methods is the Landweber iteration [70]. This algorithm was originally proposed for well-posed problems and takes the following form,

$$\min_{\sigma} \|\mathbf{J}\sigma - \mathbf{y}_{fwd}\|_2^2 \quad \text{Eq.(3.26)}$$

The $(n+1)$ th Landweber iteration is expressed as the following iterative formula

$$\sigma_{n+1} = \sigma_n + \omega \mathbf{J}^T (\mathbf{J}\sigma_n - \mathbf{y}_{fwd}) \quad \text{Eq.(3.27)}$$

where the relaxation parameter $\omega \in \mathbb{R}$ should satisfy the condition

$$2 \left(\|\mathbf{J}^T \mathbf{J}\|_2 \right)^{-1} > \omega > 0$$

As long as the current approximation of the solution σ_n is not too close to the true solution, the residual $\mathbf{J}\sigma_n - \mathbf{y}_{fwd}$ of the linear system is quite large and the data error in the right-hand side is negligible as compared to the size of the residual. It follows that the negative gradient of the LS functional, i.e. the Landweber step $\mathbf{J}^T (\mathbf{J}\sigma_n - \mathbf{y}_{fwd})$, essentially points to the right descent direction. As iterations progress, the value of the residual reduces and on the other hand the data error component gradually increases before it eventually dominates the objective function. The regularisation parameter in this case is the index of the iteration, which itself is ultimately controlled by Morozov's discrepancy principle [82], so that the residual and the error in the data are halted before they converge to an unstable LS solution. The major disadvantage of the Landweber iteration is its very slow convergence rate, especially when compared to the Conjugate Gradients method. In fact, the Landweber iteration in its standard form is too slow to be useful in practice. In a hypothetical scenario, if the Jacobian was an orthogonal matrix, the algorithm could have an optimum convergence rate. However as this is definitely not the case, the approximation $\mathbf{J}^T \approx \mathbf{J}^{-1}$ suggested by Kotre [83] in the 1990s is too crude, and the computational efficiency of the algorithm is radically compromised. In practise, the corresponding Landweber iteration filters are functions of the iteration number n ,

$$\tau_i^{(n)} = 1 - (1 - \omega \zeta_i^2)^n, \quad i = 1, \dots, m \quad \text{Eq.(3.28)}$$

where ζ_i is the i th singular value of \mathbf{J} . From Eq.(3.28) it is clear that the n th Landweber iterative solution can be computed directly as

$$\boldsymbol{\sigma}_n = \boldsymbol{\sigma}_0 + \sum_{i=1}^m \tau_i^{(n-1)} \frac{\mathbf{p}_i^T \mathbf{y}_{fwd}}{\zeta_i} \mathbf{q}_i \quad \text{Eq.(3.29)}$$

where \mathbf{p} , s , and \mathbf{q} are the SVD components of \mathbf{J} and \mathbf{y}_{fwd} is the boundary voltage measurement vector. A closer look at the iteration shows that the efficiency and indeed the performance of the algorithm can be vastly improved by swapping the scalar factor ω with a functional approximating the Hessian of the error residual. Possible options include $\mathbf{J}^T \mathbf{J}$ effectively forming the Moore–Penrose generalised inverse, or even better $(\mathbf{J}^T \mathbf{J} + \alpha \mathbf{I})^{-1}$ which leads to the so called iterative Tikhonov regularisation.

$$\boldsymbol{\sigma}_{n+1} = \boldsymbol{\sigma}_n + (\mathbf{J}^T \mathbf{J} + \alpha \mathbf{I})^{-1} \mathbf{J}^T \mathbf{y}_{fwd} \quad n = 0, 1, \dots \quad \text{Eq.(3.30)}$$

3.4.4.2 The Kaczmarz iteration

The Kaczmarz method [47] has been originally derived to handle linear systems with an excessive number of equations, similar to those emerging from the high resolution imaging modalities, such as Positron Emission Tomography (PET) and single Photon Emission Computerised Tomography (SPECT). This memory–efficient algorithm calculates the LS solution of a linear system, by solving recursively parts (rows) of the original system. In this section, a brief description of the ‘block–Kaczmarz’ method is presented, however this can be easily transformed to the standard form by taking ‘blocks’ of single rows in each iteration. The $(n+1)$ th iterative solution in the block–Kaczmarz method is

$$\begin{aligned} \boldsymbol{\sigma}_{n+1} &= \boldsymbol{\sigma}_n + \mathbf{J}_{(l:m,:)}^T \left(\mathbf{J}_{(l:m,:)} \mathbf{J}_{(l:m,:)}^T \right)^{-1} (\mathbf{y}_{fwd(l:m)} - \mathbf{J}_{(l:m,:)}^T \boldsymbol{\sigma}_n) \\ &= \boldsymbol{\sigma}_n + \left(\mathbf{J}_{(l:m,:)}^T \mathbf{J}_{(l:m,:)} \right)^{-1} \mathbf{J}_{(l:m,:)}^T (\mathbf{y}_{fwd(l:m)} - \mathbf{J}_{(l:m,:)}^T \boldsymbol{\sigma}_n) \end{aligned} \quad \text{Eq.(3.31)}$$

where

$$\begin{bmatrix} \cdot \\ \mathbf{y}_{fwd(l:m)} \\ \cdot \end{bmatrix} = \begin{bmatrix} \dots & \dots \\ \mathbf{J}_{(l:m,:)} \\ \dots & \dots \end{bmatrix} \begin{bmatrix} \cdot \\ \boldsymbol{\sigma} \\ \cdot \end{bmatrix} \quad \text{Eq.(3.32)}$$

From the previous equation, the formation of the generalised inverse $\mathbf{J}_{(l,m,:)}^\dagger$ is obvious as indeed are the possibilities of stabilising the inverse at a minimum computational cost by augmenting $\mathbf{J}_{(l,m,:)}\mathbf{J}_{(l,m,:)}^T$ by $\alpha\mathbf{I}$. Although the iteration clearly exploits overdetermined systems (more measurements than unknowns) by partitioning the Jacobian from the measurements side (rows), its computational advances in solving underdetermined systems are less obvious.

3.5 The discrete Picard criterion

The images resulting from implementing the EIT modality are mainly dominated by low-frequency spectral components that are needed to describe features of the image. However, high-frequency components are also needed to characterise the fine details of the image, however these components are generally smaller in magnitude than the low-frequency ones. This means that the expansion coefficients in a spectral basis will need to decay in magnitude as the frequency increase.

In [15], the author popularised Picard's criterion as an invaluable insight into the stability of the regularisation problem. In effect, in Picard's criterion the stability of the regularised problem is oriented around the (decay of the) Fourier coefficients $|\mathbf{p}_i^T \mathbf{y}_{fwd}|$, or more realistically $|\mathbf{p}_i^T (\mathbf{y}_{fwd} + \varepsilon)|$. These coefficients are frequently encountered in the literature as Picard's coefficients.

In the EIT image reconstruction process, one can only hope to compute an approximate reconstruction if the spectral components of \mathbf{y}_{fwd} decay faster than the generalised singular values of the Jacobian matrix. This requirement to the data, or the right-hand side \mathbf{y}_{fwd} , is known as the discrete Picard condition [15], and specifically for the truncated decompositions formulation this condition says that the right-hand side coefficients $|\mathbf{p}_i^T \mathbf{y}_{fwd}|$ must decay (on average) faster than the corresponding generalised singular values.

Due to the presence of the noise in the collected voltage measurements, one cannot expect all the coefficients $|\mathbf{p}_i^T \mathbf{y}_{fwd}|$ to decay, rather, the coefficients $|\mathbf{p}_i^T \mathbf{y}_{fwd}|$ will level off when they become dominated by the noise components. In order to guarantee a reasonably sharp image in the reconstruction process, one should include only the components that correspond to coefficients $|\mathbf{p}_i^T \mathbf{y}_{fwd}|$ that are above the noise level.

3.6 Summary

In this chapter, the EIT inverse problem was discussed in conjunction with a variety of techniques used throughout the history of EIT to deal with such a problem. The discrete framework of the linearised EIT inverse problem is presented, various direct and iterative reconstruction algorithms are applied in order to reconstruct meaningful difference images out of a very ill-conditioned system.

The regularisation concept implemented in a variety of ways was discussed; all variants are equipped with performance and regularisation selection measures to optimise the image reconstruction process. The concepts discussed in this chapter and the previous ones, will be combined to solve a variety of 2D and 3D examples, illustrating the added contribution of this thesis in reducing the size of the Jacobian matrix through lessening the number of required measurements, while keeping the resolution of the reconstructed images the same, through utilising groups of opposite electrodes, instead of pairs, in the current injection process. A further advantage of the approach is that it reduces the acquisition time needed by a EIT system to collect voltage measurements.

Chapter 4

Multi stimulation and measurement patterns for fast EIT

4.1 Introduction

In principle, EIT is simple and easy to operate and does not require experienced personnel to perform a scan. In a typical experiment, as previously mentioned, currents are applied through electrodes attached to the periphery of a body and voltage measurements are collected from some other surface electrodes. The observed data vector, i.e., the voltage measurements, is then fed to a computer to estimate the interior material distribution [47], [25], [90], [91] and [92].

Not many will argue that most of the numerical effort is typically allocated to the image reconstruction aspects of the EIT problem. Unlike standard imaging methods, as for instance X-ray CT, in EIT one could model, study and demonstrate how a ‘local’ perturbation affects not only nearby measurements but, crucially, all measurements [47]. Despite the fact that the captured measurements are sensitive to local perturbations, little is reported on how to optimise driving patterns that produce more information-rich measurements and thus reconstructions. This is a crucial matter given the fact that measurements are the only observable data in EIT.

It is worth mentioning the reports [18] and [93], where the authors derived patterns that maximise the distinguishability between two corresponding materials or simply the anticipated reconstruction contrast. Briefly, the idea is to maximise the difference between the two Neuman-to-Dirichlet (NtD) maps.

In a circular domain, the optimal stimulation pattern accounts for the eigenvalues of the corresponding NtD functional, i.e., firing on electrodes with Fourier bases. Although this provides an excellent solution from a mathematical point of view, there are some practical limitations. For instance, one needs to derive a pattern for all

electrodes and then measure the resulting voltages on the same (current carrying) electrodes. Hence, more practical patterns are sought.

In a 3D EIT setting, there is greater flexibility in stimulating the object. The authors in [94], suggested some measures to assess available stimulation protocols. Amongst many, their findings encouraged the use of non-adjacent electrode patterns. Further, since for a given set of known driving patterns, measurements are subject to a reconstruction (and thus regularisation) algorithm, results could be significantly enhanced or deteriorated. It is not clear therefore, how to best stimulate an object in order to get the most out of a measurement data set. This simply means that the way the object is stimulated could either enhance or obscure information content. A detailed discussion on the implication of information content for EIT can be found in [95].

When considering an application such as breast imaging, the reconstruction situation could be much less trivial mainly due to practical limitations. For instance, a large array of electrodes needs to be attached to the easily deformable female breast. Since both the number of electrodes and hence measurements as well as model misfits of the actual boundary surface are said to affect the quality of the reconstructed image [96], one encounters a potential bottleneck on how to proceed. The latter could be addressed by optical measurements that would result in accurate representations of the female breast surface [97]. However, there is no straightforward way as to which stimulation pattern would provide the best results for the breast imaging domain at hand and, of course, under what constraints.

To alleviate this, the authors in [19] proposed plane-wise sinusoidal voltage patterns with different phases per plane that provide improved images.

Assuming that a phase difference is the way forward for breast EIT screening, the question on whether one takes the most out of the available EIT system, as some of the measurements are (numerically) linearly dependant, is still open. In sort, this implies that one would eventually need to compensate for this loss by means of penalising higher frequency solutions, i.e., regularisation, to avoid numerical

instability. Needless to say that determining the optimal number of electrodes is also an additional open issue.

In the same spirit, the authors in [20] identified the stimulation shortcomings and proposed a much promising strategy which was numerically demonstrated in a 2D setting with 32 electrodes. Unlike most conventional methods reported in literature, the novelty lies in engaging 4 electrodes to drive a current pattern. Next, a measure was derived by means of GSVD to quantify the collected measurements against prior information as well as measurement noise, in order to filter out problematic singular values.

The work introduced in this Chapter is an extension to that in [20], as, in the author's view, this appears to be the only practical measure that factor in prior information when devising a stimulation strategy. Further, the stimulation protocol is extended to 3D, where a greater number of electrodes and patterns is often available. To the best of the author's knowledge, this methodology has never been tested on a 3D domain before. On the other hand, this contribution differs from the one in [20] as it accounts for groups of variable electrode numbers to apply the desired stimulation protocol. This implies a variable reduction in the number of collected measurements (and thus data acquisition times) without compromising the quality of the reconstructed images. Finally, there is no need to measure on current carrying electrodes [18], [19] and [93] - [97].

4.2 Numerical stability of simulation studies

Unlike the conventional injection protocols, the proposed multi-injection protocol aims at reducing computational complexity as well as acquisition time, whilst maintaining reconstruction quality. This is achieved by injecting electrical currents from opposite groups of electrodes rather than through single electrodes. Each current pattern is formed by shifting those groups by a factor which is equal to half the number of electrodes forming each group, this shift is often referred to as 'scrolling' [20].

4.2.1 Conservation of Energy

In order to achieve comparable results with those obtained from conventional injection protocols, and avoid injecting excessive amounts of electrical currents (especially when considering medical applications), one opts to divide the magnitude of the injected electrical current (in the conventional stimulation protocol) by the number of electrodes forming a single group (in the multi-injection protocol), as shown in Figure 4.1.

In a conventional stimulation scenario, as shown in the top part of Figure 4.1, the injected electrical current through a single electrode has an amplitude of $+x$ Amps (top left), and $-x$ Amps exit the medium through the opposite one (top right). Then, an electrical current of $+x/n_{elec}$, where n_{elec} is the total number of electrodes per group, in this example $n_{elec}=4$, will be the value of the current amplitude injected through each electrode within the group (bottom left of Figure 4.1), and $-x/n_{elec}$ for the one exiting the medium through each electrode within the opposite group (bottom right of Fig 4.1).

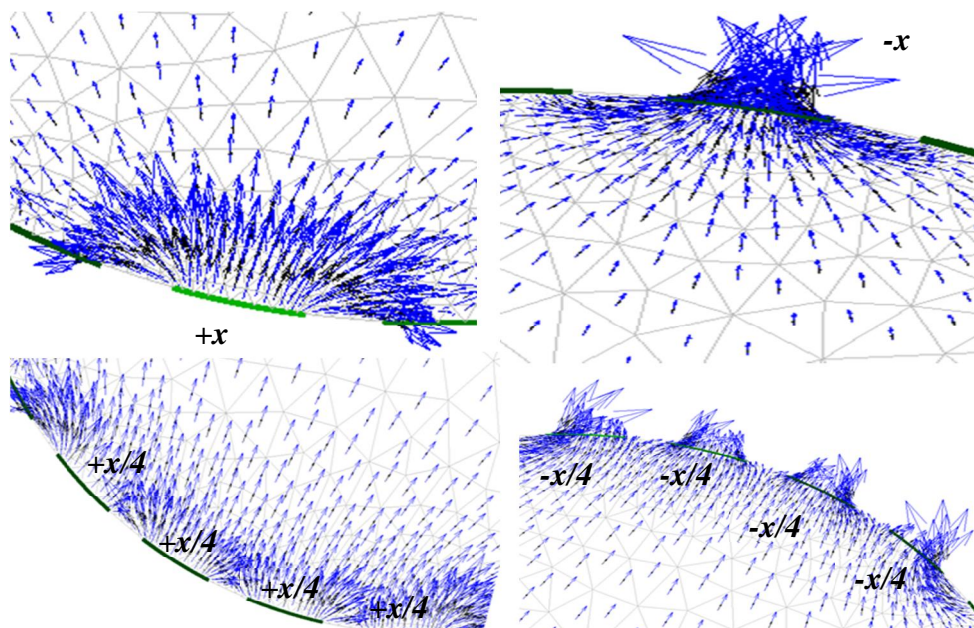


Figure 4.1 Principle of energy conservation. The two top images show the conventional opposite 2-electrode pair injection mechanism, whilst two bottom images show the multi-injection protocol with 4-electrodes per group.

4.2.2 Boundary conformity

Following the same rationale, it should be emphasized that the *total* length (in the 2D case) and area (in the 3D case) of the medium's boundary occupied by the electrodes should remain the same, and independent of the number of electrodes to be used. The motivation for this work is to design efficient stimulation protocols while maintaining the length/area occupied by the electrodes, and thus the area of current injection.

In other words, if only 2-electrode groups are desired to be installed at the medium's periphery covering a total of A length/area units, then each of them will cover $A/2$ units. Along the same lines, using a 4-electrodes scheme should cover the same total of A units, with each electrode covering $A/4$ units.

4.3 Overview of simulations studies

In order to provide a clear comparison between the conventional and the proposed stimulation protocols, numerical simulations will be presented, focusing on the use of a specific metric. This metric is referred to as the gain of the stimulation protocol, which is defined as the ratio of the generalised singular values that meet Picard's criterion over the total number of available generalised singular values [20]. This can be interpreted as a measure of the practical efficiency of the system, i.e., the percentage of reliable measurements spectrum over the spectrum of all available measurements. It will be shown later on that the use of a multi-injection protocol eventually decreases the percentage of the unreliable (filtered out) measurements spectrum over the full measurements spectrum solely by making adjustments on the stimulation pattern. This is equivalent to collecting less measurements m .

On the other hand, in order to demonstrate that essentially no compromise in the quality of the reconstructed images is reported, Section (4.7) shows some indicative yet representative reconstruction results. The question of investigating regularisation parameter selection strategies to decide on an optimum regularisation parameter

value α is not of prime interest as far as this study concerned. However, to emphasize on the impact of an appropriate selection of a stimulation strategy, priors, and regularisation parameter in order to obtain optimum reconstructions, the previously discussed L-curve criterion [98] is deployed to support the choice of regularisation parameter used in the simulations herein. For clarity, a linearised problem is opted for, the solution of which is given by Eq. (3.21). Unless otherwise specified, the identity matrix is employed as the regularisation prior, $R^T R = I$. At this stage, the selection of the regularisation matrix is of secondary importance when compared to the selection of the stimulation pattern.

4.4 Computational efficiency

One of the main advantages of the multi-injection protocol is the substantial reduction in acquisition time. That is, collecting a minimal number of boundary measurements, whilst maintaining performance. Throughout this section, the proposed multi-injection protocol is compared against the conventional opposite 2-electrode pair stimulation protocol. However, although one could consider adjacent stimulations, according to [94], little information is acquired with adjacent stimulation patterns, hence a standard opposite 2-electrode pair stimulation pattern is employed in this research.

When $L = 8$ electrodes, are available and the current is applied to a 2-electrode pair of opposite electrodes, i.e., $I_1 = [1, 0, 0, 0, -1, 0, 0, 0]^T$, one could collect measurements between electrodes $\{2, 3\}$, $\{3, 4\}$, $\{6, 7\}$, and $\{7, 8\}$ i.e., $L - 4$ measurements for this particular current pattern. By shifting the current pattern by one electrode, one arrives at $I_2 = [0, 1, 0, 0, 0, -1, 0, 0]^T$. Repeating for L -electrodes, eventually one could potentially collect $m = L \times (L - 4) = 32$ measurements, half of which are linearly independent. Thus, one could practically collect a total of $m = \frac{1}{2} L \times (L - 4) = 16$ independent measurements which will then form the measurements vector \mathbf{y} .

On the other hand, when employing the multi-injection protocol by assigning two opposite groups of 2-electrodes per group ($n_{elec} = 2$), i.e., having the first stimulation pattern of $I_1 = [1, 1, 0, 0, -1, -1, 0, 0]^T$, where one could collect measurements between electrodes $\{3, 4\}$ and $\{7, 8\}$ i.e., $(L-2) \times n_{elec} - 2$ measurements for this particular current pattern, and by shifting the current pattern by the scrolling value of 2 (i.e., half the number of electrodes in the group or $n_{elec}/2$), one arrives at $I_2 = [0, 1, 1, 0, 0, -1, -1, 0]^T$, and following the same rationale for L electrodes, a total of $m = \frac{1}{2} \frac{L(L-2 \times n_{elec} - 2)}{(n_{elec}/2)} = 8$ independent boundary measurements can be collected for vector \mathbf{y} .

Figure 4.2 shows images of the potential distributions, which resulted at the first stimulation pattern (upper images) inside a 2D medium with 24-electrodes, and plots of the calculated (through the forward problem) boundary voltages when subjected to a conventional 2-electrode pair opposite injection strategy (left-hand side of the image) and also for the multi-injection protocol. In the conventional protocol, only two opposite electrodes are involved in the current firing process, resulting in 20 adjacent measurements being collected at each stimulation pattern (i.e., a total of 480 measurements). However, in the multi-injection protocol, where 2 groups of 4-electrodes each are involved in the firing process, only 14 measurements are being taken at each stimulation pattern, totalling 84 measurements. This number is significantly less than the 480 measurements that would have been otherwise needed.

Hence, the apparent advantage of the proposed stimulation pattern is that although $L = 24$ electrodes were originally considered, the EIT system is essentially clocked with just 84 measurements. In other words, 84 measurements translate to just 17.5% of the overall time required to collect data with the conventional 2-electrode pair opposite protocols.

Table 4.1 shows values of quantitative time-saving ratios obtained through running the EIT system when utilising the multiple-injection scheme. The system is clocked

CHAPTER 4. MULTI STIMULATION AND MEASUREMENT PROTOCOL FOR FAST EIT

to fire 6–stimulation patterns only. The percentage reduction is calculated as the ratio between the number of measurements collected when utilising the multi–injection protocol over the number of measurements collected when utilising the conventional 2–electrode pair opposite protocol.

# of collected measurements \ # of electrodes	Conventional 2–electrode pair opposite protocol	Multi–injection protocol (6–stimulation patterns)	Percentage reduction (%)
12	96	36	62.5
24	480	84	82.5
36	1152	132	88.54
48	2112	180	91.48

Table 4.1 Percentage reduction time when using the multi–injection protocol

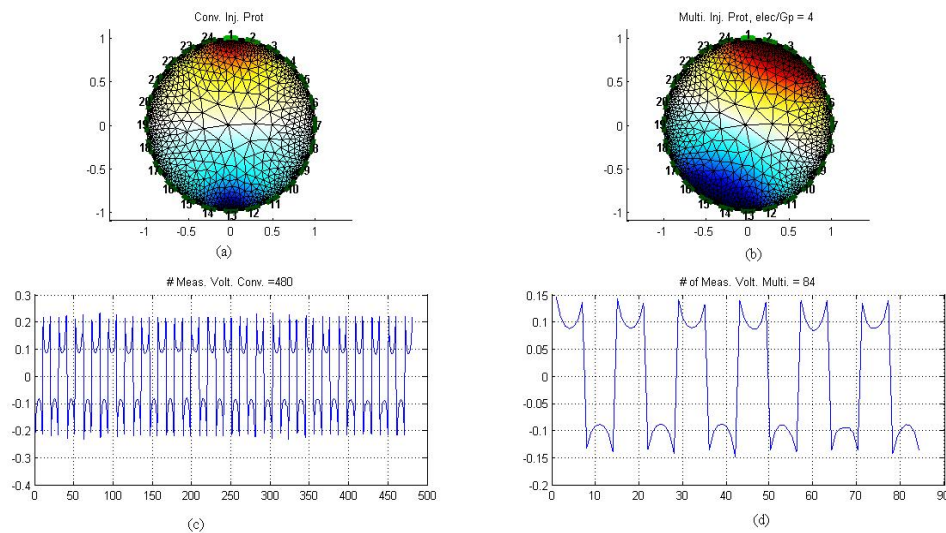


Figure 4.2 The potential distribution and calculated boundary voltages. (a) The field from the first current pattern for the conventional opposite 2–electrode pair stimulation protocol, (b) the field from the first current pattern for the multi–injection protocol with 4 electrodes/group, (c) the measured boundary voltages for the conventional opposite 2–electrode pair stimulation protocol, and (d) the measured boundary voltages for the multi–injection protocol.

Another added advantage of the multi–injection protocol is that the current density (left–hand side image) inside the medium, is substantially higher than that for the conventional opposite 2–electrodes one (right–hand side image), as shown in a

b

Figure 4.3b. This directly results in higher detection chances of any perturbation should it be missed due to its size or location by the conventional injection protocol. Hence, the perturbation’s traceability is higher given the reduced number of collected voltage measurements.

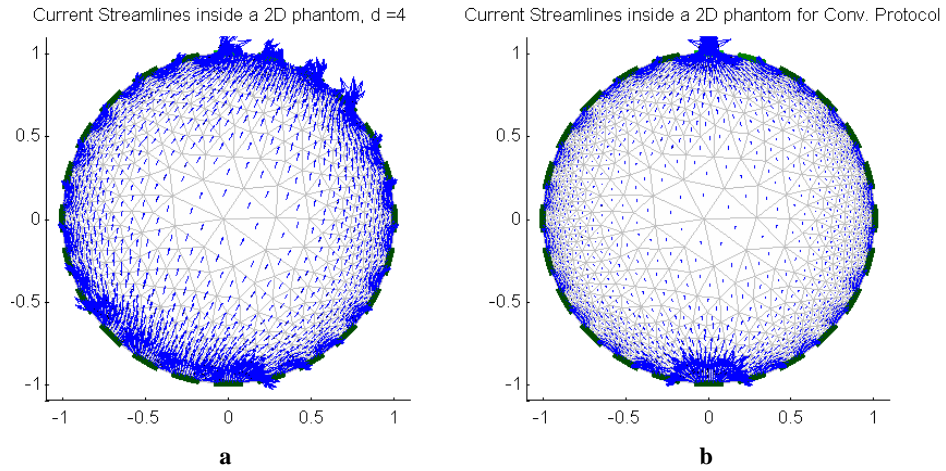


Figure 4.3 The current streamlines for (a) the conventional opposite 2–electrode pair and (b) multi–injection stimulation protocols.

4.5 A comparison between the conventional opposite 2–electrode pair stimulation and multi– injection protocols based on Picard’s stability and GSVD techniques

In this section, the gains resulting from the implementation of the conventional opposite 2–electrode pair stimulation and multi–injection protocols are calculated for 2D and 3D scenarios. The 2D model used in this context is a circular domain of a uniform background distribution, whilst the 3D model is a cylinder having 3 rings and 4 rings of electrodes, respectively. For each case, a single inhomogeneity whose conductivity differs from its surrounding, is placed at a given location inside the medium. The respective gains are then calculated for each stimulation protocol for various numbers of electrodes ($L=12, 24, 36,$ and 48 electrodes). The motivation for choosing L (number of electrodes) and the directly related m number of measurements is essentially to highlight the fact that, the greater the number of electrodes, the more the measurements to be collected.

Throughout the experiments in this section, without loss of generality, 6–stimulation patterns are employed. Therefore, opposite groups will have different sizes depending on the total number of electrodes used, i.e., in order to achieve 6

stimulation patterns, the respective electrode groups will have a number of electrodes $n_{elec} = 6, 12, 18,$ and 24 electrodes/group for the 12, 24, 36, and 48 electrodes configuration schemes, respectively. Finally, in order to avoid the inverse crime, and to add realistic operating conditions, without loss of generality, in all simulation results, 25dB additive Gaussian noise ε is added to the simulated measurements.

4.5.1 Conventional opposite 2–electrode pair stimulation protocol – 2D and 3D scenarios

Figures. 4.4–4.9 show plots of the Picard coefficients along with the generalised singular values γ_i when plotted for different 2D and 3D media. Recalling the discrete Picard criterion in Section 3.4, one requires a faster decay of Picard’s coefficients $|\mathbf{p}_i^T(\mathbf{y} + \varepsilon)|$ than the decay of the generalised singular values γ_i . In [20], the ratio of the generalised singular values that meet Picard’s criterion over the total number of available generalised singular values is termed as *gain* of the selected stimulation pattern.

Figure 4.4. illustrates that, for the 2D scenario, when running the system using the conventional opposite 2–electrode pair stimulation strategy, the quality of the gathered measurements is no better when additional electrodes are added. As the gains tabulated in Table 4.2 show, the increase in the number of electrodes has led to a relative reduction in the respective gain, **Gain 1**, as has been referred to in this context. In the same Table, the ratio of the number of electrodes over the number of measurements is also tabulated to demonstrate how disproportional the increase of electrodes with respect to measurements could be.

Clearly, as it can be depicted from Figure 4.4(a), the majority of the singular values (labelled in blue in the Figure) are below Picard’s threshold (labelled in green in the Figure). This becomes profound as the number of electrodes increases in the same Figure for the cases of (b) 24, (c) 36 and (d) 48 electrodes, where notably only a few singular values γ_i survive filtration.

The same concept applies for the 3D scenario reported in Figure 4.6 when deploying 3–rings of electrodes. The actual gains recorded for each case are tabulated in Table

4.3, and termed as, **Gain 2**. In the same spirit, one can see that the quality of the obtained measurements does not improve when additional electrode rings are deployed. In the new configuration, the number of electrodes remains fixed, however, an additional ring of electrodes is allowed. As such, a different electrode distribution is enabled as illustrated in Figure 4.8 and the corresponding gains for the 4 rings systems are now tabulated in Table 4.4 and termed as Gain 3. By coupling each of the sub-Figures in Figure 4.8 by their corresponding entries in Table 4.4, it is evident that assuming a fixed number of electrodes for each case, essentially the additional ring allowance offers very little improvements, if any at all.

Taking into account that the meshing algorithm [99], produces slightly more mesh elements to accommodate the need for the additional ring, the gains obtained from **Gain 2** are in the same range as in **Gain 3**. It is not hard to see from Table 4.3 and Table 4.4 that an additional ring of electrodes results in the same number of measurements and does not yield an overall system improvement in the sense discussed herein.

In fact, one should focus on the fact that, for the given opposite 2-electrodes pair stimulation pattern, as the total number of electrodes increase, both **Gain 2** and **Gain 3** plummet, as more regularisation would indeed be required for stability. In this regard, less singular values would escape filtration. This should be approached as a numerical acknowledgement of the fact that increasing the number of electrodes does not (necessarily) increase the potential information content. Note that this acknowledgement triggers again the easier question on whether one takes the most out of an EIT system, which essentially paves the way for non-conventional stimulation/collection protocols.

4.5.2 Proposed Multi-injection stimulation protocol – 2D and 3D scenarios

Given the GSVD discussion of the previous sections, it remains to demonstrate that the resulting gain for the multiple-electrodes pair is better than the conventional one. Intuitively, since more electrodes are involved in the firing process whilst occupying

a greater boundary surface, it is sensible to anticipate some gain improvement over the conventional 2–electrodes pair stimulation scheme. In other words, one would expect to observe a faster decay in Picard’s coefficients than the generalised singular values of the matrix pair (\mathbf{J}, \mathbf{I}) for this particular case.

In the 2D scenario, as Figure 4.5 shows, the percentage of the number of generalised singular values below the Picard’s coefficients are much less than for the conventional 2–electrode pair stimulation protocol. This actually means that the new generalised singular values, calculated for a smaller Jacobian, contain much more information of the problem at hand, than those calculated from the Jacobian resulting from the conventional protocol. In other words, according to Table 4.2 and Table 4.5, it is quite clear that, the gains resulting from deploying the multi–injection protocol are almost 60% higher than for the conventional one, i.e., containing 60% more information.

On the other side, for the 3D scenario, Figure 4.7 reveals the generalised singular spectrum against the Picard’s coefficients for the multi–injection protocol when applied for the 3D model with 3–rings of electrodes. The superiority of this scheme for this case materialises from the readings of Table 4.6, in particular when a large number of electrodes is considered (**Gain 5**). The naïve interpretation of Table 4.6 is that, for the same domain, with the same forward problem parameters and the same regularisation matrix, one could essentially derive an improved system. As in the derived EIT system m is significantly smaller than the original one, so is the linearised problem. Hence, by definition, this is a lower dimension problem and thus intuitively it should be a much faster problem to solve.

The advantages of the proposed scheme become more apparent as more electrodes are engaged in the simulation process. For clarity, the number of electrode rings is increased to 4 and the corresponding singular spectrum for the 4 rings of electrodes case is illustrated in Figure 4.9. As anticipated, a significant gain improvement when compared with Gain 3 is recorded and the results are tabulated in Table 4.7 (**Gain 6**).

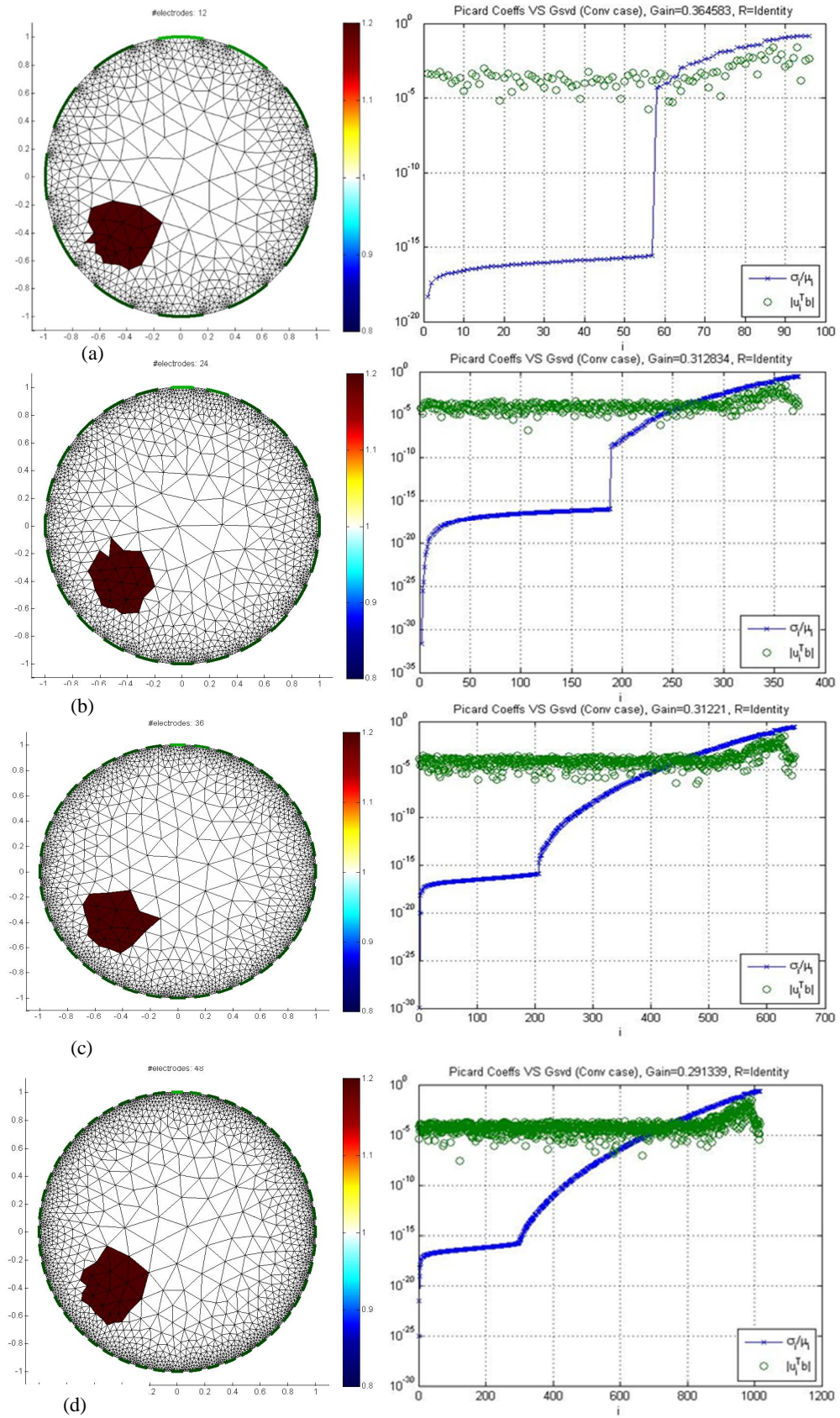


Figure 4.4 Conventional opposite 2-electrode pair stimulation protocol gains for a 2D circular medium with a single inhomogeneity located at $(x - 0.45)^2 + (y - 0.4)^2 - 0.2^2 < 0$ and $\delta\sigma = +20\%$ of the background value.

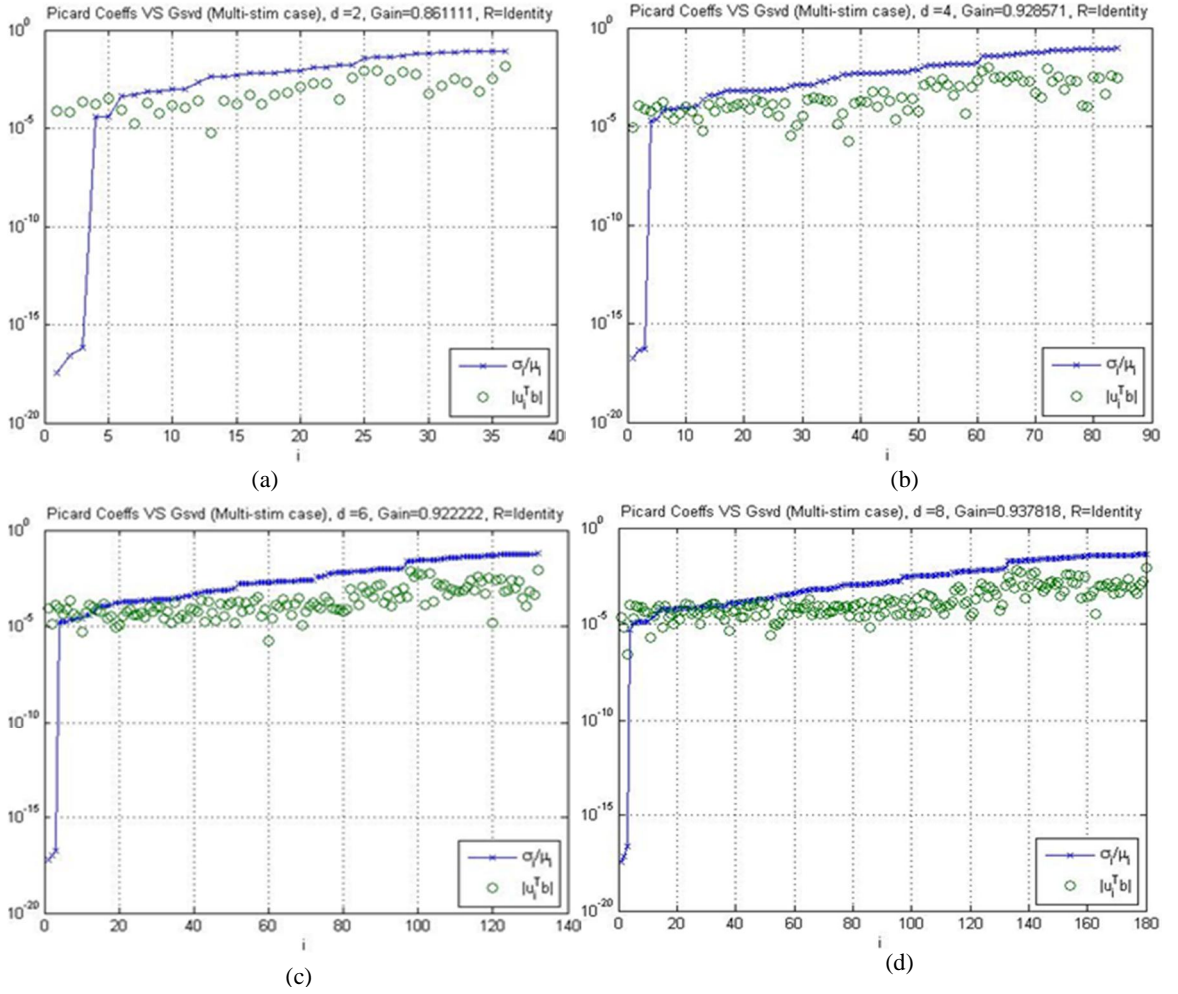


Figure 4.5 Proposed multi-injection stimulation protocol gains, for a 2D circular test phantom where a single inhomogeneity is located at $(x - 0.45)^2 + (y - 0.4)^2 - 0.2^2 < 0$ of $\delta\sigma = +20\%$ of the background value.

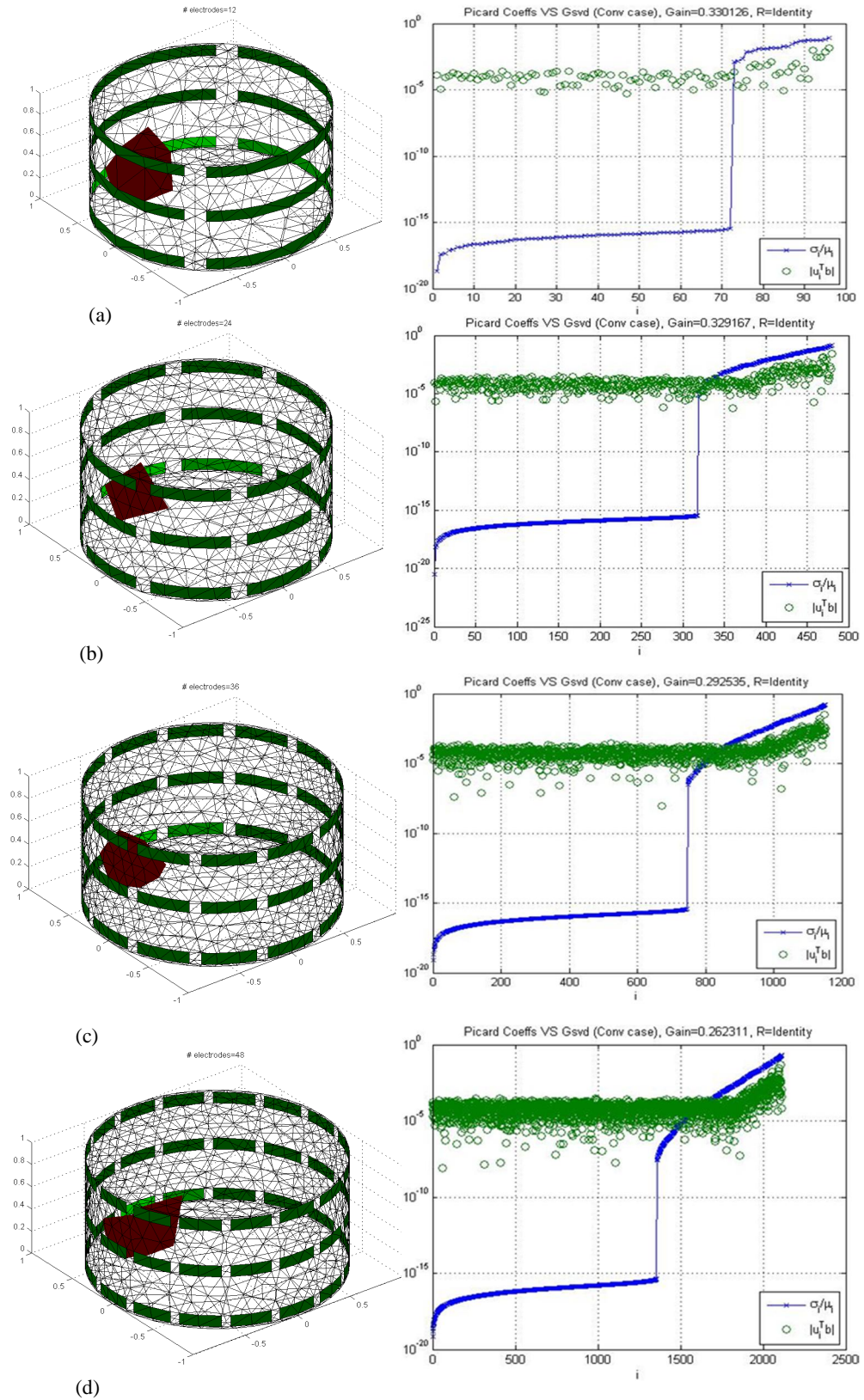


Figure 4.6 Conventional opposite 2-electrode pair stimulation protocol gains for a 3D cylindrical medium, where a single inhomogeneity is located at $(x+0.5)^2 + (y-0.3)^2 + (z-0.4)^2 - 0.1^2 < 0$ of $\delta\sigma = +20\%$ of the background value. A maximum of 3 rings of electrodes are allowed.

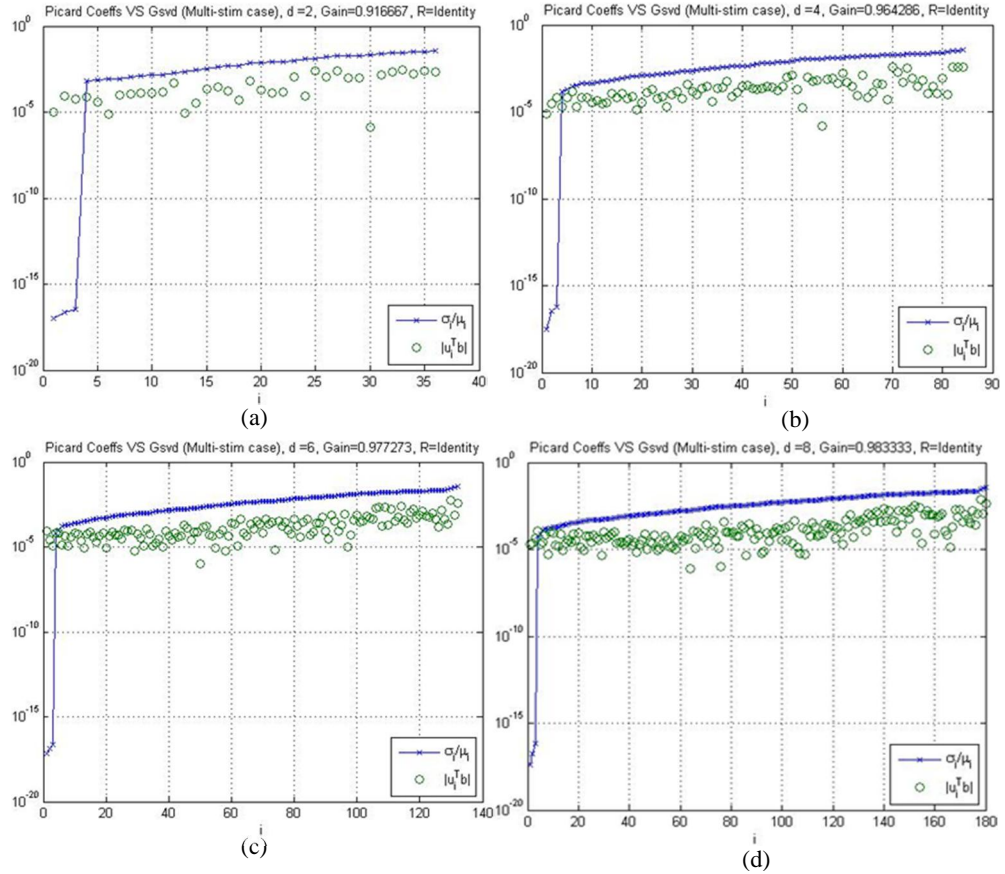


Figure 4.7 Multi-Injection stimulation protocol gains for a 3D cylindrical medium, where a single inhomogeneity is located at $(x+0.5)^2 + (y-0.3)^2 + (z-0.4)^2 - 0.1^2 < 0$ of $\delta\sigma = +20\%$ of the background value. A maximum of 3 rings of electrodes are allowed.

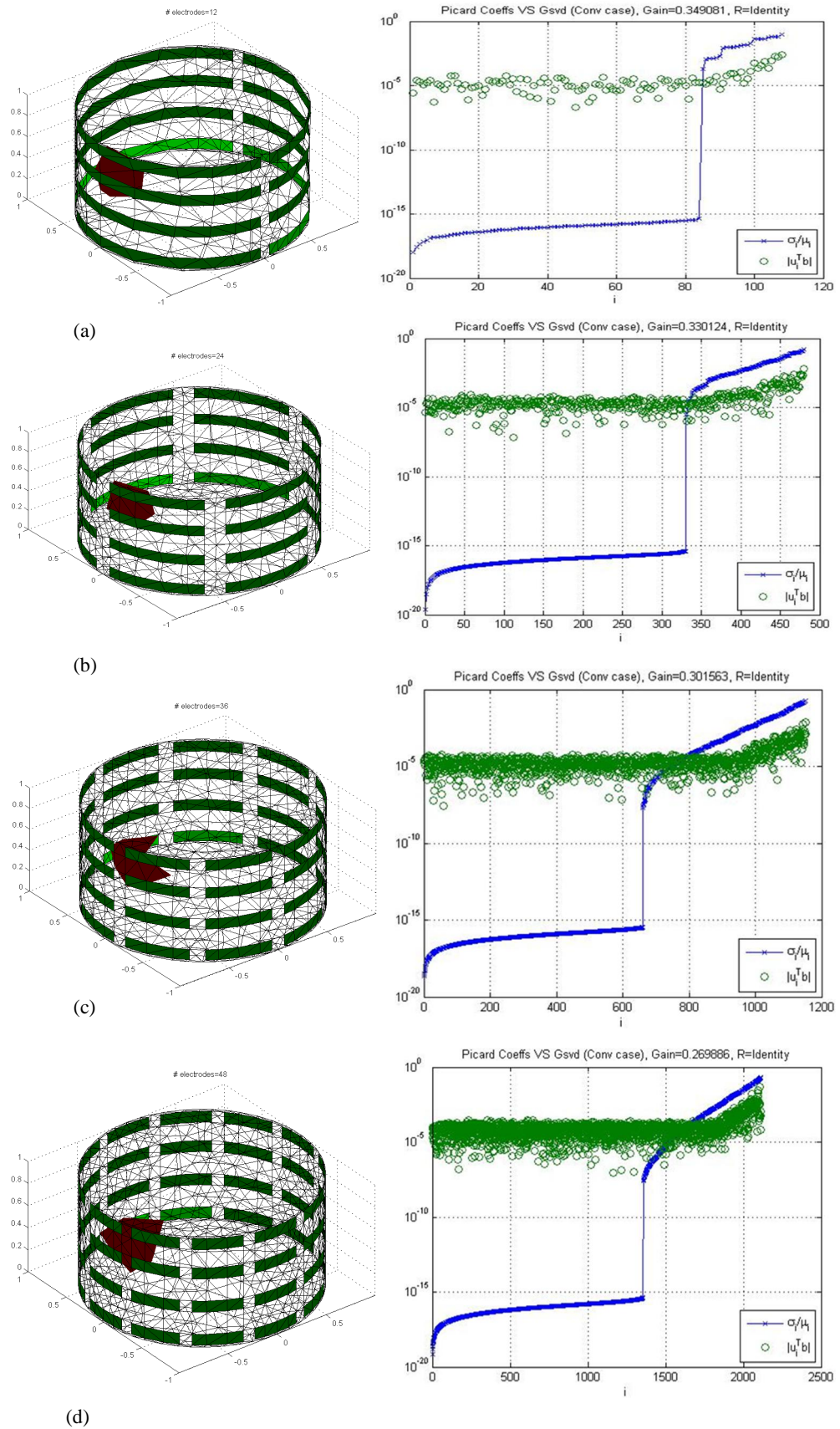


Figure 4.8 Conventional opposite 2-electrode pair stimulation protocol gains for a 3D cylindrical medium, where a single inhomogeneity is located at $(x+0.5)^2 + (y-0.3)^2 + (z-0.4)^2 - 0.1^2 < 0$ of $\delta\sigma = +20\%$ of the background value. A maximum of 4 rings of electrodes are allowed.

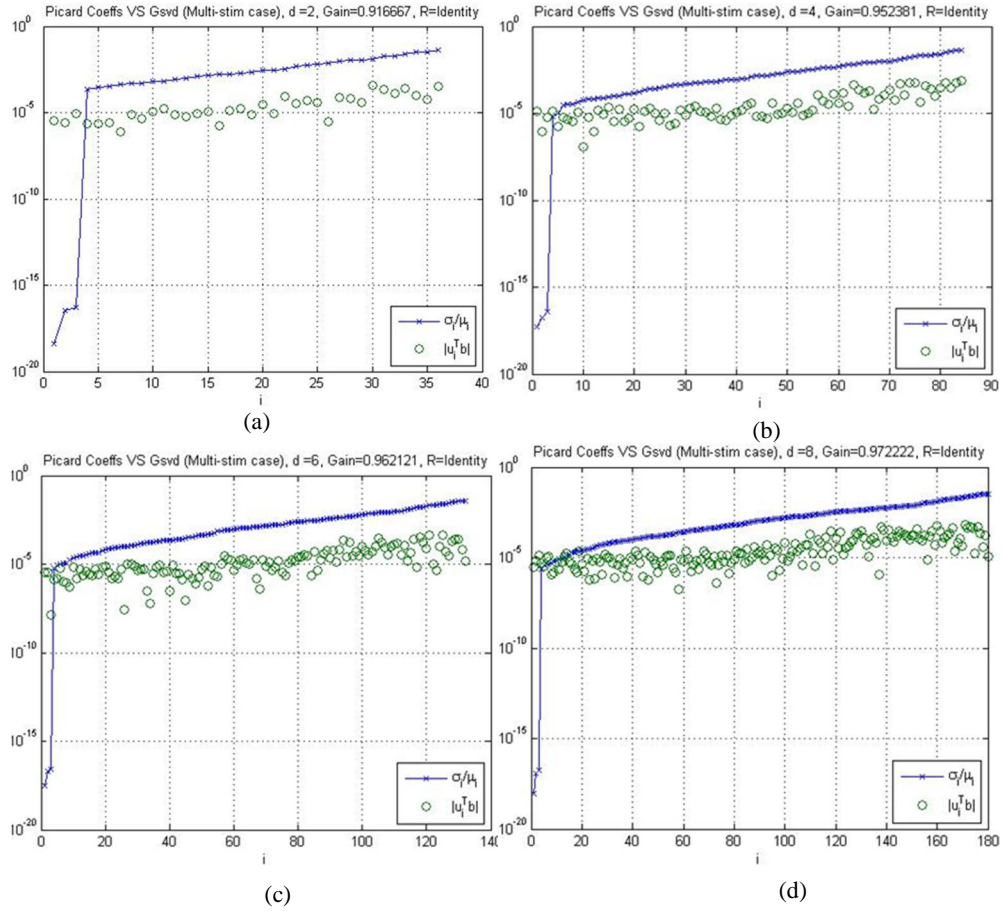


Figure 4.9 Proposed multi-injection stimulation protocol gains, for a 3D cylindrical medium, where a single inhomogeneity is located at $(x+0.5)^2 + (y-0.3)^2 + (z-0.4)^2 - 0.1^2 < 0$ of $\delta\sigma = +20\%$ of the background value. A maximum of 4 rings of electrodes are allowed.

CHAPTER 4. MULTI STIMULATION AND MEASUREMENT PROTOCOL FOR FAST EIT

Electrode L	Measurements m	L/m	Gain 1
12	96	0.12500	0.364583
24	480	0.05000	0.312834
36	1152	0.03125	0.312210
48	2112	0.02273	0.291339

Table 4.2 Conventional opposite 2–electrode pair stimulation protocol gains for a 2D circular test phantom.

Electrode L	Measurements m	L/m	Gain 2
12	96	0.12500	0.330126
24	480	0.05000	0.329167
36	1152	0.03125	0.292535
48	2112	0.02273	0.262311

Table 4.3 Conventional opposite 2–electrode pair stimulation protocol gains, when a maximum of 3–rings of electrodes is allowed.

Electrodes L	Measurements m	L/m	Gain 3
12	96	0.12500	0.349081
24	480	0.05000	0.330124
36	1152	0.03125	0.301563
48	2112	0.02273	0.269886

Table 4.4 Conventional opposite 2–electrode pair stimulation protocol gains, when a maximum of 4 rings of electrodes is allowed.

Electrodes L	Measurements m	L/m	Gain 4
12	36	0.12500	0.861111
24	84	0.05000	0.928571
36	132	0.03125	0.922222
48	180	0.02273	0.937818

Table 4.5 Multi–injection stimulation protocol gains for a 2D circular test phantom.

Electrodes L	Measurements m	L/m	Gain 5
12	36	0.3333	0.916667
24	84	0.2857	0.964286
36	132	0.2727	0.977273
48	180	0.2667	0.983333

Table 4.6 Multi–injection stimulation protocol gains, when a maximum of 3 rings of electrodes is allowed.

Electrodes L	Measurements m	L/m	Gain 6
12	36	0.3333	0.916667
24	84	0.2857	0.952381
36	132	0.2727	0.962121
48	180	0.2667	0.972222

Table 4.7 Multi–injection stimulation protocol gains, when a maximum of 4 rings of electrodes is allowed.

4.6 Multi–injection versus prior information

It is evident from the previous sections that an increased number of electrodes is not necessarily a computational bottleneck. Having demonstrated the effectiveness of the proposed scheme, the next sensible task is to report on the performance of a non–identity prior, and opt to nominate optimum operating conditions, in terms of stimulation patterns and the prior used in order to achieve a higher gain, which in turn indicates, making better use of the available ‘useful’ singular values. For this purpose we employ the so called Newton’s One–Step Error Reconstructor prior [58] or the NOSER prior, for short, which is essentially the diagonal of $\mathbf{J}^T \mathbf{J}$.

The number of electrodes used to illustrate this concept is fixed. Three rings of electrodes as shown in Figure 4.6 (c) each containing 12 electrodes, i.e., totalling 36 electrodes. The performance of the original opposite 2–electrode pair stimulation pattern is illustrated in Figure 4.10 (a) and the corresponding gains are tabulated in Table 4.8. As anticipated, an increase in the gain measure is reported when, as expected, the more efficient NOSER prior used (**Gain 8**) for the same case. Next, the proposed configuration when 2 electrodes per group are used, is tested against the conventional one. This action essentially supports the theme of this research which is replacing the single electrode groups for more electrodes per group.

In Table 4.8 one may appreciate the performance of the suggested scheme for the prior considered herein. Clearly, increasing the number of electrodes per firing–group results in a more efficient system, up to a certain point, where any further increase in the number of electrodes will not affect the gain (i.e., when the gain reaches 1). However, the performance is clearly enhanced by the selection of the NOSER prior.

In summary, by suitably ‘clocking’ an EIT with an appropriate stimulation pattern as well as an appropriate prior, the performance of the same system could be drastically improved from a gain of 0.292535 (**Gain 7**) to 0.980364 (**Gain 8**), not to mention the benefits in data acquisition volumes and computational times. If more electrodes are

considered, say $L=48$ rather than 2112 measurements, only 180 measurements need to be collected. This accounts for approximately 8.52% of the original measurement vector or a saving in terms of data acquisition volume of approximately 91.48 %. Thus, for this example, one could not only derive a faster system but could also get away with a fraction of the conventional measurements.

CHAPTER 4. MULTI STIMULATION AND MEASUREMENT PROTOCOL FOR FAST EIT

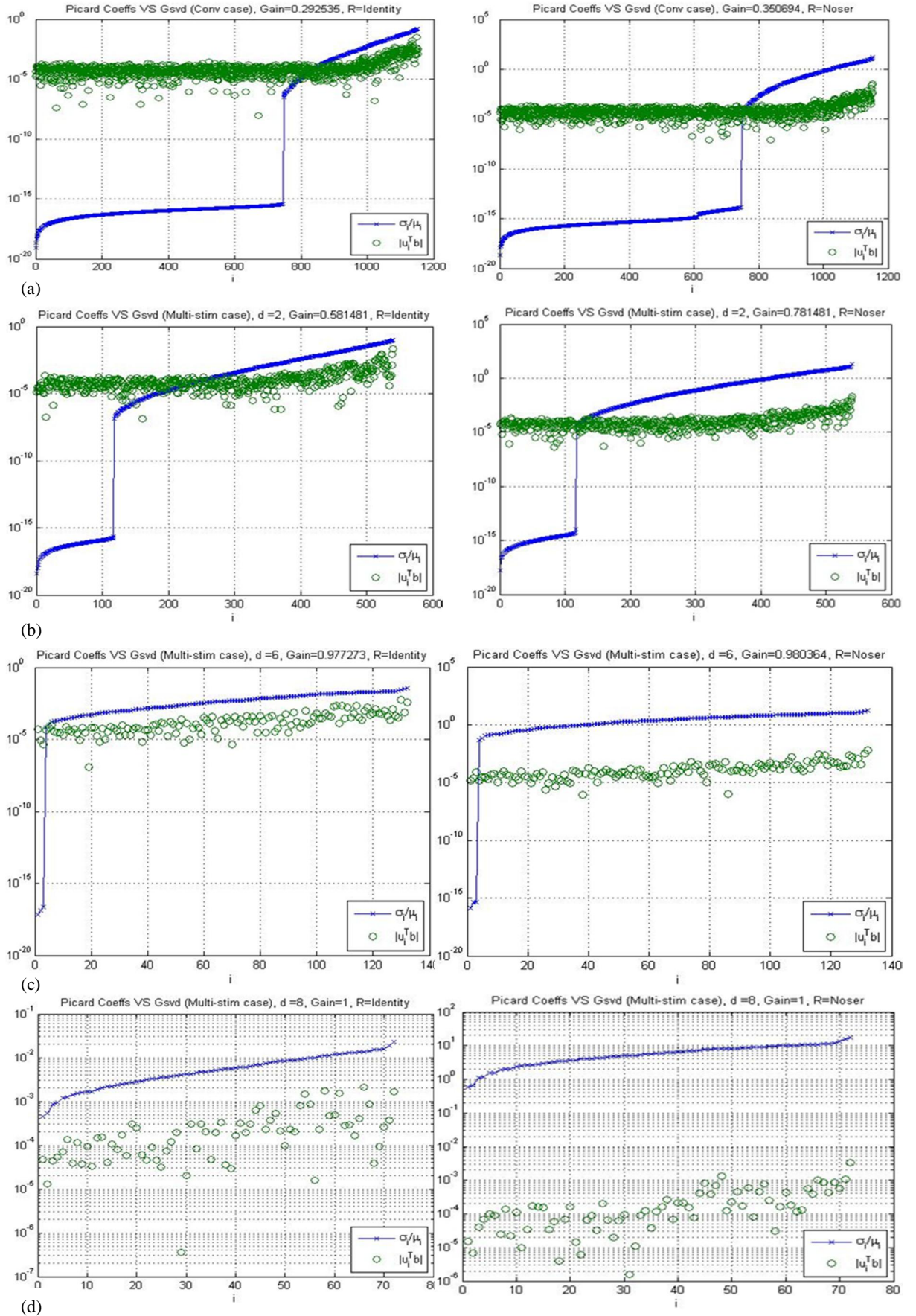


Figure 4.10 Conventional versus proposed opposite protocol for various numbers n_{elec} of electrodes per group per stimulation group. (a) $n_{elec} = 1$ (Conventional), (b) $n_{elec} = 2$, (c) $n_{elec} = 6$, (d) $n_{elec} = 8$ electrodes per group. The results shown in the left column assume a simple identity prior whilst in the right column, the NOSER prior is used.

electrodes/group	Electrodes L	Measurements m	L/m	Gain 7	Gain 8
1 (conventional)	36	1152	0.03125	0.292535	0.350694
2	36	540	0.06671	0.581481	0.781481
6	36	132	0.27274	0.977273	0.980364
8	36	72	0.50000	1.00000	1.00000

Table 4.8 Comparison between conventional and proposed (2, 6, and 8 electrodes per group) opposite protocol gains for the 3D phantom with 3 rings of 12 electrodes. Priors considered herein are the Identity (**Gain 7**) and the NOSER (**Gain 8**) one.

4.7 Image reconstruction

In order to demonstrate that essentially no compromise in the quality of the reconstructed images is reported, some indicative yet representative reconstruction results, are provided. The question of the optimum regularisation value is essentially an active research area where various methods could be used [15]. This is beyond the scope of this study as the answer lies with the problem at hand and the specifications to be met. Therefore, images are reconstructed for various equidistant logarithmic values for α , ranging from 10^{-1} to 10^{-8} , i.e., $\alpha = \{1.00000e-001, 1.33352e-002, 1.77828e-003, 2.37137e-004, 3.16228e-005, 4.21697e-006, 4.62341e-007, 7.49894e-008, 1.00000e-008\}$. In addition, the resulting reconstructed image for the specific choice of the regularisation parameter produced by employing the L-curve criterion is presented within.

For clarity, linear reconstruction for the various configurations reflecting the number of electrodes per firing-group, is presented, i.e., the conventional stimulation protocol i.e., 1 electrode per group in Figure 4.11, the proposed one for 2 electrodes per group in Figure 4.12 for 6 electrodes per group in Figure 4.13, and for 8 electrodes per group in Figure 4.14. In each Figure, one depicts from the first column 2D coronal slices extracted from the original 3D simulated perturbation. Essentially, we extract 2D reconstruction at levels $\mathbf{h} = [0.3334 \ 0.5001 \ 0.6668 \ 0.8335]^T$, hence 4-images per column. The columns next to the original 3D perturbation, i.e., columns 2–10 in each Figure, are reconstructions for the various values of α , and the last column represents the slices resulted from slicing the reconstructed image when the L-curve is deployed to choose the value of the regularisation parameter.

To avoid biased reconstructions and essentially an inverse crime, measurements and reconstructions were computed on different meshes. In effect, measurements were

collected from the fine mesh for a 20% perturbation. As mentioned before, 25dB noise was added to the measurements. All reconstructions were performed on a coarser mesh. For all simulations the EIDORS toolbox was employed [100].

Another useful observation that can be seen from the previous figures is that, the more electrodes per group employed, the wider the range that one can pick up the regularisation parameter from, to result in more meaningful images. That is due to the better utilisation of the ‘useful’ singular values resulting from the appropriate choice of the current stimulation strategy. Hence, this coupled with utilising the L–curve criterion, as shown in the far right–hand side column, assuming it to be the optimal regularisation selection criteria, will result in even clearer images. Appendix (C) contains further simulations for 2D and 3D image reconstructions when deploying the conventional opposite 2–electrode pair and multi–stimulation protocols.

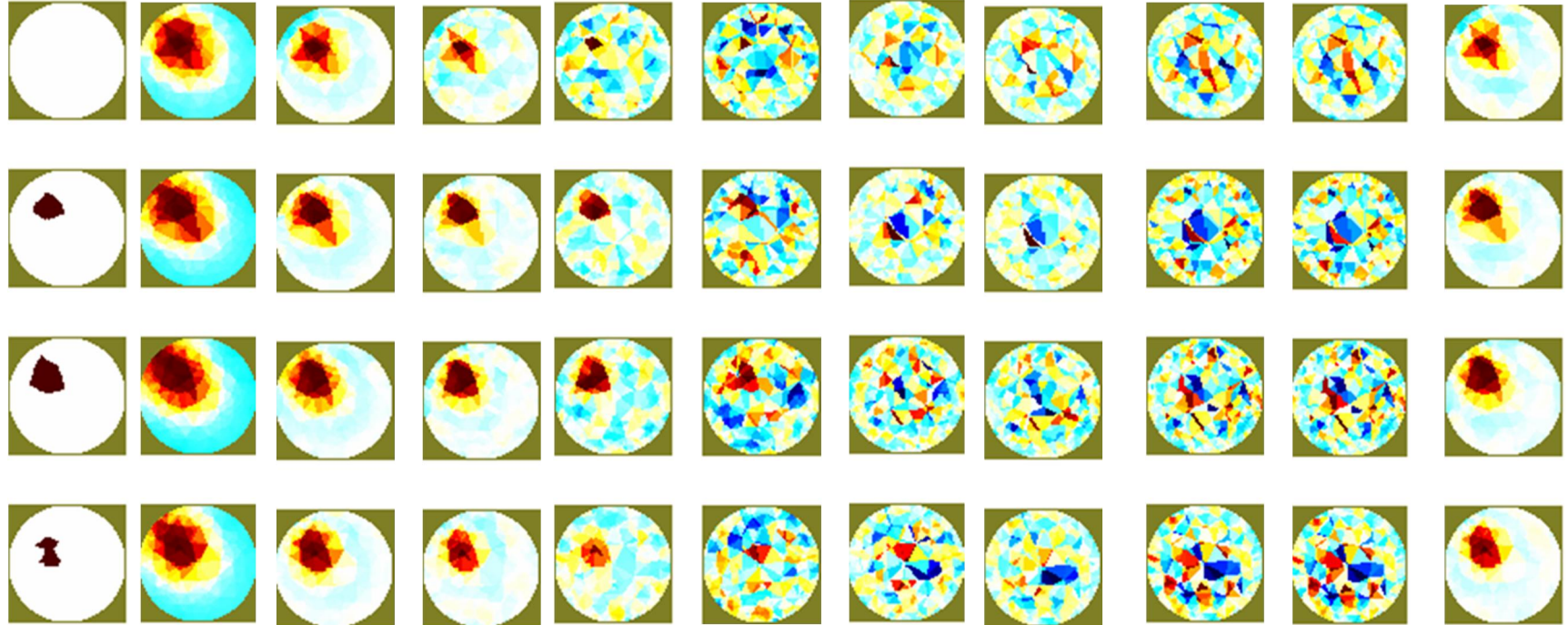


Figure 4.11 Conventional opposite protocol. The first column is the original 3D perturbation presented as 2D coronal slices of the cylindrical phantom at levels \mathbf{h} . The columns (2–10) are the reconstructions for various values of the regularisation parameter $\lambda = \{1.00000\text{e-}001, 1.33352\text{e-}002, 1.77828\text{e-}003, 2.37137\text{e-}004, 3.16228\text{e-}005, 4.21697\text{e-}006, 4.62341\text{e-}007, 7.49894\text{e-}008, 1.00000\text{e-}008\}$, and the last column represents the reconstructed image resulted from the regularisation parameter produced though the L-curve criterion.

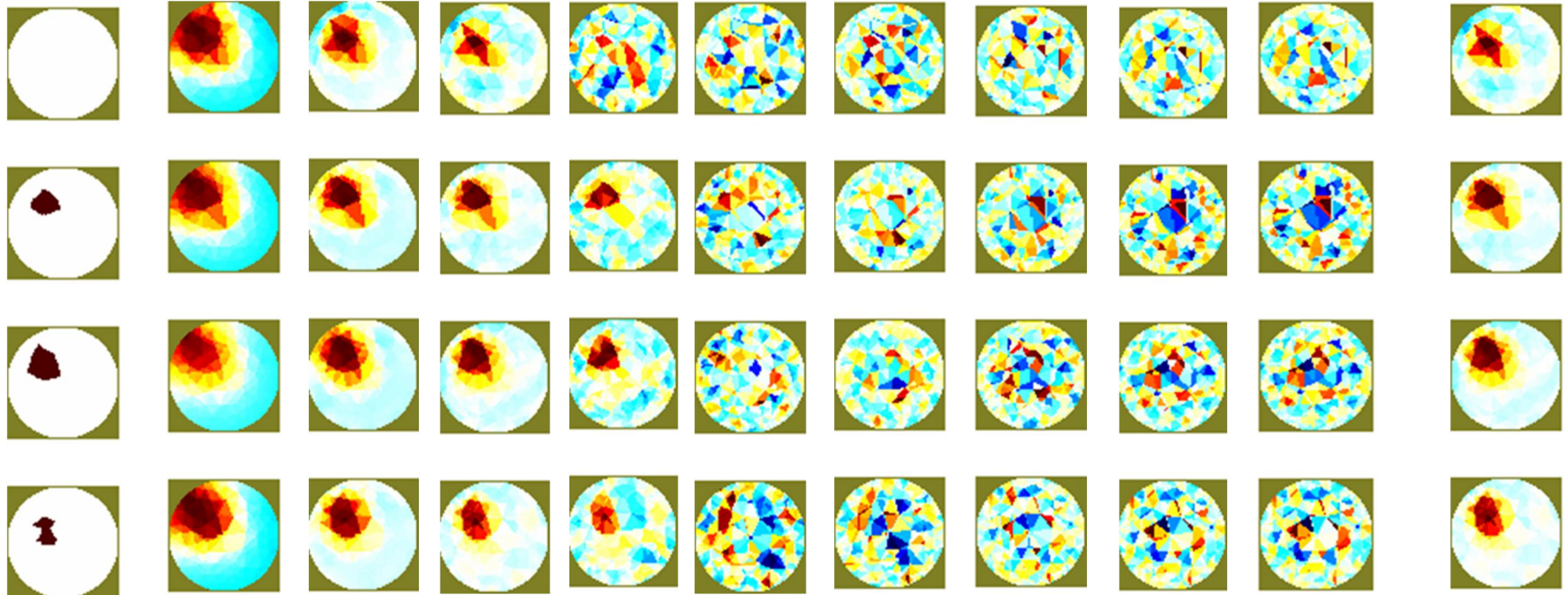


Figure 4.12 Proposed opposite protocol (2-electrodes per group). The first column is the original 3D perturbation presented as 2D coronal slices of the cylindrical phantom at levels \mathbf{h} . The columns (2–10) are the reconstructions for various values of the regularisation parameter $\lambda = \{1.00000\text{e-}001, 1.33352\text{e-}002, 1.77828\text{e-}003, 2.37137\text{e-}004, 3.16228\text{e-}005, 4.21697\text{e-}006, 4.62341\text{e-}007, 7.49894\text{e-}008, 1.00000\text{e-}008\}$, and the last column represents the reconstructed image resulted from the regularisation parameter produced though the L-curve criterion.

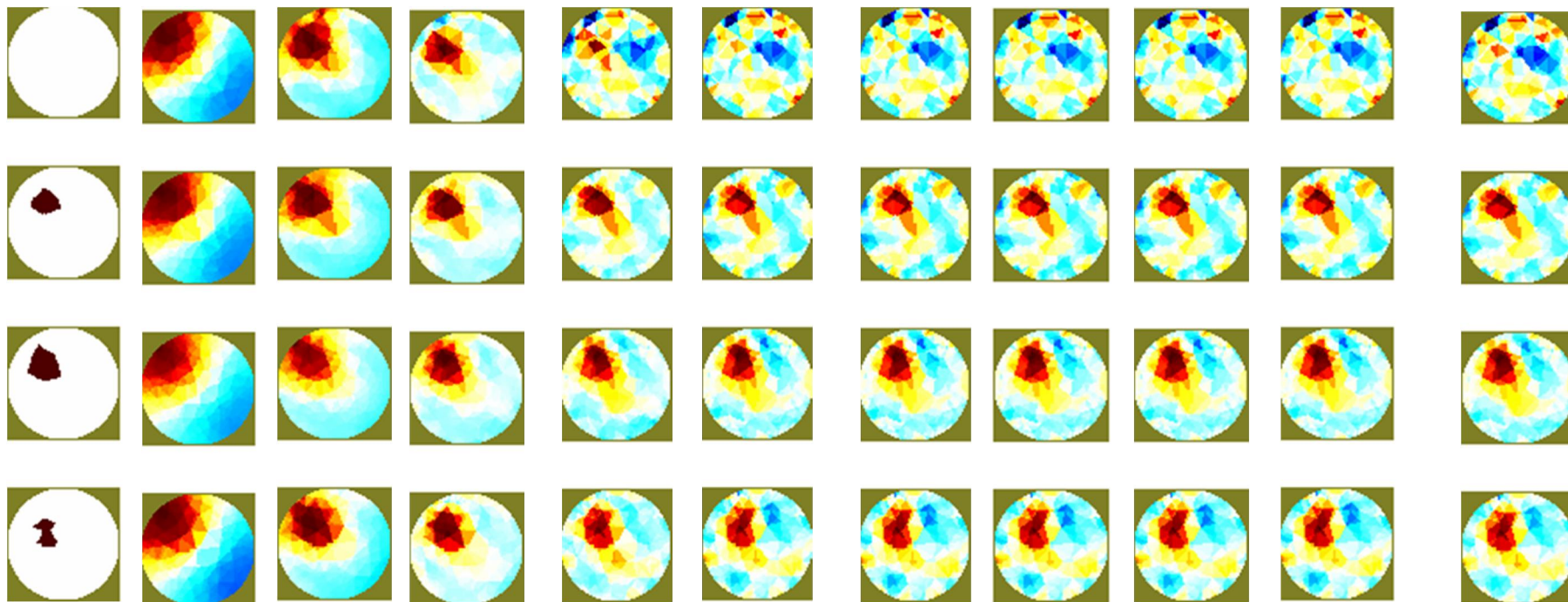


Figure 4.13 Proposed opposite protocol (6 electrodes per group). The first column is the original 3D perturbation presented as 2D coronal slices of the cylindrical phantom at levels **h**. The columns (2–10) are the reconstructions for various values of the regularisation parameter $\lambda = \{1.00000e-001, 1.33352e-002, 1.77828e-003, 2.37137e-004, 3.16228e-005, 4.21697e-006, 4.62341e-007, 7.49894e-008, 1.00000e-008\}$, and the last column represents the reconstructed image resulted from the regularisation parameter produced though the L-curve criterion.

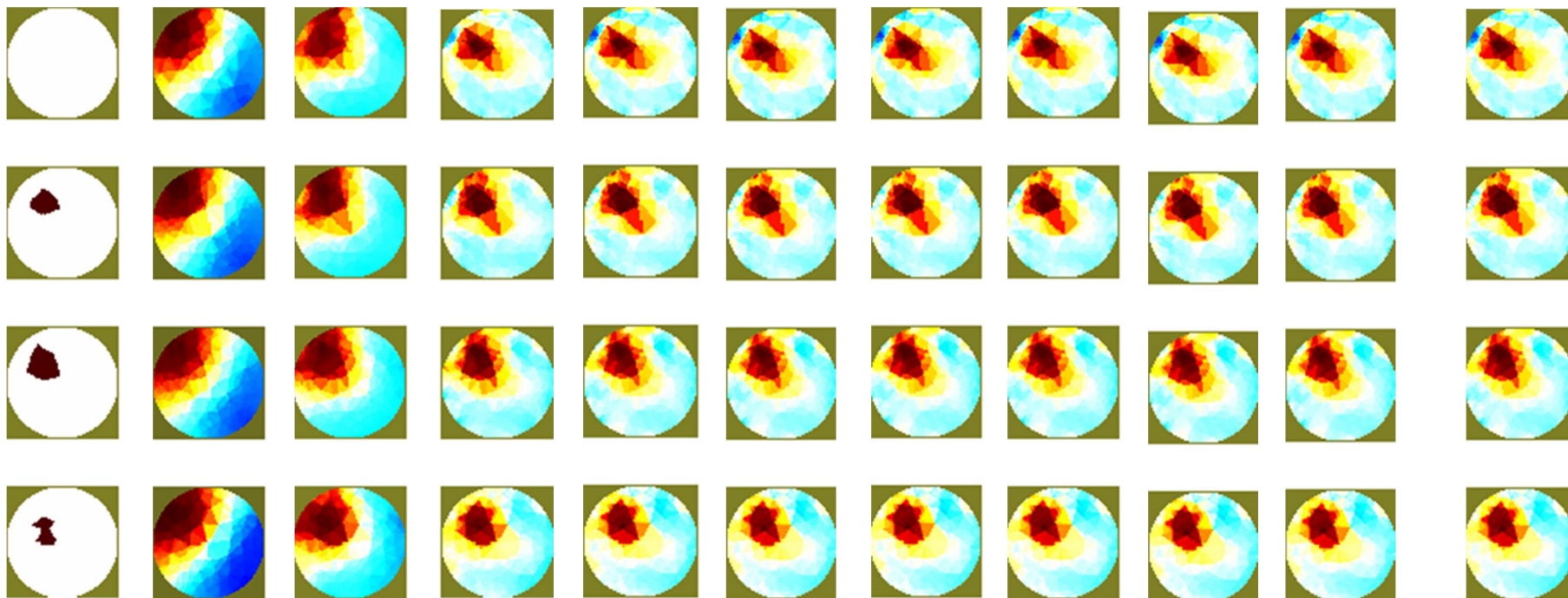


Figure 4.14 Proposed opposite protocol (8 electrodes per group). The first column is the original 3D perturbation presented as 2D coronal slices of the cylindrical phantom at levels \mathbf{h} . The columns (2–10) are the reconstructions for various values of the regularisation parameter $\lambda = \{1.00000\text{e-}001, 1.33352\text{e-}002, 1.77828\text{e-}003, 2.37137\text{e-}004, 3.16228\text{e-}005, 4.21697\text{e-}006, 4.62341\text{e-}007, 7.49894\text{e-}008, 1.00000\text{e-}008\}$, and the last column represents the reconstructed image resulted from the regularisation parameter produced though the L-curve criterion.

4.8 Summary

This chapter discussed the numerical stability and efficiency of the proposed current stimulation criterion when compared to the conventional opposite 2–electrodes pair stimulation protocol. The results have shown superiority, demonstrated in a better utilisation of the generalised singular values and therefore better performance, projected in higher gains. Further, by including the coupling effect between the regularisation \mathbf{R} and Jacobian matrices \mathbf{J} , it was numerically demonstrated that an appropriate choice of the matrix \mathbf{R} could essentially enhance the system performance.

Furthermore, another substantial advantage is the reduced computational overheads, due to the lesser amount of collected boundary voltage measurements m . In the same spirit, this simulation study also confirms the fact that employing an appropriate prior, the respective stimulation protocol gains increase indicating better utilisation of the available information. Lastly, the reconstruction quality is not affected by this caused reduction in the number of measurements, on the contrary, when a proper stimulation strategy coupled with an optimal regularisation parameter selection criterion and a proper prior are used, images with better resolution and wider regularisation range can be obtained.

Chapter 5

Conclusions and future work

Desire is the key to motivation, but it's determination and commitment to an unrelenting pursuit of your goal – a commitment to excellence – that will enable you to attain the success you seek.

Mario Andretti

5.1 The problem and the solution

Electrical Impedance Tomography is an inverse problem, and thus in order to achieve meaningful results, the regularisation process should couple the stimulation and measurement strategies with prior information about the characteristics of the conductivity distribution inside the medium. Further, as it was clearly demonstrated in the previous numerical results the single electrode group (i.e., the conventional stimulation strategy), simply put, performs poorly. This was manifested by the low values of the respective gains, which directly indicated the involvement of redundant singular values or those having extremely low values, which are no good for solving the problem at hand. Although an attempt to enhance performance through increasing the number or configuration of the electrodes has taken place, a reduction in the respective gains, and therefore the performance of the system, has otherwise occurred. Therefore, the proposed compound–electrode pair strategy has outperformed the conventional stimulation methods through a better utilisation of the available singular values. This technique appears to ‘automatically’ filter out ‘useless’ singular values, i.e., those who lie below the level of Picard’s coefficients.

On the other hand, by using GSVD analysis, one could essentially provide a good indication of the amount of information that a specific coupling (\mathbf{J} , \mathbf{R}) could offer to the inverse problem, before actually solving Equation (3.21). In this light, it is of little surprise that the identity prior offered very little improvement in the

CHAPTER 5. CONCLUSIONS AND FUTURE WORK

performance of the system. Indeed, the poor performance indicated that major amendments in the selection of the regularisation matrix were necessitated.

As mentioned in Chapter two, solving the forward problem assumes a piecewise constant (per element) approximation for the real conductivity distribution,

$$\sigma \approx \sum_{i=1}^K \sigma_i \chi_i \quad (5.1)$$

where χ_i is the characteristic function having the value 1 on element i and 0 otherwise, and K is the number of elements constituting the discrete model, the size of the typically underdetermined version of the Jacobian is $\mathbf{J} \in \mathbb{R}^{m \times K}$, where practically $m \ll K$. Therefore, a sensible step is to establish a means of increasing the number of measurements m until, ideally, $m \approx K$. This means a significant increase in the number of measurements and, eventually, electrodes L .

Aside from impractical, an increased number of measurements m will contribute towards unrealistically high computational overheads both for the assembly and the inversion of the dense matrix \mathbf{J} (not to mention possible ill-conditioning). Therefore, should a classical 2-electrode pair stimulation and measurement strategy be deployed, a practical upper bound in terms of available computational resources is encountered.

On the other hand, taking into account that we are dealing with an inverse problem, it is essential for stability to only utilise a subset of the available singular values spectrum, as suggested by the singular value analysis of Section 3.3. Moreover, in order to factor in the role of the regularisation matrix \mathbf{R} as well as the presence of the noise in the measurements, the GSVD analysis, in particular, is recalled.

5.2 Thesis deliverables

As mentioned earlier, the EIT imaging modality suffers from poor spatial resolution due to its sensitivity to noise and boundary voltage measurements [1],[101]. Also, EIT images are often subtracted from a reference image so that errors caused from electrode movement or unknown boundary shape are minimised. The EIT imaging modality results in reconstructed images that are differential in nature rather than static. The previous two reasons usually prevent the use of EIT in the diagnosis of a number of diseases and make it less comparable to modalities such as the CT and MRI [38].

Therefore, throughout this research, it was numerically demonstrated that by engaging more than one electrodes in the stimulation pattern, significant computational savings could be reported. Moreover, it was shown that unlike conventional systems, in the proposed configuration, as the number of electrodes increases so does the performance of the proposed system. Simulations on simple domains with varying numbers of electrode rings and number of electrodes per ring were presented. Representative reconstructions for a 3D cylindrical tank were provided to emphasise that despite the reduction in the number of collected measurements, no compromise in the quality of the reconstructed images was reported.

5.3 Further Work

This study is part of our long term goal in the Information Engineering and Medical Imaging Group at City University London to derive model reduction schemes in EIT without compromising robustness and/or the quality of acquired EIT data/images. In this regard, a reduction in the number of measurements m was achieved and essentially reflected on the Jacobian matrix \mathbf{J} .

It would be of great interest to verify the numerical findings herein with realistic measurements. The current bottleneck however, is that most available EIT systems are configured (hardware-wise) to fire on single-electrode groups and are typically

CHAPTER 5. CONCLUSIONS AND FUTURE WORK

manufactured with a small number of electrodes. As such, as long as a multiple-electrode pair system becomes available, results can be confirmed in an experimental setting.

A recent research initiative on the electrode configuration for EIT systems [104] has demonstrated that by having the electrodes as small and as closely spaced as possible, it was possible to have a better estimate of the conductivity of a surface perturbation like colo-rectal cancer. However, depending on the depth to which the perturbation had grown, different electrode spacings demonstrated varied levels of sensitivity. This work is of great importance to tackle the various non-uniform medium such as soft tissue imaging.

On the image reconstruction front, Polydorides *et al* [105] have shown promising results in reducing numerical overheads when calculating the solution of the nonlinear EIT reconstruction problem. This broadens the horizon for a potential cooperation by utilising the multi-stimulation current patterns along with the reduced mathematical complexity of solving the non-linear inverse problem to achieve the EIT's main goal of producing a better resolution images with less complexity.

It is also worth mentioning the efforts in [106] and [107] which broke new grounds for achieving numerical efficiency in both forward and inverse problems.

In addition, in [92], the author proposed multi-level basis functions (wavelets) as basis functions for both the forward and inverse computations of the soft-field imaging problem in order to reduce the dimensionality of \mathbf{J} (by compression). This automatically enables the 'multi-level Jacobian' and hence the multi-level version of the forward version at no additional computational cost. Hence, it is sensible therefore, to couple the ideas developed in the current research with the ideas developed in [92] in order to offer a 'possibly primitive' model reduction scheme that makes use of no additional transformation aside from the ones required for the solution of the inverse problem. Needless to say that if appropriate, this could be further combined with other generic model reduction methods, e.g., statistical ones [102], to offer additional significant advantages in reconstruction times.

CHAPTER 5. CONCLUSIONS AND FUTURE WORK

On the other hand, there is no restriction on the use of nonlinear schemes to perform the reconstruction task. In fact, the proposed method appears to best suit nonlinear systems, where linearised steps are essential. Thus, the proposed method has the potential to enable additional computational savings. Not to mention that although real admittivities were considered herein, there is no obvious limitation for the complex case. In this manner, higher frequency models or a multi-frequency EIT system could also be studied.

References

- [1] Holder, D., Physics, *Electrical Impedance Tomography: Methods, History And Application*. Bristol: Institute of Physics Pub., 2005. Print.
- [2] Halter R.J., Hartov A., Paulsen KD., *Experimental justification for using 3D conductivity reconstructions in electrical impedance tomography*. *Physiol Meas*. 2007 Jul; **28**(7):S115–128.
- [3] Metherall, P. *et al.*, *Three–Dimensional Electrical Impedance Tomography*. *Nature*, 1996. **380**(6574): p. 509–12.
- [4] Triantis IF., Constantinou L., Kassanos P., Demosthenous A., Bayford RH., *Towards the development of a fully integrated circuit for multi-frequency impedance measurements*, 12th International Conference on EIT, 2001
- [5] Lionheart, W.R., *EIT reconstruction algorithms: pitfalls, challenges and recent developments*. *Physiol Meas*, 2004. **25**(1): p. 125–42.
- [6] Isakov, V., *Inverse Problems for Partial Differential Equations* Springer, 1997.
- [7] Boone, K., Barber, D. and Brown, D. *Imaging With Electricity: Report of the European Concerted Action on Impedance Tomography*. *Journal of Medical Engineering & Technology*, 1997. **21**(6): p. 201–232
- [8] Rigaud, B., Morucci, J.P., *Bioelectrical Impedance Techniques in Medicine Part III: Impedance Imaging First Section: General Concepts and Hardware*. *Critical. Reviews. in Biomedical. Engineering*, 1996. **24**(4–6): p. 467–597.
- [9] Rigaud, B. *et al.*, *Experimental Acquisition System for Impedance Tomography with Active Electrode Approach*. *Medical and Biological Engineering and Computing*, 1993. **31**(6): p. 593–599.
- [10] Smith *et al.*, *Real Time Electrical Impedance Imaging*. *Proceedings of the 12th Annual International Conference of the IEEE Engineering in Medicine and Biology Society*, 1990: p. 104–105.
- [11] Brown, B., and Barber, C., *Electrical Impedance Tomography*. *Colloquium on Functional Imaging*, 1994.
- [12] Casas, O. *et al.*, *A Parallel Broadband Real–Time System for Electrical Impedance Tomography*. *Physiol Meas*, 1996. **4A**: p. A1–A6.

REFERENCES

- [13] Kotre, C.J., *Electrical Impedance Tomography*. British Journal of Radiology, 1997. **70**(E SPI/1): p. S200–S205.
- [14] Guardo, R *et al.*, *An Experimental Study in Electrical Impedance Tomography Using Backprojection Reconstruction*. IEEE Transactions on Biomedical Engineering, 1991. **38**(7): p. 617–627.
- [15] Hansen PC,. *Rank–Deficient and Discrete Ill–Posed Problems: Numerical Aspects of Linear Inversion*, 1998 (SIAM, Philadelphia, PA)
- [16] Schorberl, J., *Netgen – An advancing front 2D/3D mesh generator based on abstract rules*. Computing and Visualization in Science, 1997. **1**(1): p. 41–52.
- [17] Wirgin, A., *The inverse crime*. ArXiv Mathematical Physics eprints arXiv.math–ph/0401050 2004.
- [18] Cheney, M., and Isaacson, D., *Distinguishability in impedance imaging*. IEEE Transactions on Biomedical Engineering, 1992. **39**(8): p. 852–60.
- [19] Dehghani, H *et al.*, *Excitation patterns in three–dimensional electrical impedance tomography*. Physiol Meas, 2005. **26**(2): p. S185–97.
- [20] Polydorides, N., McCann, H., *Electrode configurations for improved spatial resolution in Electrical Impedance Tomography*. Measurement Science and Technology, 2002. **13**(12): p. 1862.
- [21] Kleiner mann, F., N.J. Avis,. F.A. Alhargan,. *Analytical solution to the three–dimensional electrical forward problem for an elliptical cylinder*. Physiol Meas, 2002. **23**(1): p. 141–7.
- [22] Silvester, P.P.,. R.L. Ferrari,. *Finite Elements for Electrical Engineers*. 1996: Cambridge University Press.
- [23] Feynman, R.P., R.B. Leighton,. M.L. Sands,. *The Feynman lectures on physics*. 1965: Addison–Wesley.
- [24] Cheng, K.S *et al.*, *Electrode models for electric current computed tomography*. IEEE Trans Biomed Eng, 1989. **36**(9): p. 918–24.
- [25] Borsic, A., *Regularisation methods for imaging from electrical measurements*, 2002, PhD Thesis, Oxford Brookes University
- [26] Calderón, A.P., *On an inverse boundary value problem*. Computational & Applied Mathematics, 2006. **25**: p. 133–138.
- [27] Somersalo, E., M. Cheney,. D. Isaacson,. *Existence and uniqueness for electrode models for electric current computed tomography*. SIAM J. Appl. Math., 1992. **52**(4): p. 1023–1040.

REFERENCES

- [28] Paulson, K., W. Breckon, M. Pidcock, *Electrode modelling in electrical impedance tomography*. SIAM J. Appl. Math., 1992. **52**(4): p. 1012–1022.
- [29] Stein, E., Olgierd C. Zienkiewicz, *A pioneer in the development of the finite element method in engineering science*. Steel Construction, 2009. **2**(4): p. 264–272.
- [30] Brenner, S.C., L.R. Scott, *The Mathematical Theory of Finite Element Methods*. 2002: Springer–Verlag.
- [31] Reddy, J.N., *Applied functional analysis and variational methods in engineering*. 1991: Krieger Pub. Co.
- [32] Mikhlin, S.G., *Variational methods in mathematical physics*. 1964: Pergamon Press; [distributed by Macmillan, New York].
- [33] Sadiku, M.N.O., *Numerical Techniques in Electromagnetics*. 2000: CRC Press.
- [34] Brown, B.H., A.D. Seagar, *The Sheffield data collection system*. Clin Phys Physiol Meas, 1987. **8 Suppl A**: p. 91–7.
- [35] Malmivuo, J., Plonsey, R., *Bioelectromagnetism: Principles and Applications of Bioelectric and Biomagnetic Fields*. 1995: Oxford University Press.
- [36] Hua P., Webster J. G., Tompkins W. J., *Effect of the measurement method on noise handling and image quality of EIT imaging*. In Proc. Ninth Int. Conf. IEEE Eng. In Med. And Biol. Society, IEEE, New York, N.Y., 1987. **2**: p. 1429–30.
- [37] Gisser, D.G., Isaacson, D., Newell, J.C., *Current topics in impedance imaging*. Clin Phys Physiol Meas, 1987. **8 Suppl A**: p. 39–46.
- [38] Zifan, A., *Integration of Geometric and Finite Element Modelling of the Thorax for EIT Lung Imaging*, in *Electrical and Electronic Engineering* 2011, PhD Thesis, City University London: London.
- [39] Breckon, W.R., *Image reconstruction in electrical impedance tomography*, 1990, Oxford Polytechnic.
- [40] Vauhkonen, M., *Electrical impedance tomography and prior information*, 1997, Kuopio University: Kuopio.
- [41] Holder, D.S., Gonzalez-Correa C A., Tidswell, T., Gibson, A., Cusick, G., Bayford, R H., *Assessment and calibration of a low-frequency system for electrical impedance tomography (EIT), optimized for use in imaging brain function in ambulant human subjects*. Annals of New York Academy of Science 1999. **873**.

REFERENCES

- [42] Sadleir, R.J., R.A. Fox., *Detection and quantification of intraperitoneal fluid using electrical impedance tomography*. Biomedical Engineering, IEEE Transactions on, 2001. **48**(4): p. 484–491.
- [43] Anita, H.M., *Numerical–Methods for Scientist and Engineers*. Birkhauser–verlag, 2002.
- [44] Press, W.H., *Numerical Recipes: The Art of Scientific Computing*. 2007: Cambridge University Press.
- [45] Yorkey, T.J., J.G. Webster., W.J. Tompkins., *Comparing reconstruction algorithms for electrical impedance tomography*. IEEE Trans Biomed Eng, 1987. **34**(11): p. 843–52.
- [46] Tikhonov, A.N. and V.I.A. Arsenin, *Solutions of ill–posed problems*. 1977: Winston.
- [47] Polydorides, N., *Image reconstruction algorithms for soft–field tomography*, in *Institute of Science and Technology 2002*, PhD Thesis, University of Manchester: Manchester.
- [48] Kaipio, J.P. et al., "Statistical inversion and Monte Carlo sampling methods in electrical impedance tomography" *EndNote*. Inverse problems, 2000. **16**: p. 1487–1522.
- [49] Williams, R.A., Beck, S., Beck, M.S., *Process tomography: principles, techniques, and applications*. 1995: Butterworth–Heinemann.
- [50] Kolehmainen, V et al., *Assessment of errors in static electrical impedance tomography with adjacent and trigonometric current patterns*. Physiol Meas, 1997. **18**(4): p. 289–303.
- [51] Allers, A., Santosa, F., *Stability and resolution analysis of a linearized problem in electrical impedance tomography*. Inverse problems 1997. **7** p. 515–535.
- [52] Neumaier, A., *Solving Ill–Conditioned and Singular Linear Systems: A Tutorial on Regularization*. SIAM Review, 1998. **40**(3): p. 636–666.
- [53] Blue, R.S., *A real–time three–dimensional linearized reconstruction algorithm generalized for multiple planes of electrodes*, 1997, Rensselaer Polytechnic Institute Troy, NY.
- [54] Cheney, M., Isaacson, D., *Electrical impedance tomography*. SIAM Review, 1999. **41** (1): p. 85–101.
- [55] Goble J. C. et al., *Electrical impedance tomography in three dimensions (1990)*. Proceedings of the Biomedical Engineering Society conference, 1990.

REFERENCES

- [56] Kohn, R.V ., *Determining Conductivity by Boundary Measurements*. Communications in Pure and Applied Mathematics 1984. **37**.
- [57] Loke, M.H., R.D. Barker., *Rapid least-squares inversion of apparent resistivity pseudosections by a quasi-Newton method*. Geophysical Prospecting, 1996. **44**(1): p. 131–152.
- [58] Cheney, M *et al.*, *NOSER: An algorithm for solving the inverse conductivity problem*. International Journal of Imaging Systems and Technology, 1990. **2**(2): p. 66–75.
- [59] Herwanger, J.V., Pain, C.C., De Oliveira, C.R.E., *Electrical and seismic inversion in anisotropic inhomogeneous media*. Fourth International Conference on Inverse Problems in Engineering, 2002.
- [60] Dorn, O *et al.*, *A nonlinear inversion method for 3D electromagnetic imaging using adjoint fields*. Inverse Problems, 1999. **15** (6): p. 1523–1558.
- [61] Webster, J.G., *Electrical impedance tomography*. 1990: Adam Hilger.
- [62] Wexler, A., *Electrical impedance imaging in two and three dimensions*. Clin Phys Physiol Meas, 1988. **9 Suppl A**: p. 29–33.
- [63] Arridge, S.R., *Topical review: Optical tomography in medical imaging*. Inverse Problems 1999. **15**: p. R41–R93.
- [64] Vauhkonen, M *et al.*, *Tikhonov regularization and prior information in electrical impedance tomography*. Medical Imaging, IEEE Transactions on, 1998. **17**(2): p. 285–293.
- [65] Lionheart, W.R.B., *Conformal uniqueness results in anisotropic electrical impedance imaging*. Inverse Problems 1997. **13**: p. 125–134.
- [66] Dorn, O *et al.*, *Sensitivity analysis of a nonlinear inversion method for 3D electromagnetic imaging in anisotropic media*. Inverse Problems, 2002. **18**(2): p. 285–317.
- [67] Borcea, L., Berryman, J.G., Papanicolaou, G.C., *Matching pursuit for imaging high-contrast conductivity*. Inverse Problems, 1999. **15**: p. 811–849.
- [68] Sylvester, J., Uhlmann, G., *A global uniqueness theorem for an inverse boundary value problem* Annals of Mathematics, 1987. **125**: p. 153–169.
- [69] Golub, G.H., Van Loan, C.F., *Matrix Computations*. 1996: Johns Hopkins University Press.

REFERENCES

- [70] Yang, W. Q. *et al.*, *Image-Reconstruction Algorithm Based on Landweber's Iteration Method for Electrical-Capacitance Tomography*. Measurement Science and Technology, 1999. **10**(11): p. 1065–1069.
- [71] Morozov, V.A., Nashed, Z., *Methods for solving incorrectly posed problems*. 1984: Springer-Verlag.
- [72] Bauer, F., Kindermann, Z., *The quasi-optimality criterion for classical inverse problems* Inverse Problems, 2008. **24**(035002): p. 20.
- [73] Hansen, P.C., O'Leary, D.P., *The use of the L-curve in the regularization of discrete ill-posed problems*. SIAM J. Sci. Comput., 1993. **14**(6): p. 1487–1503.
- [74] Lawson, C.L., Hanson, R.J., *Solving Least Squares Problems*. 1974: SIAM.
- [75] Desbat, L., Girard, D., *The “Minimum Reconstruction Error” Choice of Regularization Parameters: Some More Efficient Methods and Their Application to Deconvolution Problems*. SIAM Journal on Scientific Computing, 1995. **16**(6): p. 1387–1403.
- [76] Kilmer, M.E., O'Leary, D.P., *Choosing Regularization Parameters in Iterative Methods for Ill-Posed Problems*. SIAM J. Matrix Anal. Appl., 2000. **22**(4): p. 1204–1221.
- [77] Kohn, R.V., Vogelius, M., *Relaxation of a variational method for impedance computed tomography*. Communications on Pure and Applied Mathematics, 1987. **40**(6): p. 745–777.
- [78] Wexler, A., Fry, B., Neuman, M.R., *Impedance-computed tomography algorithm and system*. Appl. Opt., 1985. **24**(23): p. 3985–3992.
- [79] Santos, R.J., *Preconditioning conjugate gradient with symmetric algebraic reconstruction technique (ART) in computerized tomography*. Appl. Numer. Math., 2003. **47**(2): p. 255–263.
- [80] Wang, H.X., Zhu, X.M., Zhang, L.F., *Conjugate Gradient Algorithm for Electrical Capacitance Tomography*. Journal of Tianjin University Science and Technology, 2005. **38**(1): p. 1–4.
- [81] Zhu, W. *et al.*, *Iterative total least-squares image reconstruction algorithm for optical tomography by the conjugate gradient method*. J Opt Soc Am A Opt Image Sci Vis, 1997. **14**(4): p. 799–807.
- [82] Bonesky, T., *Morozov's discrepancy principle and Tikhonov-type functionals*. Inverse Problems 2009 **25**(1).
- [83] Kotre, C.J., *EIT image reconstruction using sensitivity weighted filtered backprojection*. Physiol Meas, 1994. **15 Suppl 2a**: p. A125–36.

REFERENCES

- [90] Soleimani, M., *Image and shape reconstructions in Magnetic induction and Electrical Impedance Tomography*, 2005, University of Manchester: UK.
- [91] Dai, T., *Image reconstruction in EIT using advanced regularization frameworks*, 2008, Carleton University Canada.
- [92] Kantartzis, P., *Multilevel soft-field tomography*, 2011, PhD Thesis, City University London: UK.
- [93] Lionheart, W.R., J. Kaipio, C.N. McLeod, *Generalized optimal current patterns and electrical safety in EIT*. *Physiol Meas*, 2001. **22**(1): p. 85–90.
- [94] Adler, A., Gaggero, P.O., Maimaitijiang, Y., *Adjacent stimulation and measurement patterns considered harmful*. *Physiol Meas*, 2011. **32**(7): p. 731–44.
- [95] Adler, A., Youmaran, R., Lionheart, W.R., *A measure of the information content of EIT data*. *Physiol Meas*, 2008. **29**(6): p. S101–9.
- [96] Boyle, A., Adler, A., *The impact of electrode area, contact impedance and boundary shape on EIT images*. *Physiol Meas*, 2011. **32**(7): p. 745–54.
- [97] Forsyth, J *et al.*, *Optical breast shape capture and finite-element mesh generation for electrical impedance tomography*. *Physiol Meas*, 2011. **32**(7): p. 797–809.
- [98] Hansen, P.C., *Analysis of discrete ill-posed problems by means of the L-curve*. *SIAM Review*, 1992. **34**(4): p. 561–580.
- [99] Science, J.S.C.a.V.i., *Netgen – an advancing front 2D/3D-mesh generator based on abstract rules*. *Computing and Visualization in Science*, 1997. **1**(1): p. 41–52.
- [100] *EIDORS*, *Electrical impedance tomography and diffuse optical tomography reconstruction software*. <http://eidors3d.sourceforge.net/>.
- [101] Sylvester, J., Uhlmann, G., *A uniqueness theorem for an inverse boundary value problem in electrical prospection*. *Communications on Pure and Applied Mathematics*, 1986. **39**(1): p. 91–112.
- [102] Nissinen, A., Heikkinen, L. M., Kaipio, J. P., *The Bayesian approximation error approach for electrical impedance tomography—experimental results*. *Measurement Science and Technology*, 2008. **19**(1): p. 015501.
- [103] Polycarpou, A.C., *Introduction to the Finite Element Method in Electromagnetics*. 2006: Morgan & Claypool Publishers.

REFERENCES

- [104] Shiraz, A., Demosthenous A., and Bayford R., *Towards an Optimised Electrode Design for Enhanced Colorectal Tumour Margin Identification in EIS Using Finite Element Methods.*, 2015
- [105] Polydorides, N., Ouypornkochagorn, T & McCann, H., *An approximate gradient for fast nonlinear inversion of the EIT model.* in 16th International Conference on Biomedical Applications of Electrical Impedance Tomography., 2015.
- [106] Adler, A., Braun, F., Solà, J., *Distinguishability as a noise performance metric for EIT algorithms.*, 2015
- [107] Mohamadou, Y., Park, J H., Wi, H., Oh T I., Woo E J., *Micro-electrode array based microscopic EIT system for characterization of cell and tissue.*, 2015

Appendix A

Deriving the stiffness matrix for a simple 2D medium using the Finite Element Method

In this section, the individual integral components comprising the sub-matrices \mathbf{A}_M , \mathbf{A}_Z , \mathbf{A}_W , and \mathbf{A}_D , as appear in the system in Equation 2.45 are evaluated using the finite element method. The medium is nominated to be a 2D shape, for simplicity reasons, and segmented into triangular tetrahedral as Figure 1 roughly illustrates.

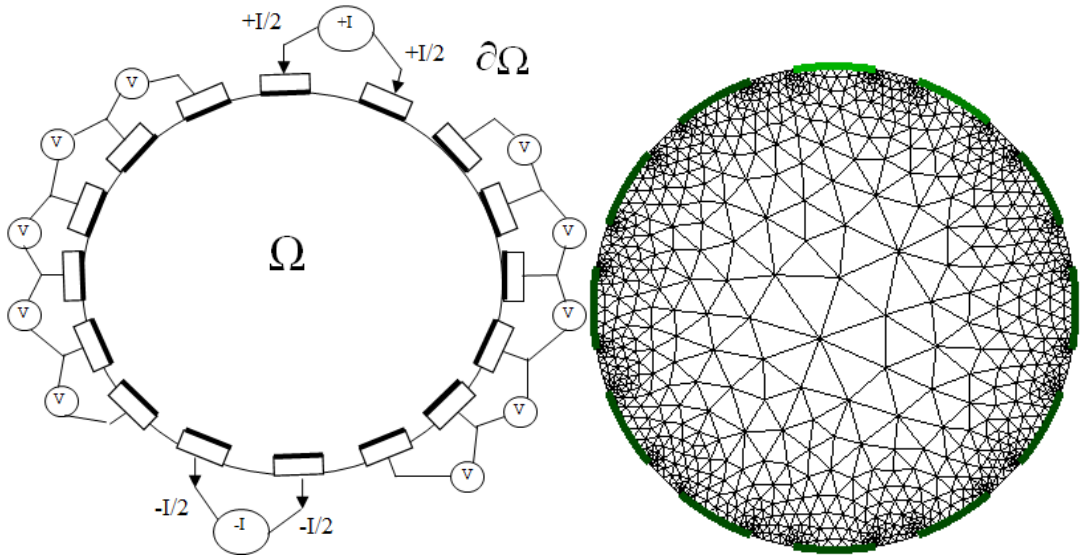


Figure A-1 A rough illustration of a 2D with L electrodes attached at its boundary. Right: Continuous domain, and left is the discretised one.

Basis/Interpolation functions

The basis functions $N_i(\mathbf{x})$ where $(\mathbf{x} \in \Omega) \in \mathbb{R}^2$, used to interpolate the electric potential over the vertices comprising the mesh, are chosen to be a piecewise linear, and having a value of “1” on vertex i and “0” at the other vertices, i.e.,

$$N_i = \begin{cases} 1 & \text{on vertex } i, \\ 0 & \text{otherwise.} \end{cases} \quad (1)$$

APPENDIX A.

Therefore, the continuous electrical potential $\phi(\mathbf{x})$ inside the mesh can be approximated over the vertices using this interpolation functions as,

$$\begin{aligned}\phi(\mathbf{x}) &\cong \sum_{i=1}^n \varphi_i N_i(\mathbf{x}) \\ &\cong \varphi_1 N_1(\mathbf{x}) + \varphi_2 N_2(\mathbf{x}) + \dots + \varphi_n N_n(\mathbf{x})\end{aligned}\quad (2)$$

where the vector $[\varphi_1, \dots, \varphi_n]^T \in \mathbb{R}^n$ represents the discrete approximations to the potential.

Generally speaking, the basis (or interpolation functions, as many may refer to) should possess the following characteristics. Firstly, they should preserve continuity of the function ϕ across inter-element boundaries, and secondly, as highlighted in Chapter 2, they must be at least once differentiable and, finally, they must be complete polynomials in order to provide sufficient representation of the solution's behaviour in the finite element domain [103].

Having assumed a 2D domain, each linear triangular element composing the domain in the xy -plane, as illustrated in Figure 2, consists of three vertices which correspond to the three nodes of the elements. Conventionally, these nodes are locally numbered in a counter-clockwise manner to avoid having a negative area using the Jacobian⁴ [103].

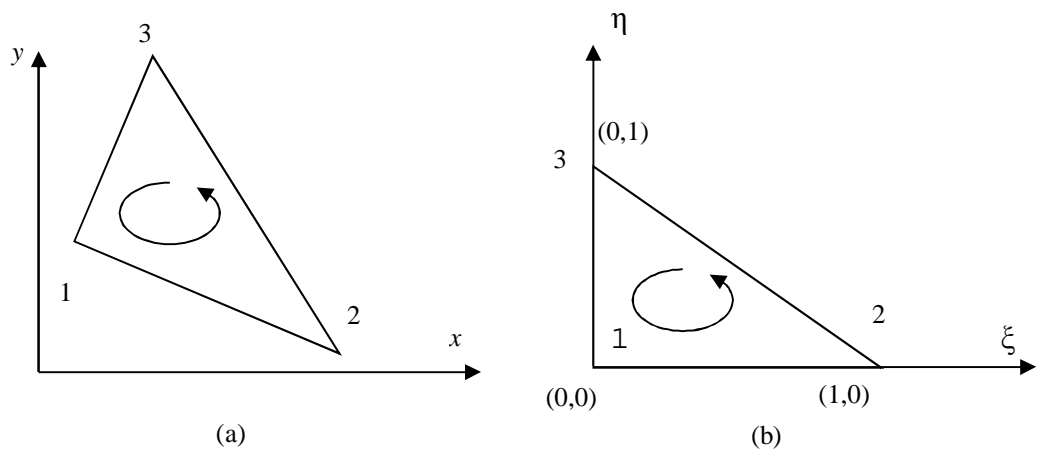


Figure A-2 (a) Linear triangular element in the xy -plane. (b) Linear triangular element in the $\zeta\eta$ -plane.

⁴ In this context, the Jacobian represents the matrix of derivatives deployed to transform a system from one coordinate system to another.

APPENDIX A.

The sub-matrices of the linear system described in Equation 2.45 include integration either over the domain of interest Ω or the boundary of the domain $\partial\Omega$. However, one can perform the integral over individual elements Ω_e and then map it onto the global matrix \mathbf{A} for the entire domain. On the other hand, using the xy -coordinates might not be a good idea because the limits of the integration change every time a new element is considered.

Therefore, by transferring the element from the regular domain onto another domain (or as referred to as the natural or the master domain), the limits of integration involved in the weak formulation do not change every time a new element is considered. Hence, it is advisable that the interpolation functions should be derived based on the master element rather than the local element.

Figure 2(b) shows that at any point on the master element ($0 \leq \xi \leq 1$ and $0 \leq \eta \leq 1$) the electric potential can be expressed as,

$$\begin{aligned} \phi^e(\xi, \eta) &\cong \sum_{i=1}^3 \phi_i^e N_i(\xi, \eta) \\ &\cong \phi_1^e N_1(\xi, \eta) + \phi_2^e N_2(\xi, \eta) + \phi_3^e N_3(\xi, \eta) \end{aligned} \quad (3)$$

where ϕ_1^e , ϕ_2^e , and ϕ_3^e are the values of the electric potential at the three vertices of the triangle, and the functions $N_1(\xi, \eta)$, $N_2(\xi, \eta)$, and $N_3(\xi, \eta)$ are the linear basis function corresponds to interpolating the potential to a triangle nodes 1, 2, and 3, respectively.

The linear representation of the interpolation function $N(\xi, \eta)$ is of the form,

$$N(\xi, \eta) = c_1 + c_2\xi + c_3\eta \quad (4)$$

hence, by employing the fact that $N_1(\xi, \eta)$ as the value of “1” at node “1” and “0” at the other two nodes, the constants c_1 , c_2 , and c_3 can be calculated as,

At node “1”

$$N_1(0, 0) = c_1 + c_2(0) + c_3(0) = 1 \text{ hence, } c_1 = 1$$

At node ”2”

$$N_1(1, 0) = 1 + c_2(1) + c_3(0) = 0 \quad \text{hence,} \quad c_2 = -1$$

APPENDIX A.

At node "3"

$$N_1(0,1) = 1 + -1(0) + c_3(1) = 0 \text{ hence, } c_3 = -1$$

Therefore, the interpolation function $N_1(\xi, \eta)$ can be expressed as,

$$N_1(\xi, \eta) = 1 - \xi - \eta \quad (5)$$

Next, the same concept applies for both $N_2(\xi, \eta)$ and $N_3(\xi, \eta)$ where $N_2(\xi, \eta)$ has the value of "1" at node "2" and "0" at the other nodes i.e., "1" and "3". And the function $N_3(\xi, \eta)$ has the value of "1" at node "3" and "0" at the other two nodes.

Hence, using a simple substitution, one can simply get,

$$N_2(\xi, \eta) = \xi \quad (6)$$

$$N_3(\xi, \eta) = \eta \quad (7)$$

For isoparametric elements, the same interpolation functions used to interpolate the electric potential inside an element are also used to interpolate the space coordinates x and y . In other words,

$$x = x_1^e N_1 + x_2^e N_2 + x_3^e N_3 = \sum_{i=1}^3 x_i^e N_i \quad (8)$$

$$y = y_1^e N_1 + y_2^e N_2 + y_3^e N_3 = \sum_{i=1}^3 y_i^e N_i$$

and by substituting the values of N_1 , N_2 , and N_3 calculated in (5), (6), and (7) and into (8) yields

$$x = x_1^e + \bar{x}_{21}\xi + \bar{x}_{31}\eta \quad (9)$$

$$y = y_1^e + \bar{y}_{21}\xi + \bar{y}_{31}\eta$$

where

$$\begin{aligned} \bar{x}_{21} &= x_2^e - x_1^e \\ \bar{x}_{31} &= x_3^e - x_1^e \\ \bar{x}_{21} &= x_2^e - x_1^e \\ \bar{y}_{21} &= y_2^e - y_1^e \\ \bar{y}_{31} &= y_3^e - y_1^e \end{aligned} \quad (10)$$

APPENDIX A.

Evaluation of element matrices

For each element Ω_k the respective sub-matrices \mathbf{A}_M^k , \mathbf{A}_Z^k , \mathbf{A}_W^k , and \mathbf{A}_D^k , are solved with respect to previously derived linear basis functions. Then, for the matrix \mathbf{A}_M^k which can be written as,

$$\mathbf{A}_{Mi,j}^k = \sigma_k \int_{\Omega_k} \nabla N_i \cdot \nabla N_j d\Omega_k \quad (11)$$

or simply,

$$A_{Mi,j}^k = \iint_{x,y} \sigma \nabla N_i \cdot \nabla N_j dx dy \quad \forall x, y \in \Omega_k$$

Given the interpolation functions N_1, N_2 and N_3 , the coordinate transformation

from the xy onto the $\xi\eta$ axes, and using the chain rule to obtain $\frac{\partial N}{\partial \xi}$ and $\frac{\partial N}{\partial \eta}$ as,

$$\begin{aligned} \frac{\partial N}{\partial \xi} &= \frac{\partial N}{\partial x} \frac{\partial x}{\partial \xi} + \frac{\partial N}{\partial y} \frac{\partial y}{\partial \xi} \\ \frac{\partial N}{\partial \eta} &= \frac{\partial N}{\partial x} \frac{\partial x}{\partial \eta} + \frac{\partial N}{\partial y} \frac{\partial y}{\partial \eta} \end{aligned} \quad (12)$$

or in a matrix form,

$$\begin{bmatrix} \frac{\partial N}{\partial \xi} \\ \frac{\partial N}{\partial \eta} \end{bmatrix} = \begin{bmatrix} \frac{\partial x}{\partial \xi} & \frac{\partial y}{\partial \xi} \\ \frac{\partial x}{\partial \eta} & \frac{\partial y}{\partial \eta} \end{bmatrix} \begin{bmatrix} \frac{\partial N}{\partial x} \\ \frac{\partial N}{\partial y} \end{bmatrix} \quad (13)$$

The 2×2 square matrix is called the *Jacobian matrix*, denoted by \mathbf{J}^\diamond , and can be evaluated using the expressions in (9) as,

$$\mathbf{J}^\diamond = \begin{bmatrix} \bar{x}_{21} & \bar{y}_{21} \\ \bar{x}_{31} & \bar{y}_{31} \end{bmatrix} \quad (14)$$

The coordinate transformation in (13) can be rearranged by inverting the Jacobian matrix and expressing the matrix system in the following form,

$$\begin{bmatrix} \frac{\partial N}{\partial x} \\ \frac{\partial N}{\partial y} \end{bmatrix} = \mathbf{J}^{\diamond-1} \begin{bmatrix} \frac{\partial N}{\partial \xi} \\ \frac{\partial N}{\partial \eta} \end{bmatrix} \quad (15)$$

where $\mathbf{J}^{\diamond-1}$ essentially denotes the inverse of the Jacobian matrix, and is given by,

APPENDIX A.

$$\mathbf{J}^{\diamond-1} = \frac{1}{|\mathbf{J}^\diamond|} \begin{bmatrix} \bar{y}_{31} & -\bar{y}_{21} \\ -\bar{x}_{31} & \bar{x}_{21} \end{bmatrix} \quad (16)$$

where $|\mathbf{J}^\diamond|$ is the determinant of the Jacobian matrix and calculated as,

$$|\mathbf{J}^\diamond| = \bar{x}_{21}\bar{y}_{31} - \bar{x}_{31}\bar{y}_{21} = 2A_e \quad (17)$$

and A_e denotes the area of the triangle. The determinant of the Jacobian matrix is equal to twice the area of the triangular element provided that the local node numbers of the triangle follow a counter-clockwise sense of the numbering. Thus, in forming the connectivity information array of any finite element mesh, it is instructive that the local nodes of each triangle be numbered in a counter-clockwise direction. Using (15–17) and (5–7) would result in

$$\begin{aligned} \begin{bmatrix} \frac{\partial N}{\partial \xi} \\ \frac{\partial N}{\partial \eta} \end{bmatrix} &= \frac{1}{2A_e} \begin{bmatrix} \bar{y}_{31} & -\bar{y}_{21} \\ -\bar{x}_{31} & \bar{x}_{21} \end{bmatrix} \begin{bmatrix} \frac{\partial N}{\partial x} \\ \frac{\partial N}{\partial y} \end{bmatrix} \\ &= \frac{1}{2A_e} \begin{bmatrix} \bar{y}_{31} & -\bar{y}_{21} \\ -\bar{x}_{31} & \bar{x}_{21} \end{bmatrix} \begin{bmatrix} -1 \\ -1 \end{bmatrix} \\ &= \frac{1}{2A_e} \begin{bmatrix} \bar{y}_{21} - \bar{y}_{31} \\ \bar{x}_{31} - \bar{x}_{21} \end{bmatrix} \\ &= \frac{1}{2A_e} \begin{bmatrix} \bar{y}_{23} \\ \bar{x}_{32} \end{bmatrix} \end{aligned} \quad (18)$$

In other words,

$$\begin{aligned} \frac{\partial N_1}{\partial x} &= \frac{\bar{y}_{23}}{2A_e} \\ \frac{\partial N_1}{\partial y} &= \frac{\bar{x}_{32}}{2A_e} \end{aligned} \quad (19)$$

Similarly,

$$\begin{aligned} \frac{\partial N_2}{\partial x} &= \frac{\bar{y}_{31}}{2A_e} \\ \frac{\partial N_2}{\partial y} &= \frac{\bar{x}_{13}}{2A_e} \end{aligned} \quad (20)$$

APPENDIX A.

and

$$\begin{aligned}\frac{\partial N_3}{\partial x} &= \frac{\bar{y}_{12}}{2A_e} \\ \frac{\partial N_3}{\partial y} &= \frac{\bar{x}_{21}}{2A_e}\end{aligned}\quad (21)$$

One can rewrite integral $A_{M^k i, j}$ as,

$$\mathbf{A}_{Mi, j}^k = \sigma_k \iint_{xy} \left[\frac{\partial N_i}{\partial x} \frac{\partial N_j}{\partial x} + \frac{\partial N_i}{\partial y} \frac{\partial N_j}{\partial y} \right] dx dy \quad (22)$$

Performing the integration in (22) over the master element lying on the natural coordinate system, and using the transformation of a double integral from the regular coordinate system to the natural coordinate system is [31]

$$\iint_{xy} f(x, y) dx dy = \int_0^{1-\eta} \int_0^{\eta} f(x(\xi, \eta), y(\xi, \eta)) |\mathbf{J}^\diamond| d\xi d\eta \quad (23)$$

Using Equations (19–21) along with the Jacobian transformation in (23), the entries of element matrix $\mathbf{A}_{Mi, j}^k$ can be evaluated in a straightforward manner. Specifically,

$$\begin{aligned}\mathbf{A}_{M1,1}^k &= \int_0^{1-\eta} \int_0^{\eta} \sigma_k \left(\frac{\bar{y}_{23}}{2A_e} \frac{\bar{y}_{23}}{2A_e} \right) \left(\frac{\bar{x}_{32}}{2A_e} \frac{\bar{x}_{32}}{2A_e} \right) 2A_e d\xi d\eta \\ &= \sigma_k \left(\frac{(\bar{y}_{23})^2}{4A_e} \right) \left(\frac{(\bar{x}_{32})^2}{4A_e} \right)\end{aligned}\quad (24)$$

Similarly,

$$\mathbf{A}_{M1,2}^k = \mathbf{A}_{M2,1}^k = \sigma_k \left(\frac{\bar{y}_{23}\bar{y}_{31}}{4A_e} \right) \left(\frac{\bar{x}_{32}\bar{x}_{13}}{4A_e} \right) \quad (25)$$

$$\mathbf{A}_{M1,3}^k = \mathbf{A}_{M3,1}^k = \sigma_k \left(\frac{\bar{y}_{23}\bar{y}_{12}}{4A_e} \right) \left(\frac{\bar{x}_{32}\bar{x}_{21}}{4A_e} \right) \quad (26)$$

$$\mathbf{A}_{M2,2}^k = \sigma_k \left(\frac{(\bar{y}_{31})^2}{4A_e} \right) \left(\frac{(\bar{x}_{13})^2}{4A_e} \right) \quad (27)$$

$$\mathbf{A}_{M2,3}^k = \mathbf{A}_{M3,2}^k = \sigma_k \left(\frac{\bar{y}_{31}\bar{y}_{12}}{4A_e} \right) \left(\frac{\bar{x}_{13}\bar{x}_{21}}{4A_e} \right) \quad (28)$$

$$\mathbf{A}_{M3,3}^k = \sigma_k \left(\frac{(\bar{y}_{21})^2}{4A_e} \right) \left(\frac{(\bar{x}_{21})^2}{4A_e} \right) \quad (29)$$

APPENDIX A.

The matrix is indeed symmetric, i.e.,

$$\mathbf{A}_{Mi,j}^k = \mathbf{A}_{Mj,i}^k \quad (30)$$

Thus, some of the entries do not have to be explicitly evaluated.

The other integral composing the system matrix \mathbf{A} is the boundary integral,

$$\mathbf{A}_{Zi,j} = \int_{\Gamma_l} \frac{1}{z_l} N_i N_j dS_{\Gamma_l} \quad (31)$$

where $\frac{1}{z_l}$ such that $z_l \neq 0$ is the reciprocal of the contact impedance of the l^{th} electrode, and dS_{Γ_l} is the discriminant of integration either in the x or y direction in the Cartesian coordinates, or ξ or η in the natural coordinates. However, having assumed a 2D geometrical shape, the matrix $\mathbf{A}_{Zi,j}$ eventually results from solving a line integral, which is easy to evaluate either on the xy -coordinate or $\xi\eta$ -coordinate.

However, solving this integral can be done through mapping the edge from the xy -coordinate onto the natural coordinate system, as shown in Figure 3, where integrating along the edge $1 \rightarrow 2$ on the regular triangle is equivalent to integrating from $0 \rightarrow 1$ along the ξ -axis of the natural coordinate system multiplied by the length of the edge. In other words,

$$dl = l_{12} d\xi \quad (32)$$

where $l_{12} = \sqrt{\bar{x}_{21}^2 + \bar{y}_{21}^2}$

Next, the integral can be rewritten as,

$$\mathbf{A}_{Zi,j} = \frac{1}{z_l} \int_0^1 N_i(\xi, 0) N_j(\xi, 0) l_{12} d\xi \quad (33)$$

Therefore,

$$\mathbf{A}_{Z1,1} = \frac{1}{z_l} \int_0^1 N_1^2(\xi, 0) l_{12} d\xi = \frac{l_{12}}{z_l} \int_0^1 (1-\xi)^2 d\xi = \frac{l_{12}}{3z_l} \quad (34)$$

$$\mathbf{A}_{Z1,2} = \frac{1}{z_l} \int_0^1 N_1(\xi, 0) N_2(\xi, 0) l_{12} d\xi = \frac{l_{12}}{z_l} \int_0^1 (1-\xi)\xi d\xi = \frac{l_{12}}{6z_l} \quad (35)$$

APPENDIX A.

$$\mathbf{A}_{z_{1,3}} = \frac{1}{z_l} \int_0^1 N_1(\xi, 0) N_3(\xi, 0) l_{12} d\xi = 0 \quad (36)$$

$$\mathbf{A}_{z_{2,1}} = \mathbf{A}_{z_{1,2}} \quad (37)$$

$$\mathbf{A}_{z_{2,2}} = \frac{1}{z_l} \int_0^1 N_2^2(\xi, 0) l_{12} d\xi = \frac{l_{12}}{z_l} \int_0^1 \xi^2 d\xi = \frac{l_{12}}{3z_l} \quad (38)$$

$$\mathbf{A}_{z_{2,3}} = \frac{1}{z_l} \int_0^1 N_2(\xi, 0) N_3(\xi, 0) l_{12} d\xi = 0 \quad (39)$$

$$\mathbf{A}_{z_{3,1}} = \mathbf{A}_{z_{3,2}} = \mathbf{A}_{z_{3,3}} = 0 \quad (40)$$

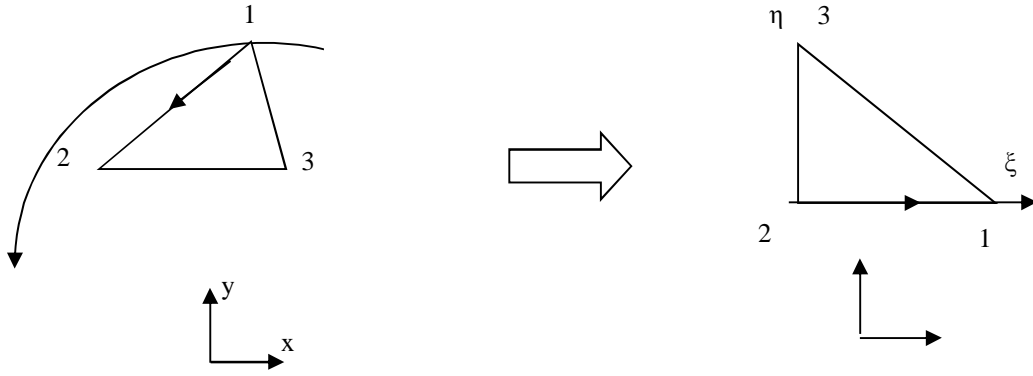


Figure A-3. (a) A triangular element with an edge on boundary. (b) Master triangular element.

Further, for the boundary integral $\mathbf{A}_{w_i, j} = -\int_{\Gamma_l} \frac{1}{z_l} N_i dS_{\Gamma_l}$, the same concept applies as it

is basically a 1-dimensional line integral and can be solved simply over the ξ -axis after rewriting the integral as,

$$\mathbf{A}_{w_i} = -\int_{\xi} \frac{1}{z_l} N_i(\xi, 0) d\xi \quad (41)$$

which can be evaluated directly as

$$\mathbf{A}_{w_1} = -\frac{1}{z_l} \int_0^1 (1-\xi) d\xi = -\frac{1}{2z_l} \quad (42)$$

$$\mathbf{A}_{w_2} = -\frac{1}{z_l} \int_0^1 \xi d\xi = -\frac{1}{2z_l} \quad (43)$$

$$\mathbf{A}_{w_3} = 0 \quad (44)$$

APPENDIX A.

Finally, this will conclude with the forth component,

$$\mathbf{A}_{D_{i,j}} = \begin{cases} \left(\frac{1}{z_l} \right)_j |\Gamma_l| & \text{for } i = j \\ 0 & \text{otherwise} \end{cases} \quad i, j = 1, \dots, L \quad (45)$$

which is essentially a diagonal matrix having the values $\left(\frac{|\Gamma_l|}{z_l} \right)_j$ across its diagonal, and $|\Gamma_l|$ is the length of the line segment underneath the electrode.

Appendix B

The derivation of the Jacobian matrix based on the Complete Electrode Model

In Chapter Two, it is described how the Jacobian matrix can be derived and formulated using the standard model [40] is used to. However, in this section, another method based on the complete electrode model CEM [47] is used to derive the Jacobian matrix for the 2D case i.e., $(\mathbf{x} \subset \Omega) \in \mathbb{R}^2$.

Basically, starting from the weak form of governing EIT problem $\nabla \cdot (\sigma(\mathbf{x}) \nabla \phi(\mathbf{x})) = 0$ (or Green identity), for any $w(\mathbf{x}) \in L_2$

$$\int_{\Omega} \nabla \cdot (w \sigma \nabla \phi) d\Omega = \int_{\partial\Omega} w \sigma \nabla \phi \hat{\mathbf{n}} dS \quad (1)$$

Here $d\Omega$ and dS are discriminants indicating surface and line measures, respectively. In particular, for $w = \phi$ we have the power conservation formula

$$\begin{aligned} \int_{\Omega} \sigma |\nabla \phi|^2 d\Omega &= \int_{\partial\Omega} \phi \sigma \nabla \phi \hat{\mathbf{n}} dS \\ &= \int_{\Gamma} \phi \sigma \nabla \phi \hat{\mathbf{n}} dS_{\Gamma} + \underbrace{\int_{\partial\Omega \setminus \Gamma} \phi \sigma \nabla \phi \hat{\mathbf{n}} dS_{\partial\Omega \setminus \Gamma}}_{=0} \\ &= \int_{\Gamma} \phi \sigma \nabla \phi \hat{\mathbf{n}} dS_{\Gamma} + \underbrace{\int_{\partial\Omega \setminus \Gamma} \phi \sigma \nabla \phi \hat{\mathbf{n}} dS_{\partial\Omega \setminus \Gamma}}_{=0} \quad (2) \\ &= \sum_{l=1}^L \int_{\Gamma_l} \left(V_l - z_l \sigma \frac{\partial \phi}{\partial \hat{\mathbf{n}}} \right) \sigma \nabla \phi \hat{\mathbf{n}} dS_{\Gamma_l} \end{aligned}$$

Therefore,

$$\int_{\Omega} \sigma |\nabla \phi|^2 d\Omega + \sum_{l=1}^L \int_{\Gamma_l} z_l (\sigma \nabla \phi \hat{\mathbf{n}})^2 dS_{\Gamma_l} = \sum_l V_l I_l \quad (3)$$

Equation (3) states that the input power is dissipated either in the domain Ω or by the contact impedance layer under the electrodes.

APPENDIX B.

Further, when for the inhomogeneous case when a perturbation takes place and $\sigma \rightarrow \sigma + \delta\sigma$, $\phi \rightarrow \phi + \delta\phi$ and $V_l \rightarrow V_l + \delta V_l$ with the current in each electrode I_l held constant. By ignoring the higher order terms in Equation (3) gives

$$\int_{\Omega} \delta\sigma \cdot |\nabla\Omega|^2 d\Omega + 2 \int_{\Omega} \sigma \nabla\phi \cdot \nabla\delta\phi d\Omega + 2 \sum_{l=1}^L \int_{\Gamma_l} z_l (\sigma \nabla\phi \cdot \hat{\mathbf{n}}) \delta(\sigma \nabla\phi \cdot \hat{\mathbf{n}}) dS_{\Gamma_l} = \sum_l V_l I_l \quad (4)$$

On the l th electrode,

$$\delta(\sigma \nabla\phi \cdot \hat{\mathbf{n}}) = \frac{1}{z_l} (\delta V_l - \delta\phi) \quad (5)$$

Using this and the weak formulation with $w = \delta\phi$ we get

$$\int_{\Omega} \delta\sigma |\nabla\phi|^2 d\Omega + 2 \int_{\partial\Omega} \delta\phi \sigma \nabla\phi \cdot \hat{\mathbf{n}} - 2 \sum_{l=1}^L z_l \int_{\Gamma_l} \frac{\delta\phi}{z_l} \sigma \nabla\phi \cdot \hat{\mathbf{n}} dS_{\Gamma_l} + 2 \sum_{l=1}^L \delta V_l \int_{\Gamma_l} \sigma \nabla\phi \cdot \hat{\mathbf{n}} dS_{\Gamma_l} = \sum_l I_l \delta V_l \quad (6)$$

In Equation (6), the second and third terms on the left-hand side cancel, and the fourth term is $2 \sum_l I_l \delta V_l$ which results in,

$$\sum_l I_l \delta V_l = \int_{\Omega} \delta\sigma |\nabla\phi|^2 d\Omega \quad (7)$$

which is essentially the total change in power. In order to derive the total change on a particular measuring electrode m when a current pattern $\mathbf{I}^{[d]}$ is driven at some or all of the other electrodes, the resulted ‘measurement pattern potential’ $\phi(\mathbf{I}^{[m]})$ should be calculated. $\phi(\mathbf{I})$ indicates the electric potential on a vector of electrode currents $\mathbf{I} = [I_1, \dots, I_L]$ and the potential for the d th drive pattern is $\phi(\mathbf{I}^{[d]})$. By applying the power perturbation formula of Equation (7) to $\phi(\mathbf{I}^{[d]}) + \phi(\mathbf{I}^{[m]})$ and $\phi(\mathbf{I}^{[d]}) - \phi(\mathbf{I}^{[m]})$ then subtracting gives

$$\delta\mathbf{y}^{(d,m)} = - \int_{\Omega} \delta\sigma \nabla\phi(\mathbf{I}^{[d]}) \cdot \nabla\phi(\mathbf{I}^{[m]}) d\Omega \quad (8)$$

APPENDIX B.

where $\delta \mathbf{y}^{(d,m)}$ is the m th measurement under the d th current pattern.

To calculate the Jacobian one must choose the discretisation of the conductivity. The simplest case is to take the conductivity to be piecewise constant on polyhedral domains, such as voxels or tetrahedral elements. Taking $\delta \sigma$ to be the characteristic function of the k th element, then for a fixed pattern

$$\mathbf{J}_{((d;m),k)} = \frac{\partial \mathbf{y}^{(d,m)}}{\partial \sigma_k} = - \int_{\Omega_k} \nabla \phi(\mathbf{I}^{[d]}) \cdot \nabla \phi(\mathbf{I}^{[m]}) d\Omega_k \quad (9)$$

Finally, the resulted Jacobian matrix will have the following format

$$\mathbf{J} = \begin{bmatrix} \frac{\partial \mathbf{y}(\mathbf{I}^{(1)})}{\partial \sigma_1} & \dots & \dots & \frac{\partial \mathbf{y}(\mathbf{I}^{(1)})}{\partial \sigma_K} \\ \vdots & \ddots & \ddots & \vdots \\ \frac{\partial \mathbf{y}(\mathbf{I}^{(3)})}{\partial \sigma_1} & \ddots & \frac{\partial \mathbf{y}(\mathbf{I}^{(3)})}{\partial \sigma_n} & \vdots \\ \vdots & \ddots & \ddots & \vdots \\ \frac{\partial \mathbf{y}(\mathbf{I}^{(d)})}{\partial \sigma_1} & \dots & \dots & \frac{\partial \mathbf{y}(\mathbf{I}^{(d)})}{\partial \sigma_K} \end{bmatrix} \quad (2.10)$$

where K is the total number of finite elements composing the medium,.

Some EIT and capacitance tomography systems use a constant voltage source and in this case the change in power of an increase in admittivity will have the opposite sign to the constant case. Under realistic conditions, it is recommended to formulate a fine mesh for the forward problem and a coarser mesh for the inverse, since a perfect model is not feasible.

Appendix C

Image reconstructions for 2D and 3D shapes for various electrode numbers and current injection protocols

In this section, various 2D and 3D images reconstructions are presented for both the conventional opposite 2–electrode pair and the proposed multi–injection protocols. That is to give representative and visual comparisons between these protocols when it comes to the quality of the reconstructed images. The prime reason of the absence of quality measures is that for different electrode numbers, and different combinations of current–injecting electrodes, the generated meshes using Netgen will have different topologies in terms of number of elements, and their respective sizes and centroids.

Figures (1), (3), and (5) show various image reconstructions for a 2D, 3D with 3–rings of electrodes, and 3D with 4 rings of electrodes, respectively. For the 3D cases, reconstructed images are resulted through slicing the model at different fixed heights described by vector $\mathbf{h}=\{0.1, 0.2, 0.3, 0.4, 0.5, 0.6\}$.

APPENDIX C.

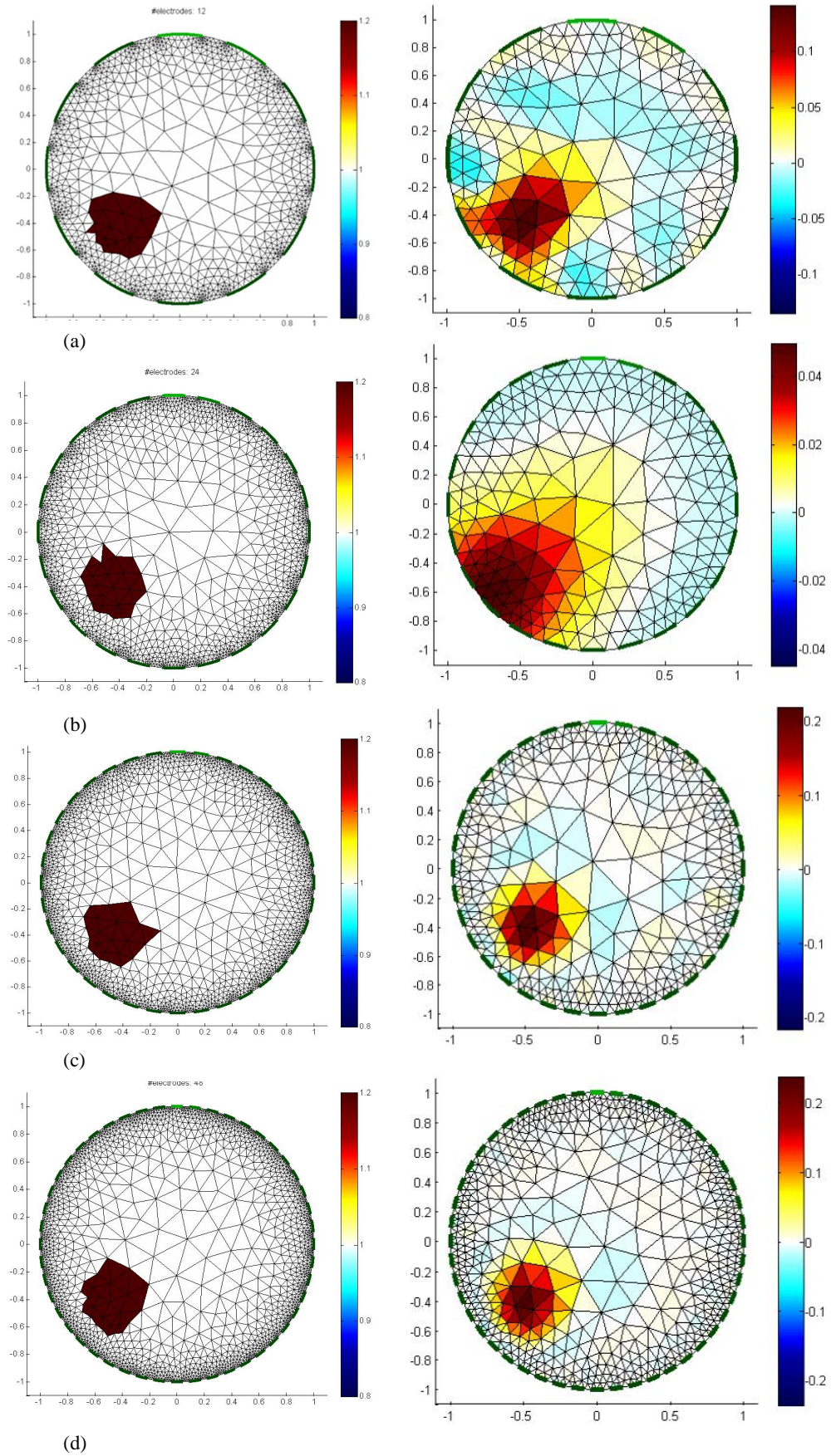


Figure C-1 2D reconstructions when using conventional opposite 2-electrode pair protocol

APPENDIX C.

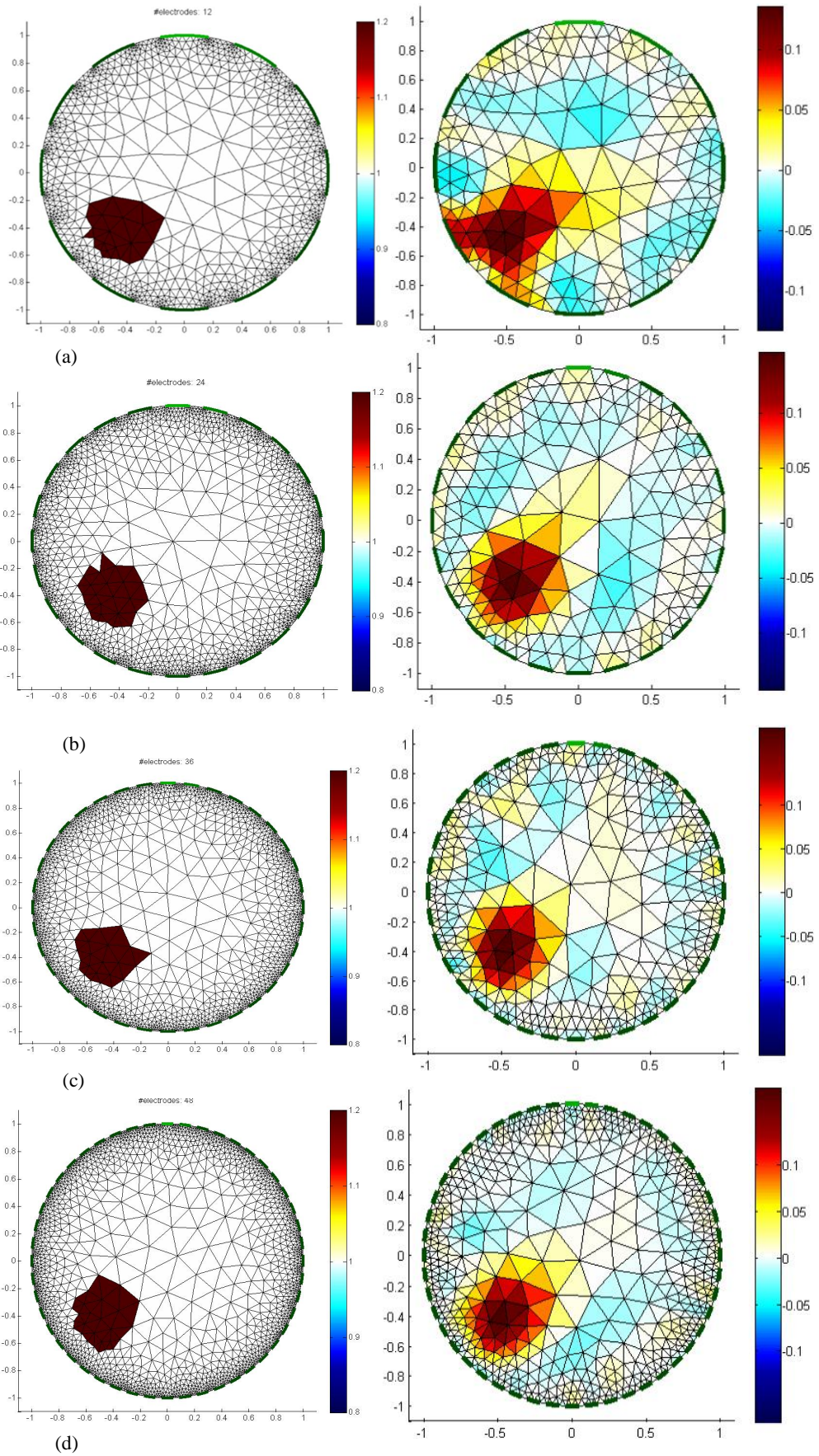


Figure C-2 2D reconstructions when deploying the proposed multi-injection protocol

APPENDIX C.

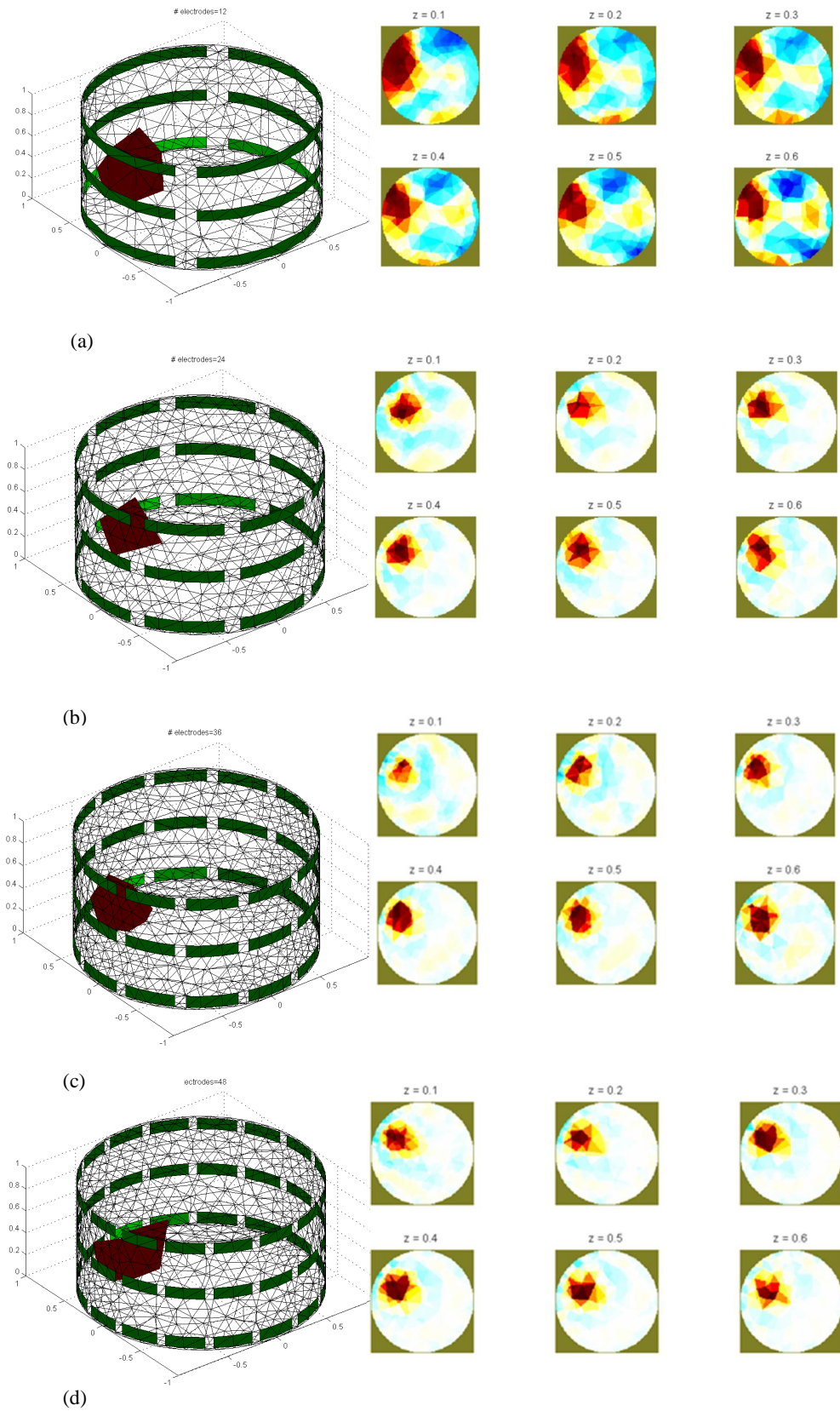


Figure C-3 3D reconstructions at different heights when using the conventional 2-electrode pair protocol, a maximum of 3 electrode rings is allowed.

APPENDIX C.

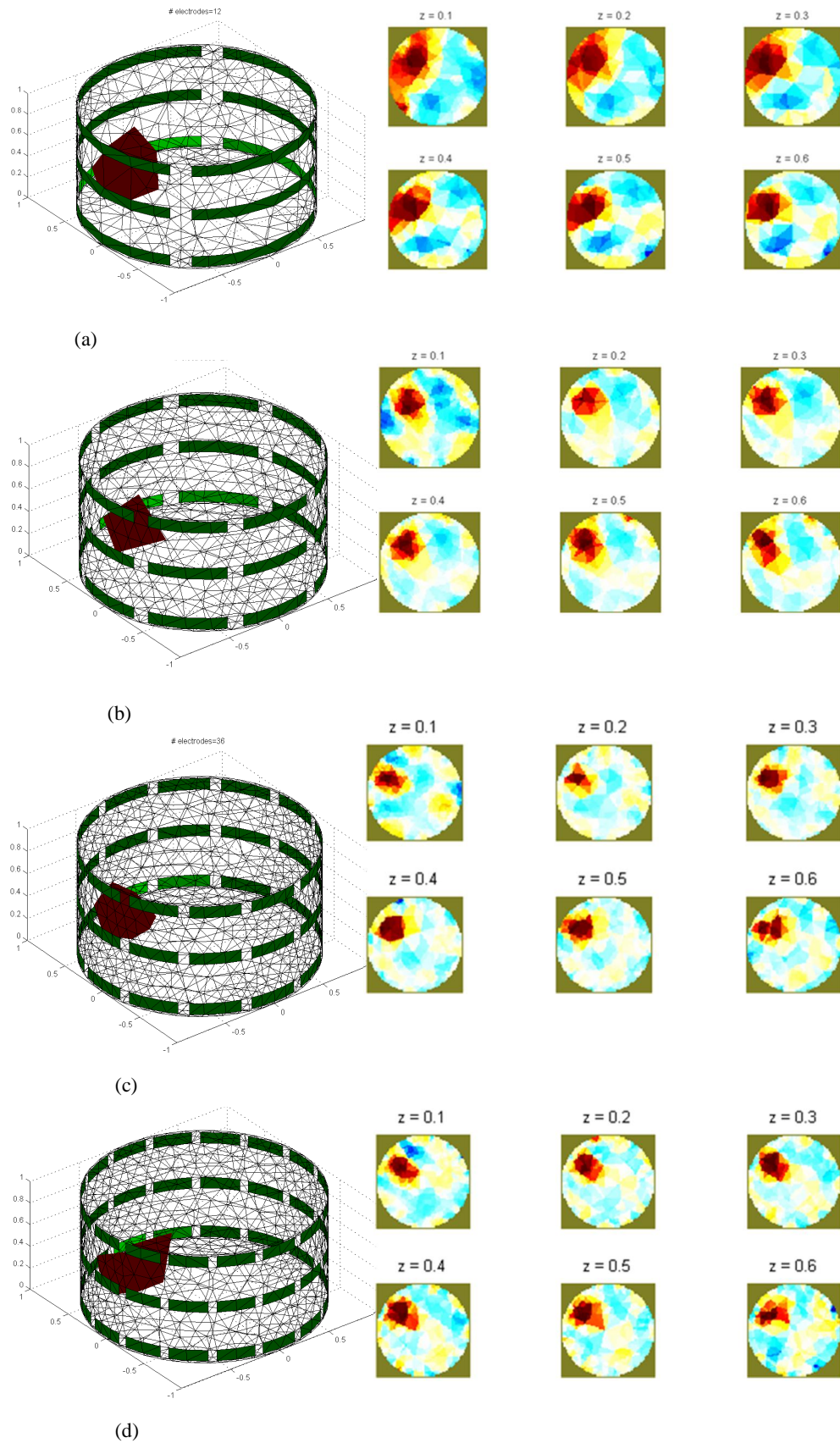


Figure C-4 3D reconstruction at different heights when deploying the proposed multi-injection protocol, a maximum of 3 electrode rings is allowed.

APPENDIX C.

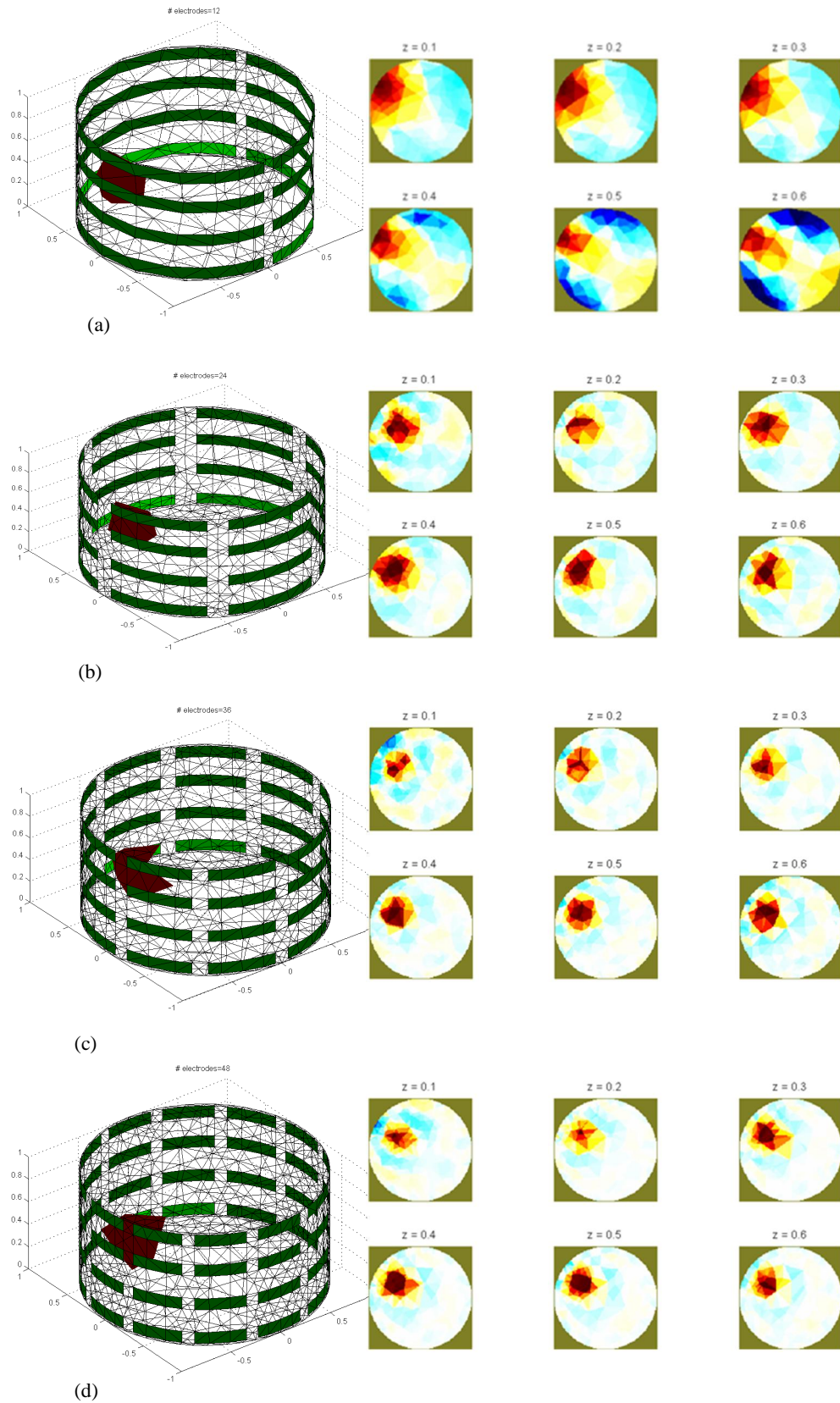


Figure C-5 3D construction at different heights when using conventional 2-electrode pair protocol, a maximum of 4 electrode rings is allowed.

APPENDIX C.

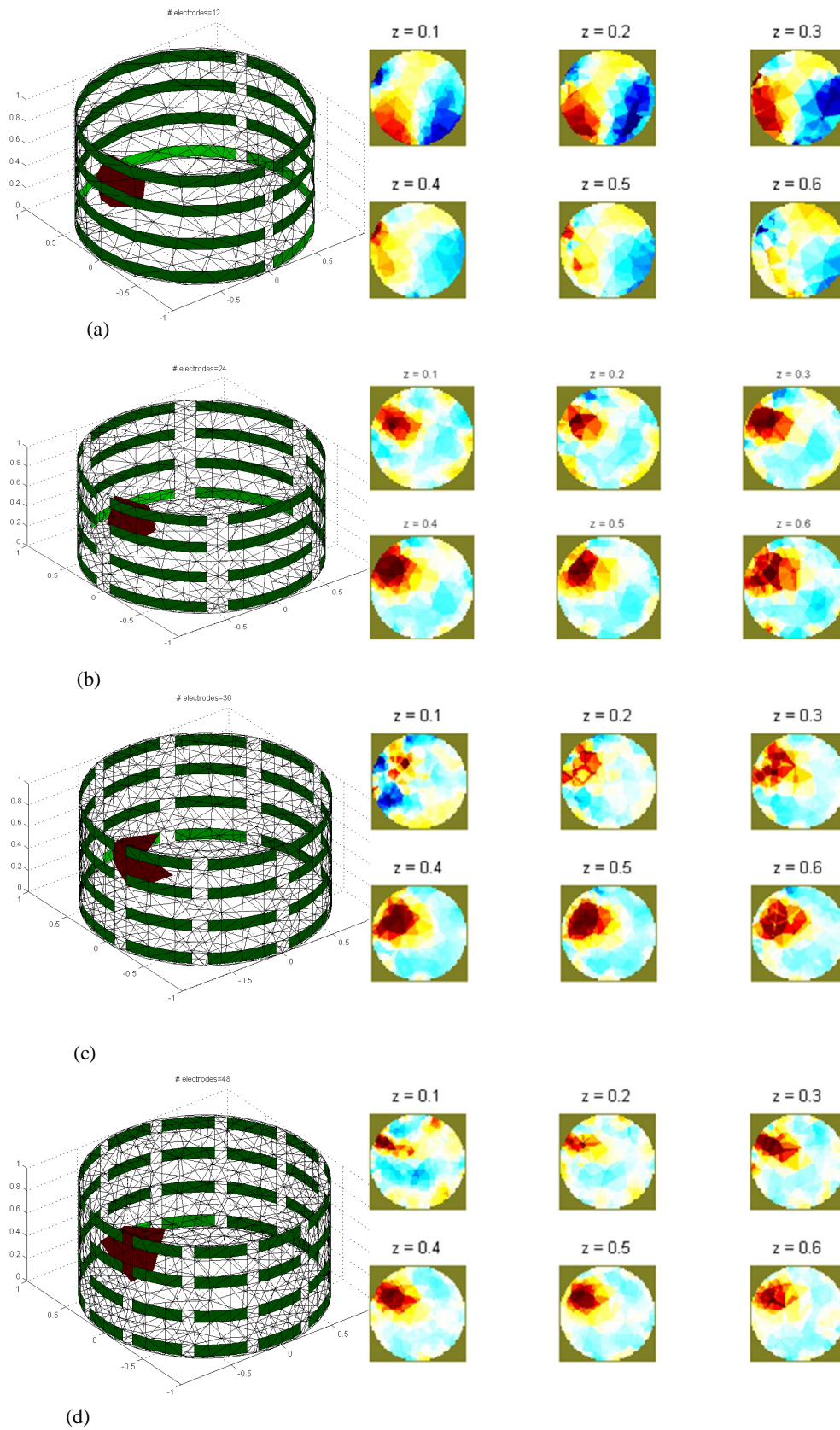


Figure C-6 3D reconstructions at different heights when deploying multi-injection protocol, a maximum of 4 electrode rings is allowed.